
Calculation of Quantum Error Correction Thresholds and Numerical Analysis of the Spinful Bose-Fermi-Hubbard Model

Janik Oliver Schönmeier-Kromer



München 2022

Calculation of Quantum Error Correction Thresholds and Numerical Analysis of the Spinfull Bose-Fermi-Hubbard Model

Janik Oliver Schönmeier-Kromer

Dissertation
der Fakultät für Physik
der Ludwig-Maximilians-Universität
München

vorgelegt von
Janik Oliver Schönmeier-Kromer
aus Saarbrücken

München, den 21.12.2021

Erstgutachter: Prof. Dr. Lode Pollet

Zweitgutachter: Prof. Dr. Miguel A. Martin-Delgado

Tag der mündlichen Prüfung: 03.02.2022

Zusammenfassung

Die Suche nach Quantencomputern wird durch das Versprechen motiviert, bestimmte komplexe Problemstellungen, die von klassischen Computern nicht in angemessener Zeit berechenbar sind, zukünftig lösen zu können. Für die Realisierung gibt es neben der bloßen Wahl des physikalischen Systems, das als Hardware Plattform genutzt wird, auch Unterschiede in der Herangehensweise. In dieser Arbeit nutzen wir moderne Monte-Carlo-Simulationen, um Vielteilchensysteme numerisch zu analysieren, die für zwei der vielversprechendsten Ansätze relevant sind.

In universellen Quantencomputern wird ein physikalisches System als Speicher für einen quantenmechanischen Zustand genutzt. Rechnungen werden durch die Anwendung vordefinierter Logikgatter ausgeübt, die durch gezielte Beeinflussungen des physikalischen Systems realisiert werden. Hierbei können jedoch bewusste Interaktionen oder Umweltfaktoren zu Fehlern im dargestellten Zustand führen. Im ersten Teil der Arbeit analysieren wir die Grenzen der Anwendbarkeit von Fracton Codes für die Fehlerkorrektur solcher Systeme. Als Musterbeispiel untersuchen wir das "X-cube" Modell, indem die Fehlerkorrekturprozesse auf zwei neue Modelle mit klassischen Spins abgebildet werden. Durch die Bestimmung der Phasendiagramme können wir für den Fracton Code die zulässigen Grenzwerte der Fehlerrate ermitteln. Eine potentielle Hardware Plattform muss diese unterschreiten. Bei der ermittelten, zulässigen Rate von 7.5% ist eine deutlich höhere Fehlerresistenz im Vergleich zu bisherigen topologischen Codes (3.3%) zu erwarten.

Im zweiten Teil befassen wir uns mit einem Modell für ein Gemisch ultrakalter Quantengase. Solche Gase sind ein vielversprechender Kandidat für einen Quantensimulator. In diesem sollen zu untersuchende Vielteilchensysteme direkt durch ein anderes, vollständig kontrollierbares und messbares Quantensystem imitiert werden, um beispielsweise das dynamische Verhalten der Zielsysteme zu analysieren. Mithilfe eines mehrkomponentigen Wurm Algorithmus studieren wir das Grundzustandsphasendiagramm des eindimensionalen, spin-behafteten Bose-Fermi-Hubbard Modells bei konstanter Dichte. Insbesondere untersuchen wir die wechselseitig induzierten Interaktionen unter den Bosonen und Fermionen durch die jeweils andere Teilchenart. Für große Teile des Phasendiagramms finden wir die vorherrschenden Phasen im thermodynamischen Grenzfall, beobachten jedoch auch Bereiche, in denen Instabilitäten selbst in großen Gittern konkurrierend bleiben.

Abstract

The ongoing quest for the realization of quantum computers is inspired by the inherent promise of solutions to classically intractable problems in the future. Beyond the mere choice for one of the various hardware platform candidates, there are also different competitive methodical approaches. In this work we use state-of-the-art Monte Carlo simulations to analyse many-body systems which are relevant for two of the most promising research directions in the field of quantum computing.

Gate-based quantum computing is centered around a quantum memory, retaining a quantum mechanical state. Processing is carried out through the application of predefined logical quantum gates on the quantum memory and is realized by careful manipulation of the underlying quantum hardware system. However, noise in the quantum system or the interaction during gate execution makes the quantum memory prone to errors. The first part of this thesis addresses the capabilities of fracton codes for quantum error correction. We study the exemplary X-cube model by mapping the error correction processes for bit-flip and phase-flip errors to two novel Ising spin models with random multi-body couplings. From the careful numerical examination of the respective phase diagrams, the optimal error thresholds are determined. The minimal threshold is the relevant one for error correction and is remarkably high at 7.5%, compared to the previously studied Kitaev model with 3.3% or color codes with 1.9%. This encouraging result paves the way for new designs in quantum memories.

In the second part of the thesis we investigate the spinful Bose-Fermi-Hubbard model, which describes a mixture of ultracold quantum gases trapped in an optical lattice. Such ultracold gases are a promising candidate for the successful realization of quantum simulators. This approach aims at direct emulation of a target system through a second fully controllable and accessible quantum system, to study properties like the dynamical evolution of the target system. Using a multi component worm algorithm, we analyse the ground state phase diagram of the model for half filling in both fermionic components and unit filling in the bosons in a one dimensional lattice. We address the question of the mutually induced intracomponent interactions and establish the thermodynamically stable phases across large regimes of the phase diagram. For some regimes we find competing interactions persisting on length scales beyond mesoscopic systems.

Contents

Zusammenfassung	v
Abstract	vii
1 Introduction	1
I Quantum Computing Error Thresholds	5
2 Quantum computing	7
2.1 From bit to qubit	8
2.2 Universal gateset	10
2.3 Quantum algorithms	14
3 Quantum error correction	19
3.1 Quantum error channels	20
3.2 Classical error correction	20
3.3 Shor’s repetition algorithm	22
3.4 Stabilizer codes	25
3.5 Mapping to classical spin systems	29
3.6 X-Cube model	35
4 Classical Monte Carlo	41
4.1 Classical statistical physics	41
4.1.1 Standard observables and the partition sum	42
4.2 Markov chain Monte Carlo	46
4.3 Local updates	48
4.3.1 Metropolis algorithm	48
4.3.2 Heat-bath algorithm	49
4.4 Parallel tempering	50

Contents

5	Numerical analysis of the optimal error thresholds	53
5.1	Models and symmetries	53
5.1.1	Disorder free models	55
5.1.2	Order parameters	55
5.1.3	Non-standard first-order scaling	57
5.1.4	Numerical results in the disorder free case	58
5.2	First-order phase transition regime	61
5.3	Second-order phase transition regime and optimal error-threshold values	66
II	Spinfoil Bose-Fermi-Hubbard Model	71
6	Bosons and Fermions in lattices	73
6.1	Bosonic Hubbard models	74
6.1.1	Bose-Hubbard model	76
6.1.2	Extended Bose-Hubbard model	79
6.2	Fermionic Hubbard models	83
6.2.1	Extended Fermi-Hubbard model	84
6.3	Bose-Fermi-Hubbard models	86
6.3.1	Spin polarized Bose-Fermi-Hubbard model	86
6.3.2	Spinfoil Bose-Fermi-Hubbard model	89
7	Path integral Monte Carlo method	91
7.1	Exact diagonalization as benchmark method	91
7.2	Path integral formulation	93
7.3	Bosonic worm algorithm	97
7.3.1	Insertworm and Glueworm	100
7.3.2	Moveworm	103
7.3.3	Insertkink and Deletkink	106
7.4	Observables	107
7.5	Two worm algorithm	109
7.5.1	Four operator Insertworm and Glueworm update	111
7.5.2	New Moveworm	112
8	Phase diagram of the spinfoil Bose-Fermi-Hubbard model	115
8.1	Analytical considerations	115
8.1.1	Weak interspecies coupling regime	116

8.1.2	Strong interspecies coupling regime	119
8.2	Phase diagram	119
8.3	Numerical results	121
8.3.1	Bosonic Mott insulator to superfluid transition	121
8.3.2	Exemplary scan at intermediate interspecies coupling	125
8.3.3	Exemplary scan at strong interspecies coupling	128
9	Conclusions and perspectives	133
Appendix A	Simulational parameters for the RPI and RACAT model	135
Appendix B	Kramers-Wannier duality for CSS code	139
Appendix C	Benchmarking the worm algorithm	143
	Bibliography	147
	List of Publications	161

Chapter 1

Introduction

Quantum computers hold the promise of new solutions to certain problem classes which have proven resilient to conventional classical computational methods. Examples for these problems are ubiquitous not only in physics, where for example certain many-body problems like high temperature superconductors are intractable [1–3], but also in industrial applications like optimization problems in production, logistics or engineering [4], cryptography [5, 6] or machine learning methods [7]. Based on Feynmans conceptual proposal to simulate physics on computers, which obey quantum mechanical laws [8], several interesting methodological approaches have been developed. In adiabatic quantum computing the known ground state of an accessible initial Hamiltonian is prepared in a quantum annealer, and adiabatically time evolved to end up with the ground state of a target Hamiltonian [9–12]. Universal gate based quantum computing is based on the realization of a quantum memory consisting of individual qubits, which can be acted on by logical quantum gates reminiscent of bits and classical logic gates in conventional computers [13–16]. In quantum simulators a physical target system is directly emulated by another physical system displaying better tunability, control and measurement results but obeying the same Hamiltonian, thus enabling the study of physical properties of the target system under consideration[17–20].

The first part of this thesis addresses the ongoing quest for a reliable quantum memory for the second approach of the above non exhaustive list of research directions. The memory based on a physical system has to obey the rules of quantum mechanics in the anticipated way, needs to be capable to be controllable to enable the application of logical gates on the intrinsic qubits and store the information encoded in the quantum state resilient from noise in the system. In the beginnings of gate based quantum computing sets of a single or a few individual qubits were experimentally realized and acted on by simple single or two qubit gates, which will be discussed in Chapter 2. Even though the storage and manipulation of qubits

Chapter 1 Introduction

was demonstrated in multiple physical platforms, they still suffer display short coherence times and imperfect gates [21–23]. We are now in the era of Noisy Intermediate-Scale Quantum (NISQ) devices, where reasonable amounts of qubits are realizable but are still prone to noise [24]. For example in superconducting qubits the technological advances throughout the recent years were dominated by an impressive increase in the number of controllable qubits, but the coherence times, which are the limiting factor to the depth of a quantum circuit, have improved at a smaller rate. Thus encoding a set of physical qubits redundantly into one logical qubit is among the most prominent candidates to succeed in quantum error correction. Chapter 3 first elaborates the general ideas of this approach for quantum systems which recently have been dominated by topological codes [25–27]. It is possible to establish a connection between these error correction codes and classical statistical spin models to study the expected error thresholds in a systematical way. We study for the first time systematically the optimal error thresholds of an error correction scheme based on a fracton model, which is also based on stabilizers, but differs from the notion of conventional topology, namely the X-cube code. The displayed interesting geometrical properties of the model make it potentially suitable for error correction. The study is based on the mapping of the error correction processes for bit-flip and phase-flip errors to the random plaquette Ising (RPI) model and the random anisotropically coupled Ashkin-Teller (RACAT) model respectively. The temperature-disorder phase diagrams of these two new models, which both display interesting subsystem symmetries, are analysed with large-scale parallel tempering Monte Carlo simulations. The numerical method is explained in Chapter 4. Chapter 5 presents our results for the respective phase diagrams and reports the minimum error threshold for the fracton code.

In the second part of this thesis we study a theoretical model for a mixture of bosonic and fermionic ultracold quantum gases. Such gases trapped in optical lattices in vacuum chambers represent a clean, fully controllable and versatile physical system, which makes them a promising candidate for the successful realization of a quantum simulator for classically incomputable many-body problems in condensed matter theory [28, 29]. Recently a quantum simulator for the dynamics of the Fermi-Hubbard model (FHM) in one dimension (1D) with spinful fermions was successfully realized [20]. In nature as well as in technologically highly relevant materials, like high T_c superconductors [1, 30], multicomponent systems are omnipresent. A neutral atom based quantum simulator, aiming at a realistic representation of these systems thus will need to be able to contain a mixture of

bosons and fermions in a single controllable optical lattice. Bose-Fermi mixtures in their own right have attracted interest ever since the first experiments with mixtures of ^3He and ^4He , and we discuss the properties of such systems in more detail in Chapter 6. There we also discuss purely bosonic and purely fermionic systems in lattices and introduce the Hamiltonian for the spinful Bose-Fermi-Hubbard model. We analyse the ground state phase diagram of the model in 1D for unity filling in the bosons and half filling in each fermionic component with a multi component worm algorithm, which is discussed in Chapter 7. Since numerically only finite system sizes are accessible, we have to carefully investigate the flow of the competing instabilities and the respective order parameters for the possible quantum phases in the system. Taking analytical considerations and finite size scalings into account we deduce the thermodynamically stable phases for large parts of the phase diagram but also find regimes where no final result can be extrapolated from the length scales, which are accessible numerically within reasonable time. The phase diagram together with the weak and strong coupling expansions and exemplary numerical evidence is presented in Chapter 8.

Part I

**Quantum Computing Error
Thresholds**

Chapter 2

Quantum computing

In 1965 George Moore described his empirical observation that the number of transistors in an integrated circuit is approximately doubled every year. In the initial publication he wrote:

”The complexity for minimum component costs has increased at a rate of roughly a factor of two per year . . . That means by 1975, the number of components per integrated circuit for minimum cost will be 65,000. I believe that such a large circuit can be built on a single wafer.” [31] (p.105)

To put his vision into perspective it should be noted that at the time he uttered his believes there were between 64 and 128 components in a single integrated circuit. Even though he adjusted the time interval to two years in 1975, his rule of thumb became famous by the name Moore’s law as the development of ever smaller components arose. In modern chips a single building block is only of the size of 10 nm. However, this process of miniaturization of the elemental building blocks has a physical limitation and even Moore himself admitted in an interview in 2007 that the size of single atoms will serve as a natural boundary, which can not be surpassed. So even without any consideration of heating issues, which already today limit further miniaturization, chip companies will not be able to build transistors, which undercut the atomic diameter of atoms like silicon, which is 0.1nm. Since a further improvement merely by an increase in clock speeds or number of transistors does not seem to be feasible beyond these natural limits, a change of the underlying concepts in computing might be necessary.

Already in 1982 Feynman proposed the idea that computational simulations of physical problems should be done directly according to quantum mechanical laws and not according to classical computations, which are then analysed to explain quantum mechanical systems [8]. Since then the quest to develop a universal computation machine, which acts according to quantum mechanical rules, has gained

traction. Even though this new paradigm was initially aiming at simulating nature through nature, it soon became evident that there even might be applications beyond physical problems. Inspired by quantum algorithms like Shor’s algorithm [5], which is able to factorize large integers almost exponentially faster than any known classical algorithm, interest arose beyond academia in industry. Today we are at a stage where noisy quantum computers are reality and the number of qubits, which in analogy to classical bits are the fundamental building blocks of quantum computers, can reach 64. While we are currently in the age of NISQ [24] computers it is important to envision how the path ahead might look for quantum computing. Apart from the bare number of qubits realizable in a system, a fundamental limitation in any computation is the effect errors inflict on the stored information. We therefore propose a new error correction scheme, which would allow for fault-tolerant quantum computing [32] in Section 3. But first let us introduce the basic notion of a qubit and revisit the necessary core concepts of quantum mechanics in this section.

2.1 From bit to qubit

In classical computing the smallest piece of information is a bit. It is a binary digit, which can take one of the discrete values 0 or 1. Operations are done by elementary gates like the *AND* and *OR* gate, which take two bits b_1, b_2 as their input and return one output bit b_{out} or gates, which act on a single bit as the *NOT* gate. The effects of these gates can be displayed by truth tables that list all possible permutations of input bits and the resulting output bit as demonstrated in Table 2.1.

<i>AND</i>		
b_1	b_2	b_{out}
0	0	0
0	1	0
1	0	0
1	1	1

<i>OR</i>		
b_1	b_2	b_{out}
0	0	0
0	1	1
1	0	1
1	1	1

<i>NOT</i>	
b_1	b_{out}
0	1
1	0

Table 2.1: Truth tables for the elementary Gateset *AND*, *OR* and *NOT* of a universal computer.

All boolean functions $f(b_1, b_2, \dots, b_n)$ with n input bits and one output bit can be executed by concatenations of these three basic gates and a machine hence is able to

2.1 From bit to qubit

perform universal operations on the contained bits [33]. Inspired by this terminology Deutsch suggested the qubit in his proposal of a universal quantum computer [13]. The qubit is the smallest building block of information in a quantum computer and can be realized by a quantum mechanical two-level system. Naturally this carrier of information is not limited to its two pure eigenstates $|0\rangle$ or $|1\rangle$, but can realize any superposition thereof, which is a linear combination $|\psi\rangle = \alpha|0\rangle + \beta|1\rangle$ with $\alpha, \beta \in \mathbb{C}$. With this change of paradigm not only the space of allowed states is enlarged [8], but also fundamentally different algorithms due to the new gateset are possible. A two-level system has two internal accessible eigenstates $|0\rangle$ and $|1\rangle$ with respect to the Pauli Z operator, which can serve as the basis for the space of possible states $|\psi\rangle$. In the *bra-ket* notation a *ket* $|\psi\rangle$ is a vector in the vector space \mathbb{C}^n , in the case of a two level system a vector in \mathbb{C}^2 respectively. A *bra* $\langle\psi|$ in a two level system is a linear form $f : \mathbb{C}^2 \rightarrow \mathbb{C}$, which maps a *ket* vector to a number in the complex plane. The convention in analogy of a spin 1/2 system reads:

$$|0\rangle = |\uparrow\rangle = \begin{pmatrix} 1 \\ 0 \end{pmatrix}, \quad |1\rangle = |\downarrow\rangle = \begin{pmatrix} 0 \\ 1 \end{pmatrix} \quad (2.1)$$

$$\langle 0| = \langle\uparrow| = \begin{pmatrix} 1 & 0 \end{pmatrix}, \quad \langle 1| = \langle\downarrow| = \begin{pmatrix} 0 & 1 \end{pmatrix} \quad (2.2)$$

Inner products are then denoted by $\langle\phi|\psi\rangle$ and orthogonality of two states is fulfilled if $\langle\phi|\psi\rangle = 0$. Pure states $|\psi\rangle$ are assumed to be normalized by $\langle\psi|\psi\rangle = 1$, which imposes the condition $\|\alpha\|^2 + \|\beta\|^2 = 1$ on the complex prefactors of any superposition state. An alternative parametrization of a single qubit state is given by the representation on the Bloch sphere

$$|\psi\rangle = \alpha|0\rangle + \beta|1\rangle = \cos(\theta/2)|0\rangle + e^{i\varphi}\sin(\theta/2)|1\rangle \quad (2.3)$$

where $\theta \in [0, \pi]$ and $\varphi \in [0, 2\pi[$ are the mixing and relative phase angle respectively. In this way any pure state can be represented as a point

$$|\psi\rangle \rightarrow \vec{r} = \begin{pmatrix} \cos\varphi \sin\theta \\ \sin\varphi \sin\theta \\ \cos\theta \end{pmatrix} \quad (2.4)$$

on a unit sphere in \mathbb{R}^3 as demonstrated in Figure 2.1. Note that any global phasefactor $\omega \in \mathbb{R}$ is not of physical importance and all states $|\psi'\rangle = e^{i\omega}|\psi\rangle$ result in the same point on the Bloch sphere. Quantum projector operators, which are frequently used in the definition of projective measurements, are defined as outer products $|\psi\rangle\langle\phi|$ in this formalism.

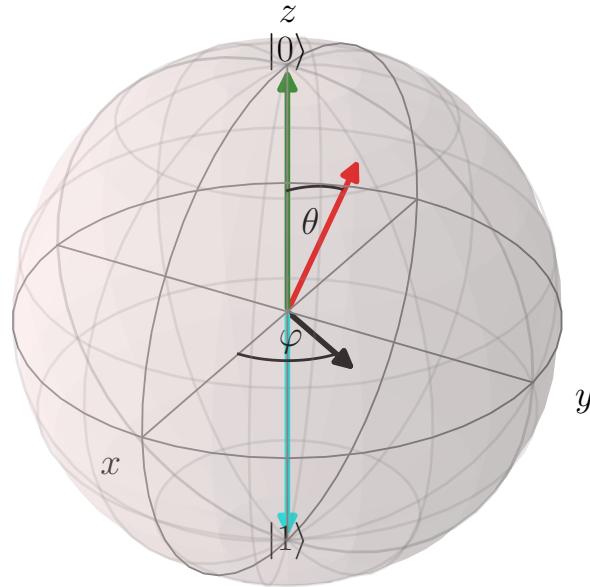


Figure 2.1: Representation of pure states on the Bloch sphere according to Equation 2.4.

The state $|0\rangle$ is represented by the green vector on top of the unit sphere. The respective orthogonal state $|1\rangle$ is visualized by the cyan vector. A linear superposition $|\psi\rangle$ of these two basis states is represented by the red arrow with $\theta = 30^\circ$ and $\varphi = 60^\circ$. φ is the angle between the black projection of $|\psi\rangle$ in the x-y-plane and the x-axis and θ is giving the inclination.

2.2 Universal gateset

Operations on qubits are represented by quantum gates, which are linear operators [34]. For a single qubit any possible gate \hat{G} can be represented as

$$\hat{G} = \sum_{i,j \in \{0,1\}} g_{ij} |i\rangle\langle j| = g_{00} |0\rangle\langle 0| + g_{01} |0\rangle\langle 1| + g_{10} |1\rangle\langle 0| + g_{11} |1\rangle\langle 1| = \begin{pmatrix} g_{00} & g_{01} \\ g_{10} & g_{11} \end{pmatrix} \quad (2.5)$$

where the g_{ij} are the complex amplitudes. Every gate needs to be unitary, so $\hat{G}^{-1} = \hat{G}^\dagger$ needs to be fulfilled and it is possible to write down the single qubit gates as the Pauli matrices

$$\hat{X} = \hat{\sigma}^X = \begin{pmatrix} 0 & 1 \\ 1 & 0 \end{pmatrix}, \hat{Y} = \hat{\sigma}^Y = \begin{pmatrix} 0 & -i \\ i & 0 \end{pmatrix}, \hat{Z} = \hat{\sigma}^Z = \begin{pmatrix} 1 & 0 \\ 0 & -1 \end{pmatrix}. \quad (2.6)$$

The \hat{X} operator is known as the qubit-flip gate, since it exchanges the amplitudes of $|0\rangle$ and $|1\rangle$. In Figure 2.1 the cyan vector would be transformed into the green vector

after the \hat{X} is applied and vice versa. The effect of \hat{X} when considering the Bloch sphere is generally given by a rotation around the x-axis. The \hat{Z} operator is referred to as phase-flip gate, since it reverses the relative phase of a single cubit state. Applied to a state on the Bloch sphere it can be considered as a rotation around the z-axis. The \hat{Y} results in a respective rotation around the y-axis.

To introduce the notion of eigenstates let us consider the effect of a \hat{Z} operator on the state $|0\rangle$.

$$\hat{Z}|0\rangle = \begin{pmatrix} 1 & 0 \\ 0 & -1 \end{pmatrix} \begin{pmatrix} 1 \\ 0 \end{pmatrix} = \begin{pmatrix} 1 \\ 0 \end{pmatrix} = |0\rangle \quad (2.7)$$

The state is unaffected by the operator. We call such states eigenstates with eigenvalue λ , which is the prefactor (in this case $\lambda = 1$). When applying \hat{Z} to $|1\rangle$, the result is $-|1\rangle$. Therefore $|1\rangle$ is also an eigenstate to \hat{Z} with eigenvalue $\lambda = -1$. It is similarly possible to find the eigenstates for the \hat{X} and \hat{Y} operator as

$$|+^X\rangle = |+\rangle = \frac{1}{\sqrt{2}} \begin{pmatrix} 1 \\ 1 \end{pmatrix} = \frac{|0\rangle + |1\rangle}{\sqrt{2}}, \quad |^{-X}\rangle = |-\rangle = \frac{1}{\sqrt{2}} \begin{pmatrix} 1 \\ -1 \end{pmatrix} = \frac{|0\rangle - |1\rangle}{\sqrt{2}} \quad (2.8)$$

$$|+^Y\rangle = |\phi^+\rangle = \frac{1}{\sqrt{2}} \begin{pmatrix} 1 \\ i \end{pmatrix} = \frac{|0\rangle + i|1\rangle}{\sqrt{2}}, \quad |^{-Y}\rangle = |\phi^-\rangle = \frac{1}{\sqrt{2}} \begin{pmatrix} 1 \\ -i \end{pmatrix} = \frac{|0\rangle - i|1\rangle}{\sqrt{2}}. \quad (2.9)$$

where $|+^O\rangle$ denotes the eigenstate to the operator \hat{O} with eigenvalue $\lambda = +1$ and $|^{-O}\rangle$ the respective eigenstate with $\lambda = -1$.

To realize the power of quantum computing, it is necessary to deal with multiple qubits and understand the notation used in quantum circuits. For a two qubit state their composite state can eventually be expressed as tensor product, if the individual states are known

$$\begin{aligned} |\phi\rangle_1 \otimes |\psi\rangle_2 &= (\alpha_\phi |0\rangle + \beta_\phi |1\rangle)_1 \otimes (\alpha_\psi |0\rangle + \beta_\psi |1\rangle)_2 = \begin{pmatrix} \alpha_\phi \alpha_\psi \\ \alpha_\phi \beta_\psi \\ \beta_\phi \alpha_\psi \\ \beta_\phi \beta_\psi \end{pmatrix} \\ &= \alpha_\phi \alpha_\psi |00\rangle + \alpha_\phi \beta_\psi |01\rangle + \beta_\phi \alpha_\psi |10\rangle + \beta_\phi \beta_\psi |11\rangle. \end{aligned} \quad (2.10)$$

However, there are also states that can not be represented as tensor product of individual basis states and consequently are called entangled states. To understand how such a state can be created by basic manipulations let us introduce the *Hadamard*

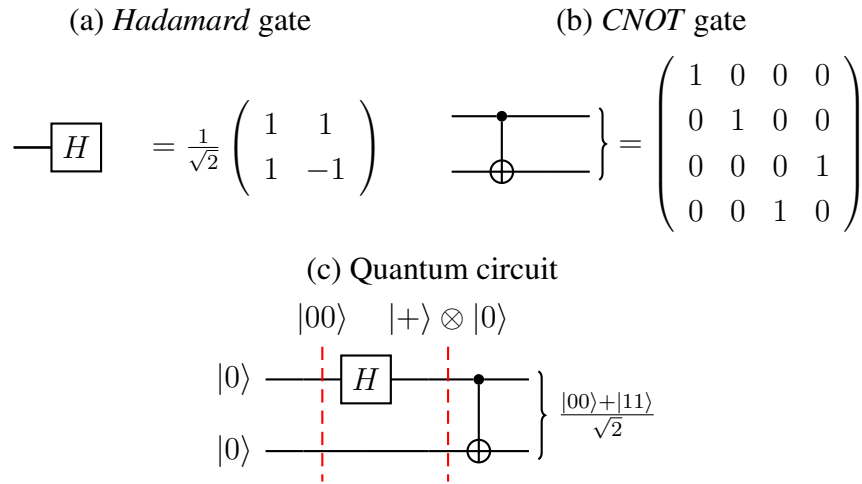


Figure 2.2: (a) **Quantum circuit notation and Matrix representation of the *Hadamard* gate.** This single qubit gate is able to produce a superposition state with equal weights, when applied to a diagonal basis state and in general acts as rotation by π around the $(x+z)$ -axis. (b) **Quantum circuit and Matrix representation of the *CNOT* gate.** Two qubit gate, which flips the target qubit (lower black line) if the control qubit (upper black line), is in the $|1\rangle$ state. (c) **Schematic quantum circuit to create an entangled state from a product state.** Each qubit is represented by a black horizontal line. The initial state is shown on the left, the final state on the right. Quantum gates are applied sequentially from left to right on the input states. Vertical red lines mark imaginary time steps for remarks on intermediate states.

and *CNOT* gates together with the formalism for quantum algorithms in Figure 2.2. The *Hadamard* gate is a single qubit gate and can be written as a 2×2 matrix as displayed in Figure 2.2(a). If applied to the state $|0\rangle$, it creates the symmetric superposition state $|+\rangle$ from Equation 2.8 and applied to $|1\rangle$ results in the respective antisymmetric state $|-\rangle$. The action on a general state on the Bloch sphere can be envisioned as a rotation by π around the $(x+z)$ -axis. The *CNOT* gate whose matrix representation is shown in Figure 2.2(b), is called a two qubit gate, since it has two input and two output qubits. It preserves the control (C) qubit, but flips the second qubit selectively, only if the control qubit is in state $|1\rangle$ and leaves it unchanged otherwise. Quantum circuits are displayed with one horizontal black line per qubit and the initial state of each qubit is shown on the left hand side. Gates are applied iteratively from left to right. In Figure 2.2(c) the system is initialized with two qubits in their $|0\rangle$ state, so the system is in the state $|00\rangle$ at the first red vertical dashed line. In the first time step qubit 1 is changed by the application of a *Hadamard* gate $H|0\rangle = |+\rangle$ and the second qubit is unchanged. Therefore, when considering the

2.2 Universal gateset

state at the time of the second red vertical dashed line, the state can still be expressed as a tensor product $|+\rangle \otimes |0\rangle = \frac{1}{\sqrt{2}}(|00\rangle + |10\rangle)$. In the next timestep a *CNOT* gate is applied. Acting on the $|00\rangle$, the first entry of the state is the control qubit and the second entry the target qubit. Since the control qubit is $|0\rangle$, the target qubit is not flipped resulting in $|00\rangle$. In the case of $|10\rangle$ the control qubit is in the $|1\rangle$ state and therefore the second qubit gets flipped resulting in the $|11\rangle$ state. The combined state $|\psi\rangle$ after this short quantum circuit can be written down as

$$|\psi\rangle = \frac{|00\rangle + |11\rangle}{\sqrt{2}}. \quad (2.11)$$

This state is known as the Bell state, which is an archetype for the class of entangled states since it is maximally entangled. Entangled states can not be represented as tensor products of individual pure one qubit states. The qubits contained in such a state are correlated, so if one would execute a projective measurement of the Z component on a single qubit, this would also affect the second qubit even though it is not directly acted on. On the one hand the entanglement of states is an important ingredient in quantum algorithms, which enables the improvements over classical algorithms. However, at the same time it introduces a crucial limitation to the kind of measurements we are allowed to do, if we do not want to destroy our current state. This phenomenon is known as the collapse of the wave function and can already be seen at the single qubit level. The notion of a measurement of a given operator is associated with its eigenvalues and eigenstates. For the example of $|\psi\rangle = \alpha|0\rangle + \beta|1\rangle$ and a measurement of the Z component the value 1 will be obtained with probability $P(1) = \|\alpha\|^2$ and the value -1 with probability $P(-1) = \|\beta\|^2$, but the state after the measurement will no longer be in the superposition but in one of the eigenstates. In Section 3.3 we will see how it is possible to design projective measurements, which project into degenerate subspaces and thereby do not cause a collapse of the wavefunction. Just as the *AND*, *OR* and *NOT* form a set of gates, which allows for universal manipulations of bits on a classical computer, it is proven that the gateset of the one qubit rotations combined with the *CNOT* gate allows for universal quantum computing in the sense that arbitrary unitary operations can be broken down into a concatenation of this discrete gateset [35]. There are other gate sets, which allow for universal unitary operations. A detailed description can for example be found in [15] or [36].

2.3 Quantum algorithms

We already noted that quantum computing allows for fundamental improvements over classical computing, but to be more instructive on this point let us highlight some of the details of one of the first algorithms, which proved this already in 1992 [37]. The Deutsch-Jozsa algorithm considers a hidden boolean function $f(b_1, b_2, \dots, b_n)$ with n input bits and one output bit b_{out} , where all inputs and outputs are restricted to be either 0 or 1. The function is a priori known to be either balanced or constant in the output, where balanced implies that considering all possible 2^n combinations of input parameters there are exactly half of them mapped to 1 and half to 0. If a function is constant, it would map all possible inputs to only one output value either 0 or 1. An algorithm is then required to determine if the function f is balanced or constant. Considering the worst case scenario classically it would require $2^{n-1} + 1$ evaluations of input states since it is possible, even though not likely, that the first half with 2^{n-1} combinations is exactly the one half input parameters, which results in one of the output values, and the $(2^{n-1} + 1)$ th evaluation results in the opposed value. However, if the $(2^{n-1} + 1)$ th evaluation also results in the initial value, the function is constant, since it can not be balanced anymore. The quantum mechanical

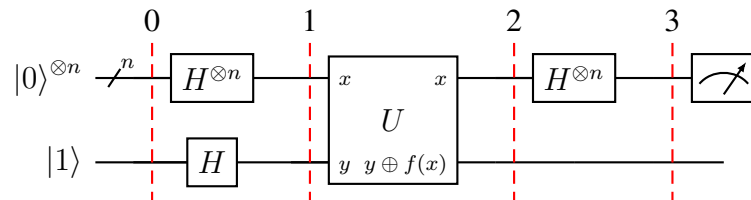


Figure 2.3: Quantum gate structure of the Deutsch-Jozsa algorithm. If the input for the target function f is of length n , there are n qubits initialized in the $|0\rangle$ state and one additional qubit in the $|1\rangle$ state. Each qubit is acted on by a *Hadamard* gate before the unitary quantum oracle is applied. Before the first n qubits are measured they are again exposed to a set of n *Hadamard* gates. Vertical red lines denote the timesteps.

algorithm designed with the gate structure as displayed in Figure 2.3 is always able to distinguish between the two options by only one evaluation of the function f independent of the number of inputs. The function f needs to be implemented as a unitary operation, which transforms a $n + 1$ qubit state $|x\rangle \otimes |y\rangle$ to $|x\rangle \otimes |y \oplus f(x)\rangle$, where \oplus is an addition modulo 2. This unitary is also called quantum oracle. The algorithm can be divided into 4 time steps:

Timestep 0

The system is initialized as product state with n qubits in the $|0\rangle$ state and one qubit in the $|1\rangle$ state. The first n qubits are drawn as one line for simplicity in Figure 2.3.

$$|\psi_0\rangle = |0\rangle^{\otimes n} \otimes |1\rangle \quad (2.12)$$

Timestep 1

Apply one *Hadamard* gate on every qubit transforming the $|0\rangle$ and $|1\rangle$ states into the symmetric and antisymmetric superposition states from Equation 2.8

$$\begin{aligned} H|0\rangle &= |+\rangle \\ H|1\rangle &= |-\rangle \end{aligned} \quad (2.13)$$

The product of the n symmetric and one antisymmetric states can be written as

$$|\psi_1\rangle = |+\rangle^{\otimes n} \otimes |-\rangle = \frac{1}{\sqrt{2^{n+1}}} \sum_x^{2^n} |x\rangle (|0\rangle - |1\rangle) \quad (2.14)$$

where the sum is running over all 2^n possible combinations of n qubit states.

Timestep 2

The application of the quantum oracle results in

$$\begin{aligned} |\psi_2\rangle &= \frac{1}{\sqrt{2^{2n+1}}} \sum_x^{2^n} |x\rangle (|0 \oplus f(x)\rangle - |1 \oplus f(x)\rangle) \\ &= \frac{1}{\sqrt{2^{2n+1}}} \sum_x^{2^n} |x\rangle (|f(x)\rangle - |1 \oplus f(x)\rangle) \\ &= \frac{1}{\sqrt{2^{2n+1}}} \sum_x^{2^n} (-1)^{f(x)} |x\rangle (|0\rangle - |1\rangle) \\ &= \frac{1}{\sqrt{2^n}} \sum_x^{2^n} (-1)^{f(x)} |x\rangle \otimes |\varphi\rangle \end{aligned} \quad (2.15)$$

since for each x , $f(x)$ will either be 0 or 1 and the $-$ sign can be brought to the front.

Timestep 3

For the evaluation the antisymmetric state $|\varphi\rangle = \frac{1}{\sqrt{2}}(|0\rangle - |1\rangle)$ is not important anymore after the quantum oracle. The first n qubits are acted on again by a

Hadamard gate.

$$\begin{aligned}
 |\psi_3\rangle &= H^{\otimes n} \otimes \mathbb{1} |\psi_2\rangle \\
 &= (H^{\otimes n} \otimes \mathbb{1}) \frac{1}{\sqrt{2^n}} \sum_x^{2^n} (-1)^{f(x)} |x\rangle \otimes |\varphi_1\rangle \\
 &= \frac{1}{\sqrt{2^n}} \sum_x^{2^n} (-1)^{f(x)} \frac{1}{\sqrt{2^n}} \left[\sum_z^{2^n} (-1)^{x \cdot z} |z\rangle \right] \otimes |\varphi_1\rangle \\
 &= \frac{1}{2^n} \sum_x^{2^n} \left[\sum_z^{2^n} (-1)^{f(x)} (-1)^{x \cdot z} |z\rangle \right] \otimes |\varphi_1\rangle
 \end{aligned} \tag{2.16}$$

where $x \cdot z = x_1 z_1 + \dots + x_n z_n$ is the scalar product of the amplitudes.

Measurement

It is sufficient to measure the Z component of the n qubit state once. Let us therefore consider the two options of $f(x)$.

Constant

In this case the function $f(x)$ is always giving 0 or 1. If it evaluates to 0, the factor $(-1)^{f(x)}$ is always 1, so the unitary operation has no effect on the n qubit state. Since the *Hadamard* gate is its own inverse $HH = \mathbb{1}$, the final state before the measurement will be $|0\rangle^{\otimes n}$. Therefore if we measure the Z component, we will get $P(|0\rangle^{\otimes n}) = 1$. If $f(x)$ is constantly evaluated to 1, the factor $(-1)^{f(x)}$ results in an overall -1 prefactor and following the above reasoning the state before measurement will be $-|0\rangle^{\otimes n}$. But this prefactor is not affecting the probability of measuring $P(|0\rangle^{\otimes n}) = 1$. Therefore if $f(x)$ is constant, we will always measure $|0\rangle^{\otimes n}$ with 100%.

Balanced

If the function $f(x)$ is evaluated equally often to 0 or 1, the symmetric n qubit superposition state after the first set of *Hadamard* gates will be rotated into an antisymmetric state with half of the complex weights being -1 . The state after the quantum oracle is therefore orthogonal to the one before the oracle. The second *Hadamard* gate will therefore change the state after the oracle into a state orthogonal to $|0\rangle^{\otimes n}$. The probability changes to $P(|0\rangle^{\otimes n}) = 0$ and we can deduce a balanced function if we do not measure $|0\rangle^{\otimes n}$.

With this one carefully chosen measurement the Deutsch-Josza algorithm therefore outperforms any classical algorithm. This algorithm might seem somewhat artificial

2.3 Quantum algorithms

in the sense that the problem is rather theoretical and there might not be a directly useful application. However, to date there are already numerous other quantum algorithms proposed with superior scaling compared to their classical counterparts and directly practical use cases even outside academia like Shor's algorithm [5], which is capable of prime factor decomposition, which is the backbone of modern cryptography.

Chapter 3

Quantum error correction

The quantum superposition states, which are created for example in the Deutsch-Josza algorithm in Section 2.3, evolve perfectly unitary in theory. However, they are rather fragile in reality, since the unitary evolution holds only for a complete system. Theoretically one can imagine a perfectly isolated quantum mechanical system with no interaction at all to the outside world to reduce noise. The protection from external noise is already attempted in realizations like trapped-ion quantum information processors [38], where information is stored in ions, kept at fixed positions via electric fields isolated in a vacuum environment. Quantum gates as introduced in Section 2.2 are implemented as microwave or optical signals acting on individual ions. However, no vacuum in any lab is perfect, nor are the external signals acting on the trapped ions free from noise. This inevitably results in decoherence of the superposition states and thereby to errors in the stored information. Building reliable scalable quantum computing hardware therefore is going to require error correction schemes. Since measurements are impacting quantum states and due to the fact that a quantum state can not be cloned [39], classical error correction schemes can not be implemented directly for quantum computers. In this chapter we will first introduce the notion and the formalism of quantum error channels and mixed quantum states. Classical repetition codes are discussed in Section 3.2. Shor's repetition algorithm inspired by the classical repetition codes is discussed in Section 3.3. The Stabilizer formalism is introduced in respect of the example of the Toric code in Section 3.4. In the following the mapping of these error correction codes to statistical physical models will be discussed for the Toric code in Section 3.5 and conclude with the introduction of the X-cube model and its respective statistical physics models in Section 3.6.

3.1 Quantum error channels

For an effective correction of errors it is necessary to know, which types of errors can affect the system of interest and at what rate they are appearing. For a classical bit, the only type of error channel that can occur, is a bit-flip error where a stored zero is turned into a one and vice versa. The bit string is changed, and the computation eventually proceeds using the faulty sequence. For a qubit, representable as quantum state on the bloch sphere, there are qubit flip errors, which can be represented as \hat{X} operator, acting on the respective qubit, but there can also be phase-flip errors, whose effects are represented by \hat{Z} operators or combinations thereof, which can be represented by \hat{Y} operators. Let us consider a qubit state $|\psi\rangle$, and with a certain probability (rate of error) p it is affected for example by a qubit flip error \hat{X} , acting on it as $\hat{X}|\psi\rangle = |\psi'\rangle$. This state can no longer be represented by a pure state but, needs the density operator ρ . The density operator can represent pure states and mixed states as weighted averages

$$\rho = \sum_i p_i |\psi_i\rangle\langle\psi_i|, \quad (3.1)$$

where p_i is the probability of being in state $|\psi_i\rangle$. For a pure unaffected state there is only one state $|\psi\rangle$ with $p = 1$, and the density matrix can be written as $\rho = |\psi\rangle\langle\psi|$. In the above example of a qubit flip error with probability p the mixed state can be represented by the density operator

$$\begin{aligned} \rho &= (1 - p) |\psi\rangle\langle\psi| + p |\psi'\rangle\langle\psi'| \\ &= (1 - p) |\psi\rangle\langle\psi| + p \hat{X} |\psi\rangle\langle\psi| \hat{X}^\dagger. \end{aligned} \quad (3.2)$$

The effect of a general error channel \mathcal{E} with multiple error operators \hat{O}_i with error probabilities p_i can therefore be written as

$$\mathcal{E}(\rho) = \sum_i p_i \hat{O}_i \rho \hat{O}_i^\dagger. \quad (3.3)$$

Before we discuss how to correct or even detect errors, let us consider how classical error correction is capable of correcting faulty bits.

3.2 Classical error correction

Classical information can easily be read out and copied. The likelihood of information loss can therefore be reduced by storing bits redundantly. The basic idea is to store the information, which would require n classical bits for storage in a larger bit string

3.2 Classical error correction

with $m > n$ bits. If the damage, caused by bit-flip errors, is not too severe, the information can still be read out without errors from the redundant bits. Let us consider the simplest example for such a repetition code, the $(3, 1)$ –Hamming code, which consists in total of three bits and one logical data bit. The three bits allow for a total of $2^3 = 8$ possible binary bit strings, which are the state space. There are 2^1 code states, which are denoted as code subspace, and can be chosen as 000 and 111. The underlying notion of the Hamming distance is the number of bits, which need to be flipped from one state to obtain the other state. Therefore the two valid code states have a Hamming distance of $d(000, 111) = 3$. Codes are classified to have a distance of d , if all valid code states have at least a distance of d to all other code states. All states from the state space, which are not code states, are therefore known to contain at least one faulty bit, if they occur during processing. They can be classified according to their distance to any of the valid code states as shown in Table 3.1. Error correction is therefore possible, if only one bit is corrupted in a single

code state 1	d=1 to 000	d=1 to 111	code state 2
	100	011	
000	010	101	111
	001	110	

Table 3.1: Possible bit strings of length 3. 000 is identified with the first code state and 111 with the second valid code state. All other possible bit strings have either $d = 1$ or to $d = 2$ to the code states respectively. Error recovery is feasible if only one bit is corrupted.

time step between two measurements of the bit string by identifying, which code state has the minimal Hamming distance to the found bit string. Error detection, however, is possible as long as there are at most two bits flipped in a time step, even though this error can not be corrected properly, as it is not possible to know, which-one was the valid code state. With a minimum of three errors it is theoretically possible that errors occur, and are not detectable.

Using the same logic, one can construct other codes with larger distances, e.g. a $(5, 1)$ code with distance $d = 5$ would allow for the recovery of 2 faulty bits and the detection of 4 faulty bits. If the distance is kept constant at $d = 3$, there are other optimal (N, k) –Hamming codes for any integer $r \leq 2$ with $N = 2^r - 1$ total bits and $k = 2^r - r - 1$ data bits and $n = N - k$ parity bits [40]. The code rate grants information on the percentage of bits containing information. While this is only $1/3 = 33, 3\%$ for the $(3, 1)$ –Hamming code, the rate rapidly improves, if the distance

is kept constant at $d = 3$ to above 96% with $n = 8$ parity bits.

In classical computers today's hardware is working very reliable with typical raw bit error rates in memories smaller than 10^{-6} [41], which corresponds to one faulty bit in 10^6 stored bits. This raw bit error rate is measured before any error correction is applied. With error correction the error rate is further reduced and for certain hardware platforms uncorrectable bit error rates of $10^{-13} - 10^{-16}$ are achieved [41].

3.3 Shor's repetition algorithm

As already noted in Section 3.1 quantum states are not solely subject to bit-flip errors inflicted by \hat{X} , but can also be acted upon by \hat{Y} or \hat{Z} as a result of an error channel. An arbitrary measurement of a qubit state projects it into the eigenspace of the measurement operator and thereby most likely will change the measured quantum state. The only exception would be that the qubit was already in an eigenstate of the measurement operator. Due to the no-cloning theorem [39] a direct implementation of the repetition code is not possible, since we can not create an exact copy of an arbitrary state. However, there are codes, like the "9-qubit code" proposed by Shor, which encode one logical qubit in nine physical qubits, trying to recover from any individual error in the physical qubits. In his version the code states are defined to be [42]

$$\begin{aligned} |0\rangle &\rightarrow \frac{1}{2\sqrt{2}}(|000\rangle + |111\rangle)(|000\rangle + |111\rangle)(|000\rangle + |111\rangle), \\ |1\rangle &\rightarrow \frac{1}{2\sqrt{2}}(|000\rangle - |111\rangle)(|000\rangle - |111\rangle)(|000\rangle - |111\rangle). \end{aligned} \quad (3.4)$$

These states can be created by similar gate circuits as demonstrated in Figure 2.2(c). A central limitation for recovery is that only one qubit is decohered, since error correction is not possible otherwise. The algorithm does not measure the individual states in a certain basis and calculates the respective minimal distances to the code states. Instead it is based on projective measurements. For illustrative purposes let us consider the easier example of a 3-qubit code, which is able to correct a single bit-flip error [43]. A single phase-flip error would also be correctable respectively, if the notation would be slightly changed. The code encodes an arbitrary state $|\psi\rangle = \alpha|0\rangle + \beta|1\rangle$ into a 3-qubit state $|\psi'\rangle = \alpha|000\rangle + \beta|111\rangle$, which is then transmitted and subject to noise. This can be achieved by the application of *CNOT* gates as shown in the first timestep in Figure 3.1. After the encryption the transmission of the state is eventually corrupted with bit-flip errors of probability p per qubit.

Afterwards the state is measured with projective two qubit measurements of the form

$$\hat{S} = |00\rangle\langle 00| + |11\rangle\langle 11| - |01\rangle\langle 01| - |10\rangle\langle 10| \quad (3.5)$$

once for the qubits one and two and once for two and three. The measurement

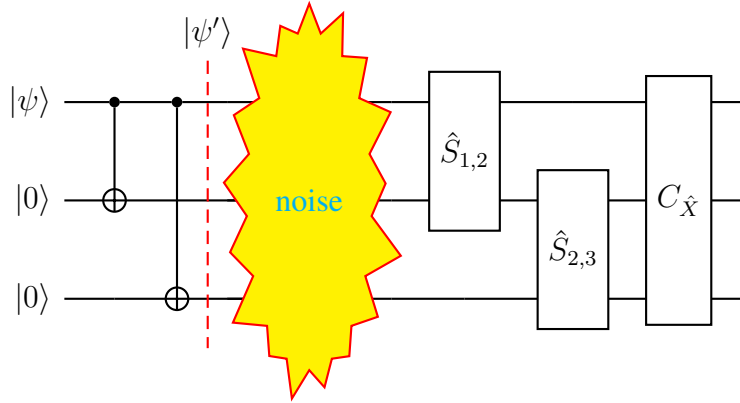


Figure 3.1: Quantum circuit for the 3-qubit code for bit-flip error correction. The entangled state $|\psi'\rangle = \alpha|000\rangle + \beta|111\rangle$ is created by the successive execution of *CNOT* gates. The noise is inflicting a bit-flip in each qubit with probability p . The projective measurement operator outputs decide, if $C_{\hat{X}}$ is flipping one of the three qubits to recover an eventual bit-flip. If the eigenvalues $\lambda_{1,2} = 1$ corresponding to $S_{1,2}$, and $\lambda_{2,3} = -1$, corresponding to $S_{2,3}$, were measured, it would indicate that the third qubit was flipped by the noise, and $C_{\hat{X}} = \mathbb{1} \otimes \mathbb{1} \otimes \hat{X}$ would flip the third qubit back, trying to correct for the most likely error channel when $p < 0.5$.

outcome is degenerate with the eigenvalue $\lambda = +1$, corresponding to aligned measured qubits, and the eigenvalue $\lambda = -1$ corresponding to antiparallel states. In this manner the quantum state is not affected, since the two qubit quantum state is already in the eigenspace before the measurement. However, due to the degeneracy we only get information about the parity of the two measured qubits. If $+1$ is measured, the two qubits are aligned and therefore possibly belong to one of the code states, which are completely aligned. With a -1 measurement we know that one qubit must have been subject to a bit-flip, but do not know, if it was the first or the second qubit. However, the second projective two qubit measurement, acting on qubits two and three lets us deduce, which of the three qubits was flipped by a majority rule, and the faulty qubit can be corrected by a respective application of the bit-flip operator \hat{X} . The quantum circuit is displayed in Figure 3.1.

The fidelity is a common measure of closeness of two quantum states. In the

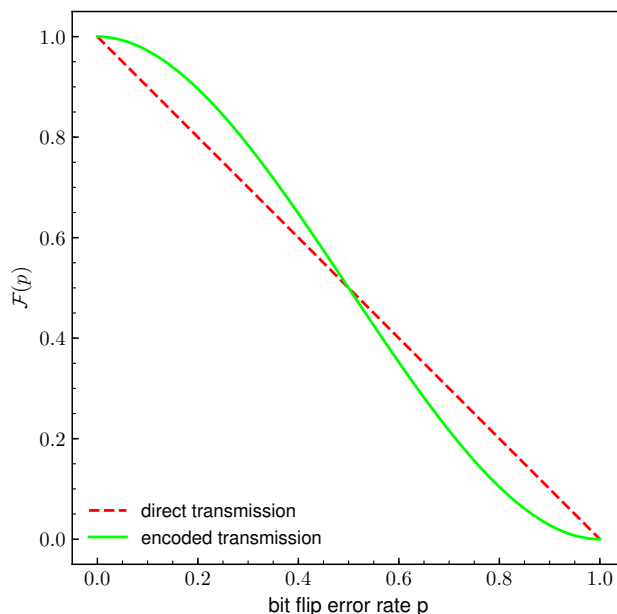


Figure 3.2: Fidelities for a direct transmission on a noisy channel or a transmission via the same noisy channel of a qubit, encoded with the 3-qubit code, as displayed in Figure 3.1. For $p < 0.5$ the fidelity can be increased by the encoding if the errors occur independently and measurements and gate operations are executed perfectly.

general case with two density matrices ρ and σ their fidelity is given by

$$\mathcal{F}(\rho, \sigma) = \left(\text{tr} \sqrt{\sqrt{\rho} \sigma \sqrt{\rho}} \right)^2. \quad (3.6)$$

In the special case of pure states $\rho = |\psi_\rho\rangle\langle\psi_\rho|$ and $\sigma = |\psi_\sigma\rangle\langle\psi_\sigma|$ the fidelity can be reduced to the overlap $\mathcal{F}(\rho, \sigma) = \|\langle\psi_\rho|\psi_\sigma\rangle\|^2$.

The fidelity of the final state and the target state without the 3-qubit code will be $\mathcal{F} = (1 - p)$, if p is the error probability per qubit. The respective encoded fidelity evaluates to $\mathcal{F} = (1 - p)^3 + 3p(1 - p)^2$, since the error correction scheme will succeed if no bit was flipped and in the case, if a single bit was flipped. The comparison can be seen in Figure 3.2.

Even though this procedure allows for a reduction of errors for small values of p , a perfect execution of manipulation and measurement operations was assumed, as well as an independence of errors. In theory further improvement might be possible by this strategy through a simple concatenated encoding with these assumptions. However, in real devices every manipulation of the system, even single qubit gates, like e.g. the \hat{X} operator, come with some inherent error probability. Therefore any theoretical improvement might be diminished by the computational overhead of the encoding.

Consequently it was proposed to build a fault-tolerant quantum computer [44, 45], where a single logical qubit is not only encoded in an ensemble of qubits, but the information is inherent in the topology of the system [46, 47], which can not easily be affected by local errors and thus is more resilient on a hardware level.

3.4 Stabilizer codes

The Toric code [46, 47] is an encoding of two logical qubits into $2L^2$ physical qubits. The physical qubits reside on the links of a 2D L times L square lattice, where opposite ends of the lattice are considered to be adjacent. It can be pictured as a square lattice residing on a torus or a square lattice with periodic boundary conditions. It belongs to the class of stabilizer codes [48, 49], which use mutually commuting check operators \hat{S}_i that fix the code states of the system

$$\hat{S}_i |\psi\rangle = (+1) |\psi\rangle, \quad \forall \hat{S}_i \quad (3.7)$$

in a similar way as the projective measurements in Equation 3.5. The code states are mutual eigenstates to the eigenvalue $\lambda = +1$ for all check operators. The check operators are tensor products of the two times two identity matrix $\mathbb{1}$ and the Pauli matrices, defined in Equation 2.6, acting on the physical qubits.

In the case of the Toric code there are two types of stabilizers attached to the lattice as demonstrated in Figure 3.3. X_v check operators are acting nontrivially on the four links (qubits) joined at a vertex v with

$$X_v = \otimes_{l \in v} \hat{X}_l \quad (3.8)$$

times the identity for all other lattice sites. Z_p check operators are associated with a plaquette p and act nontrivially on the four surrounding links as

$$Z_p = \otimes_{l \in p} \hat{Z}_l, \quad (3.9)$$

with identities $\mathbb{1}$ applied to all other qubits. The stabilizers are mutually commuting, since they either act on disjoint qubits, in which case the commutator is zero trivially, or act on two joint qubits, where it is also possible to show that the commutator evaluates to zero. Vertex check operators are commuting with vertex check operators and plaquette stabilizers among one another. The set of all these check operators generates an Abelian group, which is called the code stabilizer \mathcal{S} . It defines the code

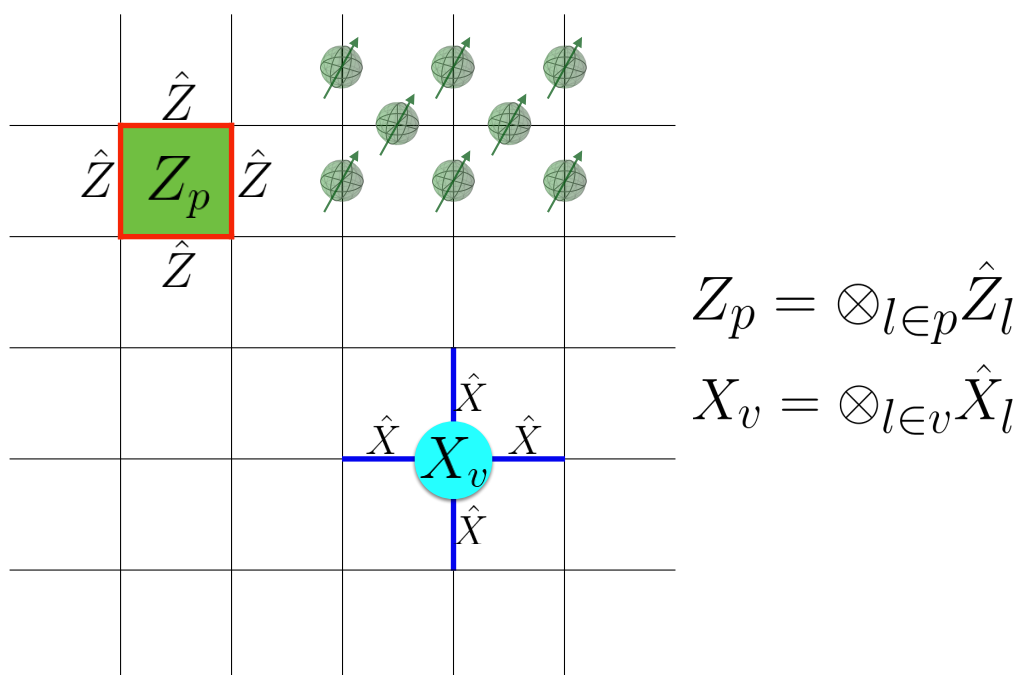


Figure 3.3: Square 2D lattice with periodic boundary conditions and Toric code stabilizers. Qubits, which are represented symbolically by green bloch spheres, are residing on every lattice site and are in one to one correspondence to the links of the lattice. Qubits residing on the top row, are identified by those in the bottom row, and qubits on the left column are identified with those on the right column, respectively due to the periodic boundary conditions. Check operators Z_p are residing on each plaquettes p and act with \hat{Z} operators on the four adjacent links (qubits), marked in red for the green plaquette. Complementary check operators X_v reside on every vertex v , exemplarily depicted in turquoise, with operators \hat{X} acting on the four adjacent blue links.

states \mathcal{C} as states from the $2L^2$ qubit Hilbert space \mathcal{H} that are mutual eigenstates with $\lambda = +1$ for all the check operators

$$\mathcal{S} = \{|\psi\rangle \in \mathcal{C} : Z_p |\psi\rangle = (+1) |\psi\rangle, X_v |\psi\rangle = (+1) |\psi\rangle \mid \forall v, p\}. \quad (3.10)$$

The check operators are not completely independent from each other. The periodic boundary conditions are fundamental for the encoding, since they allow for an expression of every vertex or plaquette check operator as product of all other $L^2 - 1$ respective vertex or plaquette check operators. Therefore the code subspace is four

dimensional, which allows for an encoding of two qubits [25, 50]. The Toric code is a Calderbank-Shor-Steane (CSS) code [48, 51], meaning that each check operator is purely a tensor product of either \hat{X} or \hat{Z} operators, but not combinations thereof. CSS codes thus allow for an independent correction of bit-flip and phase-flip errors.

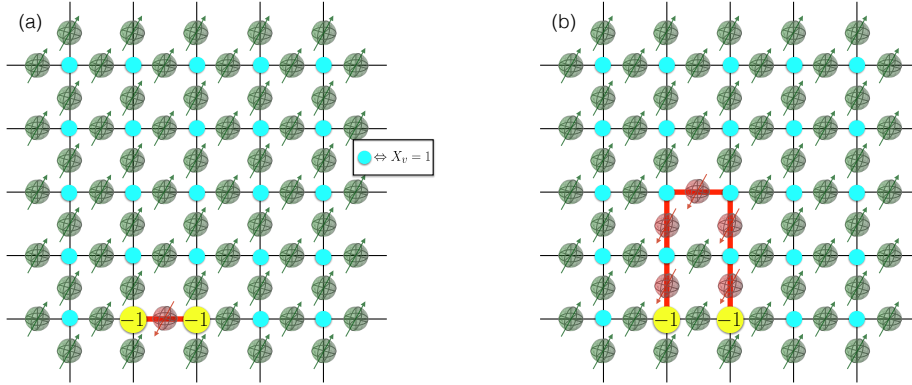


Figure 3.4: (a) **Error syndrome of a single bit-flip error:** Starting with a code state the measurement X_v and Z_p would return $+1$ for all vertices and plaquettes. Correct measurements of $X_v = +1$ are denoted by turquoise dots. A single phase-flip error occurring at the red link leaves results in a state outside the code space. The adjacent X_v operators will return -1 , if measured, which is denoted by yellow dots. The configuration of all yellow dots is called the error syndrome. (b) **Same error syndrome caused by an error chain:** An error syndrome is highly ambiguous and can be caused by many different error chains. If errors somehow happen to affect adjacent qubits, the individual errors form a chain, wherein all intermediate X_v operators are unaffected, since they are adjacent to an even number of faulty qubits, and the minus signs cancel. Only at the boundary of such a chain the measurement will return -1 . After a measurement of all check operators it is therefore unknown, which error chain E caused the syndrome.

Let us consider the effects of phase errors of qubits on the measurement values of the stabilizer operators of X_v . An isolated faulty bit, residing on a link, will cause the two adjacent X_v operators to measure -1 as shown in Figure 3.4(a). A correction could be achieved by applying a Pauli operator, consisting of a tensor product of \hat{Z} and $\mathbb{1}$, with weight $w = 1$, on the qubit between two defects. The weight w of a Pauli operator is the number of qubits, it is acting upon nontrivially. The configuration of the defects is called an error syndrome. It is highly ambiguous, and whilst the qubit configuration shown in Figure 3.4(a) might be the most likely configuration, if the error rate p is small, there are other possible qubit configurations, which cause the very same syndrome as shown in Figure 3.4(b). Error chains E are constituted

by faulty qubits, which are adjacent as shown in Figure 3.4(b). The endpoints of such a chain are called boundary, and in general error chains with the same boundary cause the same syndrome. This might appear as a severe problem at first, since it is unknown, what the actual error chain causing the syndrome was.

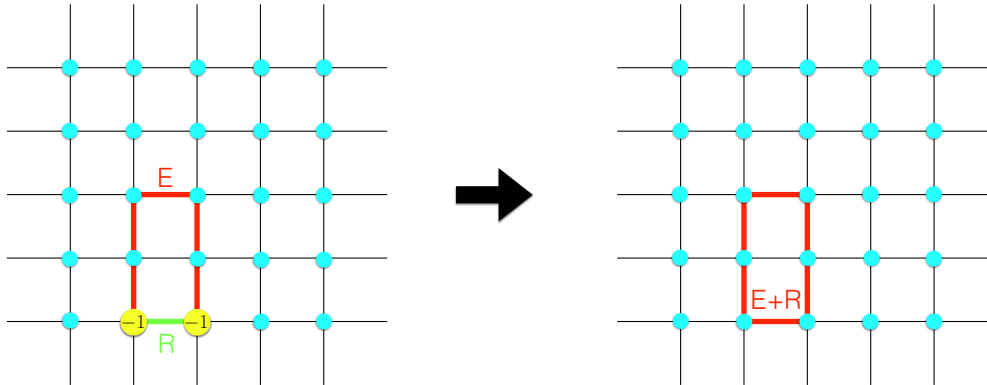


Figure 3.5: Simplified notation of an error syndrome with an error chain: The individual qubits on the chain are only represented by the links for simplicity. An error chain E can be denoted by red links, while black links represent unaffected qubits. The configuration of the yellow dots denotes the syndrome of the caused error. Error recovery is eventually possible by the application of a recovery chain R . It is chosen exemplary as the Pauli operator with the smallest weight. It succeeds if $E + R$, consisting of the actual error chain E , which is unknown, and the recovery chain R form a homologically trivial cycle.

However, due to the construction of the check operators by simply always applying the recovery chain R with the Pauli operator of the shortest distance as depicted in Figure 3.5 it turns out that either we have chosen the correct faulty bits and directly successfully recovered the error, or by the application we created a cycle $E + R$ that is a chain whose boundary is trivial. $E + R$ denotes the disjoint union of E and R , which contains all the links acted on by \hat{Z} that are solely in E or R . There are two distinct types of cycles, which are showcased in Figure 3.6. A homologically trivial cycle bounds a region, which can be tiled by plaquettes as shown in Figure 3.6(a), and the corresponding tensor product of Z_p operators is part of the stabilizer and thus does not affect the encoded information, as it is acting trivially upon a code state. Non-trivial cycles, however, could also be created as depicted in Figure 3.6(b), which span across the boundary of the system. The tensor product corresponding to these cycles commutes with the stabilizer, but is not contained therein. It therefore preserves the code subspace, but affects the encoded information. If we create

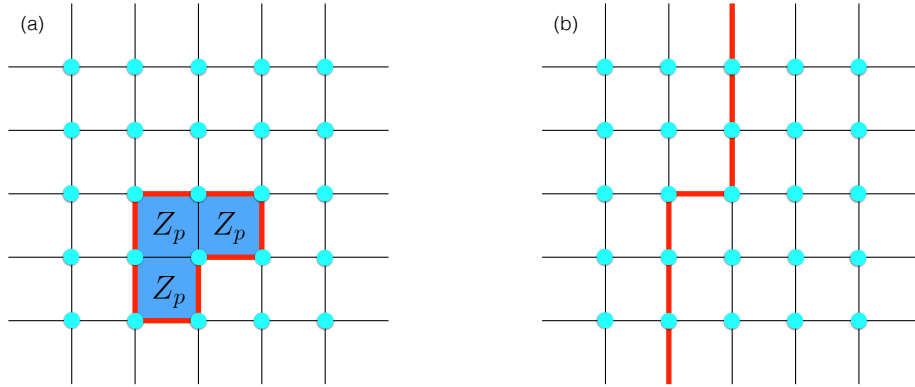


Figure 3.6: (a) **Homologically trivial cycle:** A cycle \mathcal{C} depicted by red links, which surrounds an area of plaquettes, has an even number of \hat{Z} acting on the system. In the displayed case the action can be simulated by enacting with the three respective Z_p plaquette operators on the system. This action is trivial for any code state by construction due to Equation 3.10. (b) **Homologically non-trivial cycle:** A cycle, which spans the system beyond a boundary, can not be represented as boundary of plaquette operators. Therefore it commutes with all check operators, but is not contained in the stabilizer. An error chain E of this form could not be detected in the first place. However, an open Error chain beyond the boundary might be corrected falsely by connecting it to a homologically non-trivial cycle.

non-trivial cycles $E + R$ during the correction process, error correction has failed. The objective of an error correction scheme therefore can be reduced to assignment of an error syndrome to a most likely homology class. If the homology class is chosen correctly, error correction can be achieved by constructing a homologically trivial cycle $E + R$. To span the system, an error chain has to consist of at least L faulty qubits, thus the code distance of the Toric code is said to be L . Let us now proceed to a more precise statistical analysis of the errors, which are appearing in the limit of large systems, and if it is possible to determine the most probable homology class given a syndrome.

3.5 Mapping to classical spin systems

In practise in each time step a measurement of all check operators will be necessary. As the measured parity in the 3-qubit code in Section 3.3 provided the information where a bit-flip operation has to be applied, here the measured syndrome will serve as an input for the error recovery process. However, for the Toric code the error syndrome is highly ambiguous. Thus instead of always applying the Pauli operator

with the smallest weight, as considered in the previous section, a classical calculation would need to decide in which of the possible homologically distinct ways recovery chains should be applied in order to always create homologically trivial cycles. It was

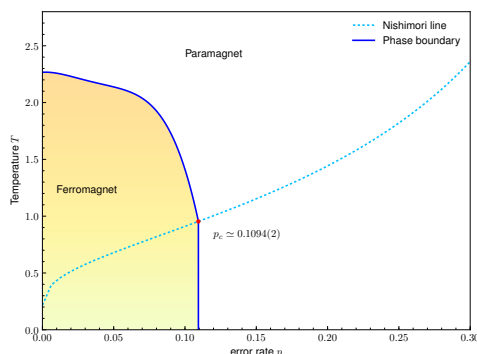


Figure 3.7: Sketched phase diagram of the random-bond Ising model. The Hamiltonian of the system is given in Equation 3.17. At $p = 0$ the random-bond Ising model resembles the isotropic 2D Ising model without any external field $h = 0$. Therefore the critical temperature $T_c = 2.269$ in this limit can be obtained by Onsagers exact solution [52]. The ferromagnetic phase extends to finite p until a critical disorder $p_c = 0.1094(2)$, found by Honecker et al. [53]. Error chains, corresponding to configurations with an error rate $p < p_c$, are correctable. The crossing of the Nishimori line $-2\beta J = \ln \frac{p}{1-p}$ [54, 55] with the phase boundary marks the optimal error threshold, with the critical point $(p_c, T_c(p_c))$.

realized by Dennis et al. [25] that in the example of the Toric code the various choices of recovery chains, depicted in Figure 3.5, can be mapped to configurations of the random-bond Ising model. In the $p - \beta$ phase diagram of this well known statistical physics model [53, 56, 57] an ordered and disordered phase can be found. If the syndrome belongs to a configuration in the ordered phase, it is possible in a time polynomial in L to determine the free energy for every possible homology class h of recovery chains [58]. The homology class with the minimal free energy is the most probable one and therefore should yield the highest probability of successful error correction. It is possible to derive an optimal error threshold p_c from the phase diagram [53], which imposes an upper bound on the allowed error rate p , at which errors occur in the physical qubits. For error rates above p_c the determination of a most probable homology class might suffer from exponentially long thermalization times in the disordered phase of the random-bond Ising model, and error correction would therefore not be feasible. Furthermore the quantum threshold theorem [59] states that quantum computing can be performed with arbitrary high precision, if the

quantum hardware used for a code has an error rate $p < p_c$. With the quantum threshold theorem at hand it is possible to compare different quantum error correction codes in a systematic way regarding their inherent necessity on error rates p_c . To

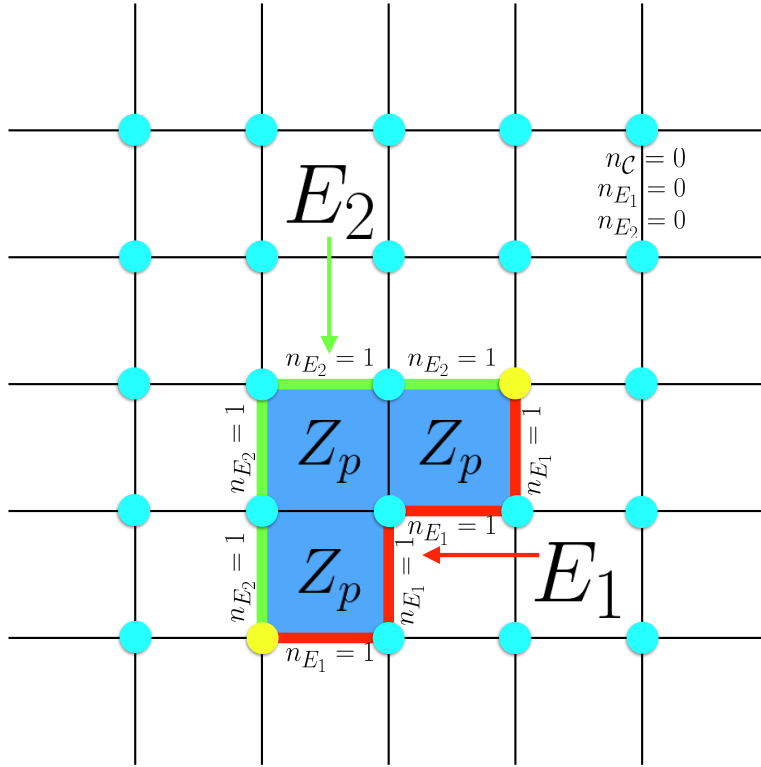


Figure 3.8: Error chains: 1-chains for E_1 and E_2 with $n_{E_1}(l)$ being one on the red links and zero everywhere else, and $n_{E_2}(l)$ is one on the green links and zero on all other links respectively. Black links represent that all 1-chains including $n_C(l)$ are zero at these links. $n_C(l) = 1$ is fulfilled on all links that are either green or red for the cycle $C = E_1 + E_2$.

derive the mapping introduced by Dennis et al. let us first recapitulate the adopted error model. Bit-flip and phase-flip errors are uncorrelated, and occur equally likely with an error rate p . Measurements of the syndrome are executed perfectly, and the errors can be corrected independent of each other. We will consider \hat{Z} errors as in the previous section. For the mapping of error chains to the random-bond Ising model it is useful to introduce the mathematical notion of a \mathbb{Z}_2 -valued 1-chain $n(l)$ displayed in Figure 3.8, where a binary value $\{0, 1\}$ is assigned to every link l . A zero corresponds to a black link without an applied \hat{Z} operator and a one marked by a red link denoted that a \hat{Z} operator acted on this link. A 2-chain assigns

binary values to plaquettes, and 0–chains would correspond to lattice sites. There exists a linear boundary operator ∂ , which takes 2–chains to 1–chains and 1–chains to 0–chains respectively. A 0–chain can therefore be regarded as the boundary, which corresponds to an error syndrome of an error chain represented by a 1–chain. Considering an exemplary fixed error chain E_1 consisting of N_{E_1} faulty qubits with its corresponding 1–chain $n_{E_1}(l)$ the probability for this error chain to appear on a lattice with N qubits can be written as:

$$\begin{aligned} P(E_1) &= (1-p)^{N-N_{E_1}} p^{N_{E_1}} \\ &= \prod_l (1-p)^{1-n_{E_1}(l)} p^{n_{E_1}(l)} \\ &= \left[\prod_l (1-p) \right] \prod_l \left(\frac{p}{1-p} \right)^{n_{E_1}(l)} \end{aligned} \quad (3.11)$$

with the product running over all qubits, residing on the lattice links l . With the choice of E_1 the error syndrome is fixed, but there are other error chains, e.g. E_2 , which have the same error syndrome. Since a cycle \mathcal{C} can be defined as $\mathcal{C} = E_1 + E_2$, we can also express $E_2 = E_1 + \mathcal{C}$ as disjoint union. The respective 1–chains n_{E_2} and $n_{\mathcal{C}}$ assign binary values to each link following the same logic as $n_{E_1}(l)$. The probability of E_2 then depends on the number of contained faulty qubits, and can be written as

$$P(E_2|E_1) = \prod_l (1-p)^{1-n_{E_2}(l)} p^{n_{E_2}(l)}. \quad (3.12)$$

For each lattice link the value of the 1–chain for E_2 can be expressed in terms of the other 1–chains as

$$\begin{aligned} n_{E_2} &= (1-n_{E_1})n_{\mathcal{C}} + (1-n_{\mathcal{C}})n_{E_1} \\ &= n_{\mathcal{C}} + n_{E_1} - 2n_{E_1}n_{\mathcal{C}} \end{aligned} \quad (3.13)$$

since if $n_{\mathcal{C}} = 1$ and $n_{E_1} = 0$, the link will be contained in E_2 , but if $n_{\mathcal{C}} = n_{E_1}$ the link will not be contained in E_2 . Equation 3.12 can therefore be rewritten with Equation 3.11 and Equation 3.13 to

$$\begin{aligned} P(E_2|\partial E_1) &= \prod_l (1-p)^{1-n_{\mathcal{C}}-n_{E_1}+2n_{E_1}n_{\mathcal{C}}} p^{n_{\mathcal{C}}+n_{E_1}-2n_{E_1}n_{\mathcal{C}}} \\ &= \prod_l (1-p)^{1-n_{E_1}} p^{n_{E_1}} \left(\frac{p}{1-p} \right)^{n_{\mathcal{C}}-2n_{E_1}n_{\mathcal{C}}} \\ &= P(E_1) \prod_l \left(\frac{p}{1-p} \right)^{n_{\mathcal{C}}(1-2n_{E_1})} \end{aligned} \quad (3.14)$$

3.5 Mapping to classical spin systems

where the dependency on l of all 1-chains is denoted implicitly. It is possible to define a spin model with classical Ising variable and quenched disorder, whose partition function resembles the probability of the error chains as

$$P(\bar{E}) = \sum_{E_i} P(E_1 + E_i) \propto Z_{E_1}(\beta) = \sum_{\{\sigma_i\}} e^{-\beta H_{E_1}}, \quad (3.15)$$

where \bar{E} is a homology class consisting of all error chains compatible with the found syndrome and sharing the same homology. Thus the sum is running over all recovery chains E_i , whose cycle $E_1 + E_i$ belongs to the same type of homology [60, 61]. H_{E_1} is a spin system with quenched disorder, where the sign of the interactions is determined by the error chain E_1 . The mapping of an exemplary error chain E_1

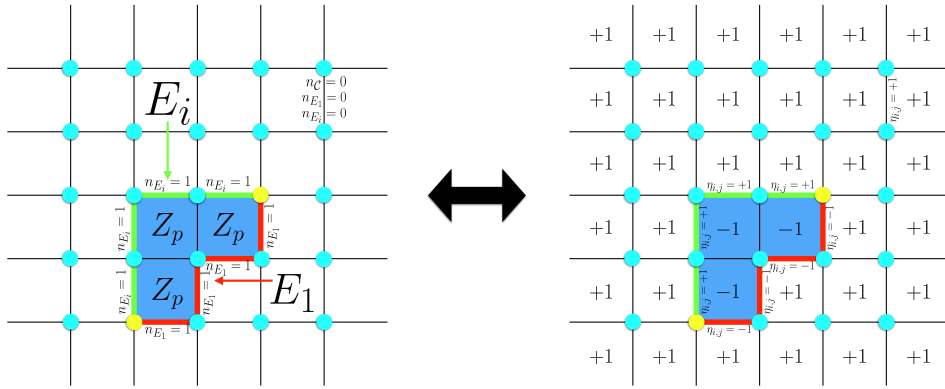


Figure 3.9: Mapping of the error chain to a spin system: The quenched error line E_1 gives rise to the links with antiferromagnetic coupling $\eta_{i,j} = -1$. All other links are ferromagnetic. Ising spins $\sigma \in \{-1, 1\}$ are placed on every plaquette. Along the links marked by $n_{E_1} = 1$ the spins on both sides will try to anti-align to minimize the energy corresponding to Equation 3.17. Every instance of an error chain E_i can be considered as a domain wall of a finite cluster of spins with $\sigma = -1$.

to the respective Ising spin system is showcased in Figure 3.9. A spin $\sigma \in \{-1, 1\}$ resides on every plaquette of the lattice. The interactions are restricted to next neighbour spins $\langle i, j \rangle$ on the square lattice with interaction strengths $\eta_{i,j}$, which are ferromagnetic or antiferromagnetic depending on their affiliation to the error chain E_1

$$\eta_{i,j} = \eta_l = \begin{cases} -1 & \text{if } l \notin E_1 \\ 1 & \text{if } l \in E_1. \end{cases} \quad (3.16)$$

The Hamiltonian is defined as

$$H_E = -J \sum_{\langle i,j \rangle} \eta_{i,j} \sigma_i \sigma_j, \quad (3.17)$$

and the mapping is completed with the relation

$$e^{-2\beta J \eta_{i,j}} = \left(\frac{p}{1-p} \right)^{1-2n_{E_1}} \quad (3.18)$$

between the product of the coupling strength J with the inverse temperature $\beta = \frac{1}{T}$ and the error probability p . This relation can be rewritten as

$$-2\beta J = \ln \frac{p}{1-p}, \quad (3.19)$$

which is known as the Nishimori line [54], which is showcased in Figure 3.7.

With this mapping it is possible to determine the maximal allowed error rate intrinsic to quantum hardware from the phase diagram of the statistical physics model. For any value of $p < p_c$ error recovery will be possible, since in the limit of an infinite system $L \rightarrow \infty$ it will be possible with probability $P = 1$ to determine the correct error homology class, which caused the error syndrome, measured by the check operators. From the numerical study of Honecker et al. [53] $p_c = 0.1094(2)$ was known for the random-bond Ising model (IM), which results in an optimal error threshold for the 2D Toric code with perfect measurements of 10,94(2)%. For imperfect measurements of the error syndrome, the p_c must be lower than $p_c = 0.1094(2)$, and Dennis et al. [25] were able to derive a lower bound $p_c \leq 0.0114$. Via the study of the corresponding 3D Random-Plaquette \mathbb{Z}_2 Gauge model Ohno et al. [62] were able to determine $p_c = 0.033$, so an minimal error threshold of 3.3% for the Toric code with imperfect measurements. There are other code schemes, based on the encoding of quantum information into topological properties of the system, as the topological color codes introduced in Bombin et al. [26, 63], and their respective error channels were studied in detail as well [60, 61, 64] with a 3D minimum error threshold of 1.9%. In the next section we will discuss a fracton model called the X-Cube model, which encodes the quantum information into a novel gapped quantum phase of matter, which hosts intrinsically immobile excitations that are called fractons, which are beyond the typical notion of topology.

3.6 X-Cube model

Vijay et al. [65] introduced the X-cube model as a paradigmatic model for fractons with the Hamiltonian

$$H_{X\text{-cube}} = - \sum_{c \in \mathcal{L}} A_c - \sum_{v \in \mathcal{L}} (B_v^x + B_v^y + B_v^z) \quad (3.20)$$

summed over all stabilizers A_c, B_v^μ , defined for cubes c and vertices v in a 3D cubic lattice \mathcal{L} . In analogy to the Toric code, discussed in Section 3.4, and other topological codes one qubit is assigned to each link of the cubic lattice, and the stabilizers are defined as tensor products of Pauli \hat{X}, \hat{Z} operators, acting on the adjacent links as

$$A_c = \prod_{l \in c} \hat{X}_l, B_v^\mu = \prod_{l \in v; l \perp \mu} \hat{Z}_l, \quad (3.21)$$

where one vertex operator B_v^μ acts on the four links perpendicular to the direction $\mu = \{x, y, z\}$ at vertex v , and A_c acts on the 12 edges surrounding the cube c .

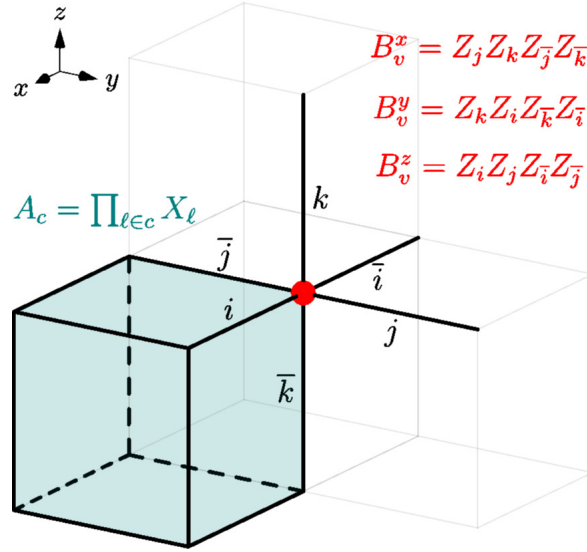


Figure 3.10: Stabilizers of the X-cube model on a cubic lattice: The stabilizers A_c, B_v^μ for $\mu = \{x, y, z\}$ are showcased. For each cube A_c is the product of \hat{X}_l operators acting on the 12 respective edges. For each vertex there are 3 stabilizers B_v^μ defined corresponding to the lattice directions $\mu = \{x, y, z\}$.

Since the A_c and B_v^μ are solely consisting of products of \hat{X} or \hat{Z} , they are commuting among each other reminiscent of the situation with X_v and Z_p in Equation 3.8 and Equation 3.9. Thus the code states are characterized by the results

of the action $A_c = 1$ and $B_v^\mu = 1$ on the states. In a cubic lattice with linear size L there are 2^{6L-3} degenerate ground states [66], which allow for an encoding of $6L - 3$ qubits. Those code states can not be distinguished by the measurement of the local stabilizers, but deviations from code states can be detected by the measurement results, and interpreted as excitations of the X-cube model. There are two types of gapped topological elementary excitations in Equation 3.20. The measurement of $A_c = -1$ corresponds to an intrinsically immobile fracton, represented by a solid grey dot, centered at a cube c in Figure 3.11. Excitations measured by $B_v^\mu = 1$ and $B_v^{\nu \neq \mu} = -1$ correspond to a lineon, which is mobile along the μ -direction, but immobile along the two perpendicular axes, and is thus represented by an ellipsoid in Figure 3.11 elongated along the respective μ - direction.

The location of the ensemble of topological excitations can be used to detect errors in the physical qubits. A single phase-flip error l corresponding to \hat{Z}_l would cause the four adjacent cubes to measure $A_c = -1$, and thus corresponds to four fractons adjacent to l , as displayed in Figure 3.11(a). An isolated single bit-flip error, occurring at a qubit residing on a link, e.g. elongated along the y -direction, will create two lineons at the two adjacent vertices v , resulting in $B_v^y = 1$, $B_v^x = -1$ and $B_v^z = -1$ at both of them.

Error correction is conducted by the application of operators

$$X_S = \prod_{l \in S} \hat{X}_l, Z_{\mathcal{M}} = \prod_{l \in \mathcal{M}} \hat{Z}_l \quad (3.22)$$

which correspond to a tensor product of Pauli operators acting along a string S for bit-flip errors and on links percolating the membrane as showcased in Figure 3.11(b) and (c) respectively. With the identical assumptions used for the derivation of the random bond Ising model in Section 3.5, namely perfect syndrome measurements and independent occurrence of errors, with both bit-flip and phase-flip error appearing at the rate p , it is possible to deduce an Ising spin system with quenched disorder for \hat{X} and \hat{Z} error channels. The error channels can be corrected independent of each other since the X-cube model is a CSS code just as the Toric code [48, 51].

It is useful to introduce the \mathbb{Z}_2 -valued 1-chains $n_A(l)$ for phase-flip and $n_B(l)$ for bit-flip errors where the values zero and one are again assigned to every link with one corresponding to a faulty qubit and zero to an unperturbed qubit. It is then possible to define boundary maps ∂_A and ∂_B in analogy of the boundary operator for the Toric model. The operator ∂_A^\dagger maps an error chain $n_A(l)$ found in the physical qubits \mathcal{Q} to the set of fractons characterizing the error. ∂_B^\dagger similarly maps $n_B(l)$ to the

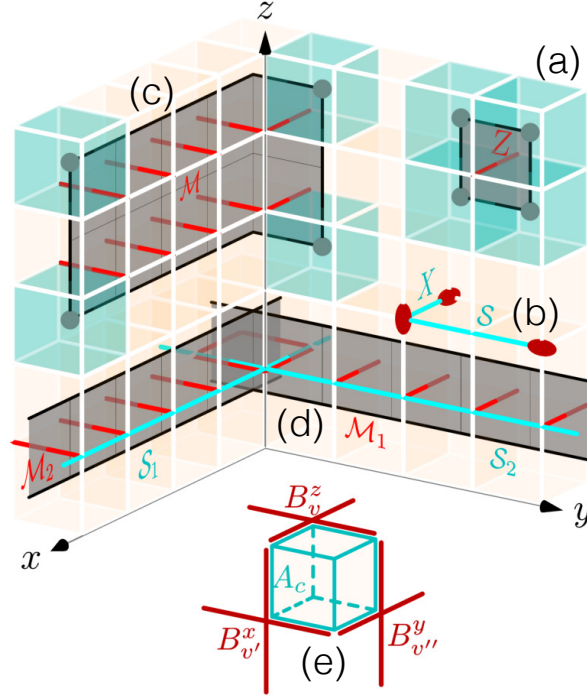


Figure 3.11: (a) **Isolated phase-flip error:** An individual \hat{Z} operator, applied on a link (red), causes the four adjacent stabilizers A_c to return eigenvalues $\lambda = -1$, which is identified by four fractons, each represented by a cyan cube. (b) **Bit-flip errors:** A single isolated \hat{X} error, present at a link (cyan) in y -direction, would create lineons on both adjacent vertices with $B_v^y = 1$, $B_v^\sigma = -1$ with $\sigma = \{x, z\}$. Reminiscent of error chains in the Toric code, adjacent bit-flip errors along a single spatial dimension only cause lineons at both ends of the error string \mathcal{S} . However, if two faulty qubits, along perpendicular directions are connected at a single vertex, e.g. along x - and y -direction, they create a lineon elongated along the z -direction at the connectional vertex. (c) **Membranes:** Phase-flip errors appearing on neighboring links only create fractons on the four cubes surrounding the membrane \mathcal{M} , extending perpendicular through the set of faulty qubits. (d) **Extended strings and membranes:** The strings \mathcal{S}_1 , \mathcal{S}_2 and the membranes \mathcal{M}_1 and \mathcal{M}_2 extend over the entire system across the boundary, thus represent errors, which do not cause the creation of excitations. These errors are not detectable. (e) **Stabilizer generators:** A_c and B_v^μ stabilizers are defined as in Equation 3.21 for each vertex and cube in the cubic lattice.

corresponding lineons. The mapping can be summarized as

$$\mathbb{Z}_2^A \xrightarrow[\partial_A^\dagger]{\partial_A} \mathbb{Z}_2^Q \xrightarrow[\partial_B]{\partial_B^\dagger} \mathbb{Z}_2^B. \quad (3.23)$$

Here \mathbb{Z}_2^A , \mathbb{Z}_2^Q and \mathbb{Z}_2^B denote the $\mathbb{Z}_2 = \{0, 1\}$ vector spaces for labeling configurations

of type- A stabilizer generators (\mathcal{A}), physical qubits (\mathcal{Q}), and type- B stabilizer generators (\mathcal{B}), respectively.

The resulting set of fractons (or lineons) are the measurable ambiguous error syndrome, which is compatible with multiple error configurations $n_A(l)$. If two error configurations $n_{A,1}(l)$ and $n_{A,2}(l)$ only differ by the application of the stabilizers defined in Equation 3.21 their action on the encoded information is equivalent and we can assign them to an equivalence class. Reliable assignment of error syndromes to the correct equivalence class $[n]_X = n + \text{Im } \partial_A$ of error configurations, which caused the syndrome is therefore crucial. Here $\text{Im } \partial$ denotes the image of the boundary map. To this end we map the error configurations $n_A(l)$ and $n_B(l)$ to a model of classical spins with the same method as presented in Section 3.5.

The probability that the physical qubit system is affected by the exemplary error chain $n_A(l)$ in analogy of Equation 3.11 is

$$P(n_A(l)) = \prod_l (1-p)^{1-n_A(l)} p^{n_A(l)} \propto \left(\frac{p}{1-p} \right)^{\sum_l n_A(l)}. \quad (3.24)$$

For the mapping we introduce classical Ising spins $S_i = \{-1, 1\}$, located at the centers of the cubes as displayed in Figure 3.12, and result in the 3D RPI model with Hamiltonian

$$H_{\tau_P}^A(S_i) = - \sum_P \tau_P \prod_{i \in P} S_i, \quad (3.25)$$

where the sum is running over all plaquettes P , consisting of four spins S_i on the edges of the plaquette in the 3D dual lattice \mathcal{L}^* . Each plaquette is contributing positively or negatively, depending on the value of $\tau_P = \{-1, +1\}$ and the spin orientations. When the signs of the interaction strengths $\tau_P = 1$ occur with probability $1-p$, and $\tau_P = -1$ with p , then the partition function of the system resembles the probability of the equivalence class

$$P([n]_X) \propto \sum_{\{A_c, n\}} e^{-\beta H_n^A} \propto Z_n^A = \sum_{\{S_i, \tau_P\}} e^{-\beta H_{\tau_P}^A(S_i)}. \quad (3.26)$$

A faulty physical qubit piercing a gray membrane in Figure 3.11 is hereby mapped to a plaquette, which contributes negatively with $\tau_P = -1$, and $\tau_P = 1$ for all other plaquettes corresponding to unaffected qubits. Thus for a given error chain we can identify $\tau_P = (-1)^{n(l)}$. The value of an Ising spin, located in a cube, can directly be associated to the eigenvalue, measured at the stabilizer generator A_c . The mapping is completely characterized with the definition of the Nishimori line analogous to Equation 3.19

$$e^{-\frac{2}{T}} = \frac{p}{1-p} \quad (3.27)$$

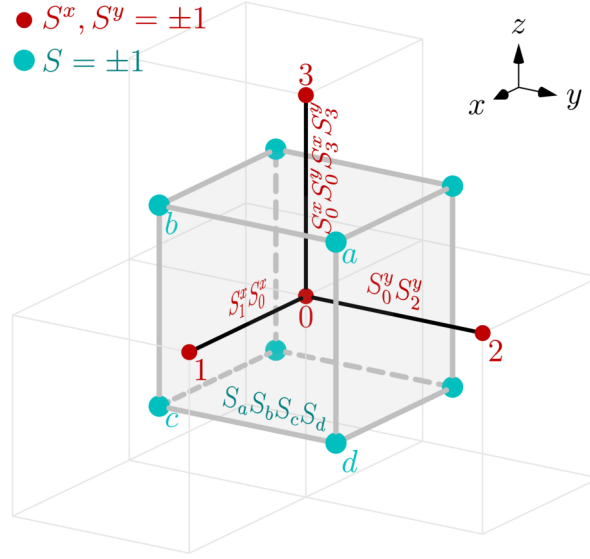


Figure 3.12: The spin arrangement for both models is shown. RPI: The measurement outcome of each $A_c = \{-1, 1\}$ is mapped to a respective Ising spin (cyan dot) $S_i = \{-1, 1\}$ at the center of a cube. If a physical qubit on a link, e.g. the link between zero and one, is affected by a respective error in the X-cube model, the coupling constant of the respective pierced plaquette a, c, b, d is $\tau_P = -1$. RACAT: Respectively the measurement outcomes of $B_v^\nu = \{-1, 1\}$ are mapped to $S_v^\nu = \{-1, 1\}$ for $\nu = \{x, y\}$ (red dot). The constraint $B_v^x B_v^y B_v^z = 1$ defines the spins in z -direction as $S_v^z = S_v^x S_v^y$. A respective error on any link, e.g. the link between zero and one, corresponds to a coupling constant $\tau_v^\mu = -1$. All coupling constants, which are not chosen negatively due to respective phase- and bit-flip errors, are positive.

Let us now consider phase-flip errors. Analogously to Equation 3.26 we can map the probability of error equivalence classes, consisting of the error syndromes of the B_v^μ stabilizers

$$P([n]_Z) \propto \sum_{\{B_v^\mu, n\}} e^{-\beta H_n^B} \propto Z_n^B = \sum_{\{S_i^x, S_i^y, \tau^\mu\}} e^{-\beta H_{\tau^\mu}^B(S_i^x, S_i^y)}, \quad (3.28)$$

to the partition function of the Hamiltonian $H_{\tau^\mu}^B(S_i^x, S_i^y)$, corresponding to the 3D RACAT model with quenched disorder. The spin model consists of two species of spins, residing at each vertex of the lattice \mathcal{L} . S_i^x is resembling the value of B_v^x and S_i^y corresponds to B_v^y respectively as displayed in Figure 3.12. The stabilizers in z -direction are not completely independent, since they are subject to the constraint $B_v^x B_v^y B_v^z = 1$ at each vertex, and so we can think of the spin in z -direction as the product of the spins along the other spatial dimensions $S_i^z = S_i^x S_i^y$. The signs of the interactions between next neighbour spins in all spatial dimensions can be derived from the error chain corresponding to phase-flip errors as $\tau_v^\mu = (-1)^{n(l)}$. Thus the

Chapter 3 Quantum error correction

Hamiltonian can be written as

$$H_{\tau^\mu}^B(S_i^x, S_i^y) = - \sum_v \sum_{\mu=x,y,z} \tau_v^\mu S_v^\mu S_{v+\hat{\mu}}^\mu, \quad (3.29)$$

with $\hat{\mu}$ being a unit vector in μ -direction and thus characterizing next neighbour interactions.

With our study of the phase diagrams of the RPI and RACAT model, which both have an ordered and a disordered phase, we can thus determine the optimal error thresholds for bit-flip p_c^X and phase-flip p_c^Z errors. As final remark for this chapter note that for $p = 0$ the two models are exactly dual to each other as discussed in Appendix B. Furthermore for the disorder free case our RPI model can be reduced to the Plaquette Ising model (PIM) [67], and the RACAT model to the Ashkin-Teller model (ATM) [68]. The scaling properties, symmetries and transition temperatures of these disorder free models have been studied in a series of papers [69–73], and we discuss the details in Chapter 5.

Chapter 4

Classical Monte Carlo

The purpose of this chapter is to introduce the Monte Carlo (MC) method [74] in the context of classical statistical physics [75]. Here we will restrict the discussion on the classical MC method, and introduce quantum Monte Carlo (QMC) techniques in Chapter 7. Although the theoretical framework describing classical statistical systems is well understood, analytical methods typically rely on approximations to describe interacting systems in certain limiting cases. Understanding critical phenomena therefore requires to affirm theoretical predictions by means of exact numerical methods. As the X-cube model, which is discussed in Section 3.5, can be mapped to spin models, we will introduce some important concepts of statistical mechanics in Section 4.1 on the basis of the archetypical spin model, the Ising model, which is briefly introduced with its characteristic observables. We continue with the characteristics, and scaling properties of first- and second-order phase transitions. In Section 4.2 the fundamental concepts underlying the MC method are explained, and two local update schemes are discussed in more detail for the Ising model in Section 4.3. Since single spin updates are infamous for long thermalization times close to phase transitions, a generalized ensemble method, known as parallel tempering, is introduced in Section 4.4.

4.1 Classical statistical physics

To be more precise in our discussion let us consider the Ising model for our recap of the general concepts used in our study of the models discussed in Section 3.5. The Ising model describes a set of spins σ_i , whose values can be $\sigma_i = \pm 1$, with fixed positions i on a d-dimension cubic lattice. The Hamiltonian \mathcal{H} can be written as

$$\mathcal{H} = -J \sum_{\langle i,j \rangle} \sigma_i \sigma_j - h \sum_i \sigma_i, \quad (4.1)$$

where $\langle i, j \rangle$ denotes a summation only over next neighbour sites, h is the external magnetic field, and J is the coupling constant, which can be either positive ($J > 0$) in the case of a ferromagnet, or negative ($J < 0$) for an anti-ferromagnet. The temperature driven transition, which can be observed in this model from a low temperature ordered phase to a high temperature disordered phase, occurs at a transition temperature T_c , and is known to be of second order. In two dimensions (2D) this model was even solved exactly, when no external field is present ($h = 0$) by Onsager [52]. In three dimensions (3D) there is no exact analytical solution available to date, but the system was studied extensively analytically and numerically throughout the years. For a more detailed discussion see [76, 77].

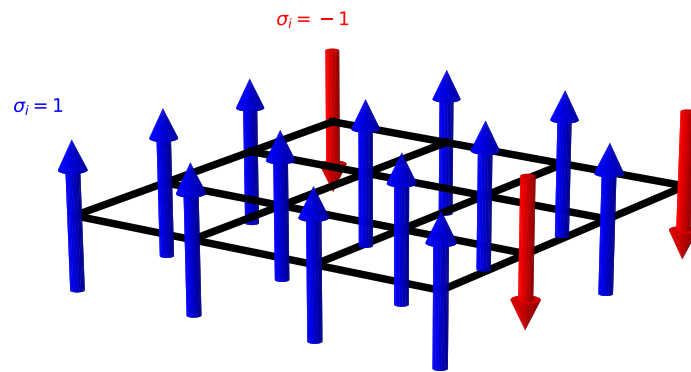


Figure 4.1: Spin configuration for the Ising model on a two dimensional lattice with linear system size $L = 4$. Individual spins are represented by blue ($\sigma_i = +1$) or red ($\sigma_i = -1$) arrows pointing up- or downwards respectively.

4.1.1 Standard observables and the partition sum

Thermodynamics characterizes systems by a set of time independent observables, for example (S, V, M) . It deals thereby with systems in equilibrium, which means all natural processes, initialized by any external influence, have ended, and the observables are measured only after such an equilibration phase. Depending on the

4.1 Classical statistical physics

choice of characterizing variables a thermodynamic potential is used to describe the state of the system. In the above example of (S, V, M) , where S is the entropy, V the volume and M the number of molecules of the system, this is the internal energy U . Its differential can be written as

$$dU = TdS - PdV + \mu dM, \quad (4.2)$$

where T is the temperature, P the pressure and μ the chemical potential [78]. Other combinations of observables are equivalently possible, and the sets (S, P, M) , (T, V, M) and (T, P, M) are corresponding to the thermodynamic potentials enthalpy H , the Gibbs free energy G and the Helmholtz free energy A . Their differentials can be written down as

$$dH = TdS + VdP + \mu dM \quad (4.3)$$

$$dG = -SdT + VdP + \mu dM \quad (4.4)$$

$$dA = -SdT - PdV + \mu dM. \quad (4.5)$$

For the later classification of phase transitions it is important to note that the above used observables (S, T, V, P) can be expressed as first derivatives of the respective thermodynamic potentials. For example by taking partial derivatives of Equation 4.2 and Equation 4.4 we note [79]

$$T = \left(\frac{\partial U}{\partial S} \right)_{M,V}, P = - \left(\frac{\partial U}{\partial V} \right)_{M,S}, S = - \left(\frac{\partial G}{\partial T} \right)_{M,P}, V = \left(\frac{\partial G}{\partial P} \right)_{M,T}. \quad (4.6)$$

In this thesis we will focus on the canonical ensemble when considering classical systems, so the particle number is fixed, and no particles can be added or removed from the system. In the canonical ensemble the partition function of a system is given by

$$Z = \sum_s e^{-\beta E} = \sum_s e^{-\frac{E}{k_B T}} \quad (4.7)$$

with the inverse temperature $\beta = 1/k_B T$ and the sum running over all possible spin configurations of the system. From now on let us set $k_B = 1$ to simplify the notation. Starting with a Hamiltonian, and noting that in this notation the internal energy is defined as $U = \langle \mathcal{H} \rangle = \langle E \rangle$, Equation 4.7 requires the microscopic description of the Hamiltonian \mathcal{H} , which in the case of the Ising model is given in Equation 4.1. It is then possible to define thermal expectation values denoted by $\langle \dots \rangle$ for a any observable O by

$$\langle O \rangle = \frac{1}{Z} \sum_s O(s) e^{-\frac{E(s)}{T}}. \quad (4.8)$$

When considering spin systems like the Ising model the most common observable is the magnetization m . It characterizes to which extent the spins are aligned with each other, and is capable of serving as an order parameter for the disorder-order phase transition in the sense of Landau. The magnetization can be calculated from the values of the individual spins σ_i as [75]

$$m = \frac{1}{V} \sum_i \sigma_i, \quad (4.9)$$

where $V = L^d$ is the volume, with L the linear system size and d the dimension of the system. For an infinite ($L \rightarrow \infty$) ferromagnetic system the magnetization in the ground state for ($T \rightarrow 0$) is $m = 1$ in the ordered phase, and $m = 0$ in the disordered phase. The specific heat capacity c_V indicates the amount of energy needed to change the temperature of the system by $1K$. It is defined as

$$c_V \equiv \frac{1}{V} \left(\frac{\partial U}{\partial T} \right)_V = -\frac{T}{V} \frac{\partial^2 A}{\partial T^2}. \quad (4.10)$$

Note that c_V can be expressed as second derivative of a thermodynamic potential. By using Equation 4.8 for the internal energy we can write down the above definition as

$$c_V \equiv \frac{1}{V} \left(\frac{\partial U}{\partial T} \right)_V = \frac{1}{V} \frac{\partial}{\partial T} \left(\frac{1}{Z(T)} \sum_s E e^{-\frac{E}{T}} \right) = \frac{1}{V} \frac{\partial}{\partial T} (g(T)h(T)), \quad (4.11)$$

where we define $g(T) = \frac{1}{Z(T)}$ and $h(T) = \sum_s E e^{-\frac{E}{T}}$. Their derivatives are $\frac{\partial}{\partial T} g(T) = -\frac{1}{Z(T)} \frac{1}{T^2} \langle E \rangle$ and $\frac{\partial}{\partial T} h(T) = \frac{1}{T^2} \sum_s E^2 e^{-\frac{E}{T}}$. By applying the product rule one obtains as a result:

$$c_V = \frac{1}{V} \frac{1}{T^2} (\langle E^2 \rangle - \langle E \rangle^2). \quad (4.12)$$

The representation in Equation 4.12 is useful for our numerical calculations, as $\langle E \rangle$ and $\langle E^2 \rangle$ can directly be calculated from the microscopic spin configuration. Another important quantity for magnetic systems is the susceptibility χ , which after a similar derivation can be expressed as [75]

$$\chi = \frac{V}{T} (\langle m^2 \rangle - \langle m \rangle^2). \quad (4.13)$$

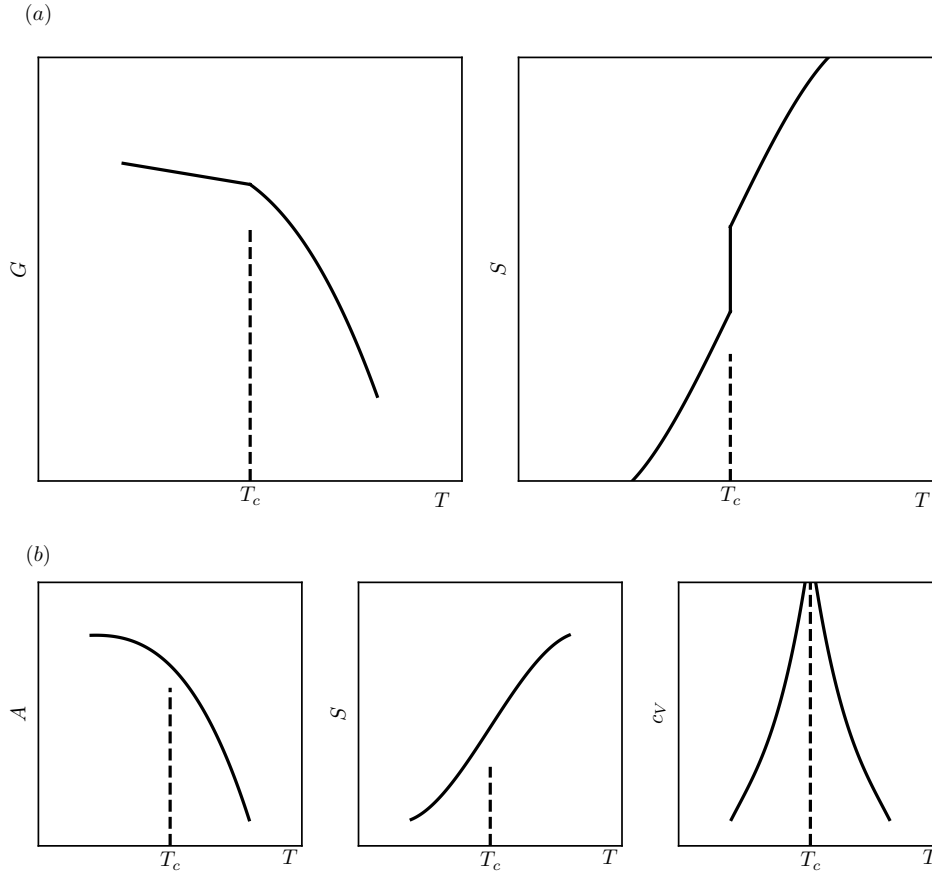


Figure 4.2: (a) **First order phase transition:** All thermodynamic potentials from Equation 4.2–Equation 4.5 are continuous at T_C , but the observables defined in Equation 4.6 display a jump associated with a latent heat. (b) **Second order phase transition:** Besides the thermodynamic potentials also the first derivatives are continuous, but some of the second derivatives, e.g. c_V in the Ising model, are discontinuous. [79]

Let us now consider two distinct behaviours of the above mentioned thermodynamic potentials and observables. There have been analytical criteria to describe the finite size effects occurring in numerical simulations [80]. But before we discuss, how it is eventually possible to distinguish first and second order phase transitions numerically based on finite systems, let us first explain what is meant by first and second order. This classification problem already dates back to 1933 when Ehrenfest [81], classified phase transition phenomena as first order transition, if the first derivative of a thermodynamic potential, e.g. S according to Equation 4.6, exhibits a jump as shown in Figure 4.2(a). This jump in the entropy is associated with a latent heat, which is

absorbed or emitted during the transition from one phase to the other. A second order phase transition on the other hand is continuous in the first derivative, but displays a discontinuity in some of the second derivatives of the thermodynamic potentials. This behaviour is schematically shown in Figure 4.2(b). As there is no jump in the first derivative, there is no latent heat involved in a second order phase transition. The transition of water to ice would be an example of such a first order phase transition. The Ising model exhibits a second order phase transition. In 1937 Landau noted [82], that both of the above types of phase transitions can be accompanied by a change in the systems symmetry, which can be characterized by an order parameter, e.g. the magnetization m in the case of the Ising model. The order parameter is zero in the disordered phase, which is the most symmetric phase, and finite in the ordered phase. A symmetry of the ordered phase is broken in the disordered phase. Thus the symmetry group of the disordered phase is a subgroup of the symmetry group of the ordered phase.

4.2 Markov chain Monte Carlo

As mentioned in the beginning of this chapter Monte Carlo methods allow for the efficient evaluation of high-dimensional integrals. As an example let us consider the rather general form of an integral over a function f

$$I = \int_D f(\vec{x}) d\vec{x}, \quad (4.14)$$

where D is the domain of integration and \vec{x} is a vector in the eventually high-dimensional vector space of the domain. If it was somehow possible to get a set of N independent and randomly distributed points $(\vec{x}_1, \dots, \vec{x}_N) \in D$, we could estimate the value of the integral I by

$$\hat{I}_N = \frac{1}{N} \sum_{i=1}^N f(\vec{x}_i), \quad (4.15)$$

That Equation 4.15 converges towards the exact value of I , is ensured by the law of large numbers, if each random variable has a common mean and finite variance σ^2 in the limit $N \rightarrow \infty$ [83]. How fast \hat{I}_N converges towards I , can then be estimated with the central limit theorem which states that the sum of many independent random variables will be approximately normally distributed, if each summand has a high probability of being small [84]

$$\sqrt{N} (\hat{I}_N - I) \xrightarrow{d} N(0, \sigma^2). \quad (4.16)$$

4.2 Markov chain Monte Carlo

Therefore the error can be estimated to be proportional to $\mathcal{O}(N^{-1/2})$. This implies, that the dimension of the integration domain has no influence on the convergence rate. Even though in one dimension other integration methods like the Riemann approximation, which approximates the integral by taking a equidistant grid of N data points along D , might provide a better error scaling proportional to $\mathcal{O}(N^{-1})$, they suffer from the curse of dimensionality. This implies that these deterministic methods have a dramatic lack of effectiveness, if the dimension of D is increased. While in a d -dimensional integration the Riemann approximation needs N^d evaluation points in the grid to achieve a comparable approximation as in the one dimensional case, the necessary number of random samples for the Monte Carlo method stays constant at N . The fact that the error estimate is scaling independent of the dimensionality is one of the main reasons for the prominence of MC methods in physics. However, the scalar factor preceding $\mathcal{O}(N^{-1/2})$ might be very large, and in general it is a challenging task to generate independent configurations from D according to a certain distribution in the first place.

Note that in the case of discrete lattice systems like the Ising model we need to evaluate sums instead of integrals. Recalling that we want to calculate physical observables according to Equation 4.8, we can rewrite $W(s) = e^{-\beta E(s)}$, where $E(s)$ is the energy of the spin configuration s , as the weight of the configuration. With the definition of $w(s) = \frac{W(s)}{Z}$ as a probability density we can express Equation 4.8 as

$$\langle O \rangle = \sum_s O(s)w(s), \quad (4.17)$$

and look at it as an average of the observable O over the states s with the physically determined probability density $w(s)$. Evaluating Equation 4.17 with MC requires to create samples $\{s_i\}$ according to $w(s)$, and estimate the value of $\langle O \rangle$ by

$$\langle O \rangle_{MC} = \frac{1}{N} \sum_{i=1}^N O(s_i). \quad (4.18)$$

In order to generate the configurations s_i according to the respective probability density, we can use a Markov chain. Such a chain consists of N elements s_1, s_2, \dots, s_N where the current configuration s_i has no information about its predecessors except for the previous configuration s_{i-1} . It is therefore possible to define a transition function $T(s_a \rightarrow s_b)$ which defines the probability that configuration s_b follows on s_a for any two configurations in the space of allowed configurations, which only depends on these two configurations. To preserve conservation of total probability it has to satisfy $\sum_{s_b} T(s_a \rightarrow s_b) = 1$. Furthermore it

can be shown that the Markov chain converges as described above towards the proper weight, if two conditions below are met [84, 85].

Ergodicity

Any configuration s_b can be reached from any configuration s_a in a finite number of transition steps.

Balance

The transition matrix has to fulfill the balance equation.

$$\sum_{s_b} W(s_a) T(s_a \rightarrow s_b) = W(s_b) \quad (4.19)$$

In practice it might be easier to use the stronger detailed balance condition

$$W(s_a) T(s_a \rightarrow s_b) = W(s_b) T(s_b \rightarrow s_a), \quad (4.20)$$

which implies balance, but allows to construct the transition matrix in a convenient way, as we will see in the next section

4.3 Local updates

The requirements that were imposed on a reasonable Markov chain in the previous section can be satisfied by a broad variety of specific update schemes. In classical physics when considering lattice systems the most prominent ones are local updates and cluster updates. Cluster updates, like the Swendsen-Wang algorithm [86] or the Wolff-algorithm [87], as their name suggests, change the spin of a whole set of spins in the system, and display an improved performance close to the transition temperature T_c , when correlations in the system are important. Local updates on the other side are universally applicable to lattice systems, and might even outperform cluster algorithms far away from T_c due to a smaller computational overhead.

4.3.1 Metropolis algorithm

A general solution to define the transition matrices for the Markov chain was first introduced by Metropolis et al. [74, 85], and later generalized for arbitrary weights by Hastings [88]. Detailed balance as introduced in Equation 4.20, implies that on average each update, involved in the Markov process, is equilibrated by its reverse update. The transition matrix $T(s_{old} \rightarrow s_{new})$ is decomposed into two parts

$$T(s_{old} \rightarrow s_{new}) = P(s_{old} \rightarrow s_{new}) \min(1, q). \quad (4.21)$$

4.3 Local updates

Here $P(s_{old} \rightarrow s_{new})$ is the probability that the update, which transforms s_{old} to s_{new} , is proposed and q is the acceptance factor for this update. The transition matrix for the reverse update can then formally be written as

$$T(s_{new} \rightarrow s_{old}) = P(s_{new} \rightarrow s_{old}) \min\left(1, \frac{1}{q}\right). \quad (4.22)$$

The acceptance factor is then chosen accordingly to satisfy the detailed balance Equation 4.20

$$q = \frac{W(s_{new}) P(s_{new} \rightarrow s_{old})}{W(s_{old}) P(s_{old} \rightarrow s_{new})}. \quad (4.23)$$

In the case of a d -dimensional Ising model the proposal function could be to choose one spin σ_i at random, and propose to change the sign of this spin to the opposite value. The probability of choosing this update would therefore be $P(s_{old} \rightarrow s_{new}) = 1/L^d$, as there are L^d spins in the system. The reverse update is chosen equally likely with $P(s_{new} \rightarrow s_{old}) = 1/L^d$. The weights of the two configurations are given by $W(s_{old}) = e^{-\beta E(s_{old})}$ and $W(s_{new}) = e^{-\beta E(s_{new})}$ respectively. The acceptance factor then follows from Equation 4.23 as

$$q = \frac{e^{-\beta E(s_{new})}}{e^{-\beta E(s_{old})}} = e^{-\beta \Delta E}, \quad (4.24)$$

with $\Delta E = E(s_{new}) - E(s_{old})$. If $E(s_{new}) < E(s_{old})$, the proposed update is always accepted. Otherwise a random number r is drawn uniformly from the interval $[0, 1)$ and if $r \geq q$, the update is accepted. If $r < q$, the update is rejected, and the old configuration is considered to be the new configuration in the Markov chain. The reason this can be done efficiently is that $E(s_{new})$ and $E(s_{old})$ only differ by the terms containing σ_i , and all the other contributions to the Hamiltonian can be ignored. Ergodicity is obviously fulfilled, as all spins are possibly subject to change.

4.3.2 Heat-bath algorithm

An alternative to the update probabilities in the Metropolis algorithm are given in the heat-bath algorithm, which chooses the new value of $\sigma_{i,new}$ directly according to the Boltzmann weight [89]. The implementation of the algorithm is model dependent, and in the form it is presented here it is only applicable to lattice systems and discrete degrees of freedom with a finite set of allowed values for σ . For the Ising model the spins σ can only take the two values ± 1 , but to showcase the more general applicability let us for now allow the values $\sigma = \{1, \dots, n\}$. The probability to select the spin σ_i can still be chosen randomly, and result in $P(s_{old} \rightarrow s_{new}) = 1/L^d$ and

$P(s_{new} \rightarrow s_{old}) = 1/L^d$. The update is always accepted, but the outcome is flexible in this scheme, and the probabilities depend only on the surrounding of $\sigma_{i,old}$, and how a change to $\sigma_{i,j}$ would affect the energy. For each possible value j in $\{1, \dots, n\}$ the probability to be the new value after the update is given by

$$T(s_{old} \rightarrow s_j) = \frac{e^{-\beta E(s_j)}}{\sum_{k=1}^n e^{-\beta E(s_k)}}, \quad (4.25)$$

with s_j being the configuration where $\sigma_{i,old}$ was changed to $\sigma_{i,old}$. This choice of the transition matrix trivially satisfies detailed balance as Equation 4.20 results in

$$e^{-\beta E(s_{old})} \frac{e^{-\beta E(s_j)}}{\sum_{k=1}^n e^{-\beta E(s_k)}} = e^{-\beta E(s_j)} \frac{e^{-\beta E(s_{old})}}{\sum_{k=1}^n e^{-\beta E(s_k)}}. \quad (4.26)$$

In this general form one would use cumulative probabilities $P_j = \sum_{l=0}^j T(s_{old} \rightarrow s_l)$ which by construction satisfy the condition $P_n = 1$. The random number $r \in [0, 1)$, as discussed in the previous section, would then iteratively be compared to the values of P_j until $r > P_{j_0}$. j_0 is the new value for σ_i after the update. In the case of Ising spins this update scheme is particularly simple, as the only two possible outcomes are ± 1 . Therefore only one comparison of r is needed to determine the new configuration after calculating the local Energies. We compared the performance of the Metropolis and heat-bath algorithm for our use cases, and choose the latter one due to shorter autocorrelation times.

4.4 Parallel tempering

To improve the performance when considering thermalization times as well as autocorrelation times, it proves to be useful in certain cases to use generalized ensemble methods. For quantum mechanical problems we discuss such a method in Section 7. In the classical case parallel tempering, also referenced to as replica exchange MC [75], uses such an extended ensemble. Instead of the canonical partition sum Z_i , as defined in Equation 4.7, the product of N_T partition sums at different temperatures $T_i \in T_1, \dots, T_{N_T}$ is considered

$$Z_{PT} = \prod_i^{N_T} Z_i = \prod_i^{N_T} \sum_s e^{-\beta_i E(s^{(i)})}. \quad (4.27)$$

For each of the N_T temperatures an individual Markov chain is generated in parallel by means of any of the above discussed update schemes according to their respective weights including β_i . The performance improvement is generated by an additional

4.4 Parallel tempering

update, which is proposed after a fixed number of local updates, and allows for an exchange of the complete current configuration $s^{(i)}$ at T_i with the configuration $s^{(j)}$ at one of the other temperatures T_j . The transition matrix can again be calculated as in Subsection 4.3.1, and reads as

$$T(s_i \rightarrow s_j) = \min\left(1, e^{(\beta_j - \beta_i)(E(s^{(j)}) - E(s^{(i)}))}\right). \quad (4.28)$$

As this update might get rejected, frequently when the difference in temperature is too big, we only allow for an exchange between adjacent temperatures, and imply an ordered structure in the temperatures $T_1 < \dots < T_j < \dots < T_{N_T}$. The general idea is, that the highest temperature is chosen in a way that autocorrelation times are short, and the system thermalizes quickly. The individual Markov chains are thereby enabled to escape local minima of the energy landscape. While the method is straightforward to implement, and does not require a priori knowledge about the Hamiltonian, the optimal allocation of the T_i s is a non-trivial task. There are feedback optimized methods, as proposed by Katzgraber et al. [90] which try to find the optimal T_i allocation for a certain Hamiltonian by measuring the diffusion of one simulation. Each simulation is labeled either by "down" or "up", depending on which temperature of T_0 (lowest temperature) or T_{N_T} (highest temperature) it visited most recently. For each temperature T_i a histogram is measured with n_{up} and n_{down} . From this data the fraction $f(T)$ referred to as "upness" of replicas, diffusing from high temperature at temperature T_i is determined as

$$f(T_i) = \frac{n_{up}(T_i)}{n_{up}(T_i) + n_{down}(T_i)}. \quad (4.29)$$

When plotting this fraction as function of the number i of the simulation, the allocation is said to be optimal, if a straight line is shown. In Figure 4.3(a) an almost optimal allocation is shown for the case of the RPI with $L = 6$ and $p = 0.075$. The red line, shown in the same figure, displays a sharp drop between two adjacent temperatures, indicating that the configurations before and after the jump are almost never exchanged. In the method proposed in [90] the temperatures are then iteratively changed to obtain a straight line for the fraction. However, when Hamiltonians with quenched disorder are studied, as in our numerical analysis of the RPI and RACAT, for every disorder realization the Hamiltonian and thereby the optimal allocation is different. Since the observables in those cases contain a disorder average over N_d quenched systems for the same set of temperatures, we use the criterion based on $f(T)$, but carefully choose a fixed temperature allocation for all Hamiltonians created

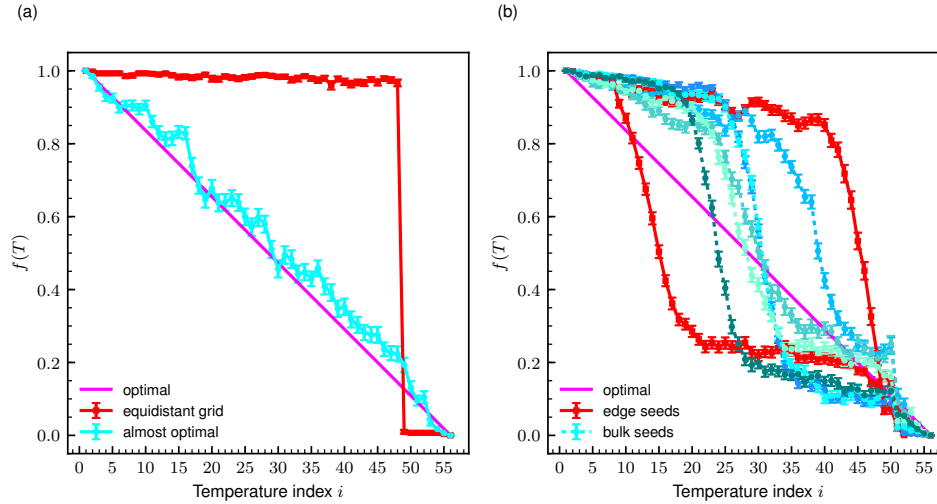


Figure 4.3: (a) **Upness as defined in Equation 4.29.** An allocation of temperatures between T_0 and T_{max} is optimal, if the resulting upness $f(T)$ is given by a straight line between $f(T_0) = 1$ and $f(T_{max}) = 0$ (purple line). This corresponds to an optimal diffusion of individual simulations in temperature space. The cyan full line corresponds to a typical production run with a carefully chosen temperature grid with linear system size $L = 6$ and error rate $p = 0.075$ for the 3D RPI model. The red line corresponds to an equidistant temperature spacing for the same system between T_0 and T_{max} . A discontinuous jump for the resulting upness is visible between $f(T_{48})$ and $f(T_{49})$. This jump implies that there is little communication between the two temperature regimes $T < T_{48}$ and T_{49} . Thus an optimal thermalization is not possible, as the parallel tempering updates between such two adjacent temperatures have very small acceptance ratios. (b) **Upness in larger systems.** Exemplary $L = 10$, $p = 0.075$ for the RPI is shown, a disorder average across different quenched systems is needed which requires one temperature allocation used for one (p, L) value set. As each quenched system contains a different set of interaction constants, subject to the disorder present in the system, it features a different energy landscape. However, the optimal temperature allocation of a system is strongly dependent on the energy landscape, and thus different quenched systems corresponding to the same values of p and L may result in strongly deviating optimal temperature allocations. Therefore we carefully select a temperature allocation, which results in an almost optimal upness for the majority of the N_d considered systems, which are exemplary showcased here in blue. As the *edge seeds*, which are shown in red, feature a non-optimal upness are rare but physical we also have to take them into account, and check for equilibration as discussed in Section A.

for a fixed p and L value. In this fashion we allow for a meaningful disorder average, and aim for an almost optimal temperature allocation for the bulk of the simulations.

Chapter 5

Numerical analysis of the optimal error thresholds

The stability of the topological fracton X-Cube code, introduced in Section 3.6, against local X and Z errors is related to the order-disorder PTs of the RPI and RACAT model, respectively. We conducted large scale MC simulations, using the parallel tempering method, discussed in Section 4.4, in combination with local heat-bath updates, as introduced in Section 4.3, and a special type of plane update, discussed in Appendix A, taking into account the symmetries of our models, which are highlighted in Section 5.1. In this chapter we describe in detail how these PTs and the optimal error thresholds p_c^X and p_c^Z are determined. First we summarize our findings regarding the disorder free cases of the RPI and RACAT models, which are known as PIM and ATM, and benchmark our method by reproducing the values of T_c^{PIM} and T_c^{ATM} in Section 5.1. We will then discuss, how the ordered phase persists for small but finite values of p , and carefully analyse the transition with increasing disorder in Section 5.2. We find, that the nature of the PT changes from being discontinuous at small values of p , to a continuous PT for p values, close to the threshold values p_c^X and p_c^Z . There we also address the question, how it is possible to examine the weakening effect of increasing disorder upon the discontinuity numerically. In Section 5.3 we determine the numerical values of p_c^X and p_c^Z by ruling out an order-disorder transition for $p > p_c$ in both models respectively. The parameters used for the simulations, which led to the results presented in this chapter, are summarized in Appendix A.

5.1 Models and symmetries

Let us now take a closer look at the 3D Ising spin models, derived in Section 3.6. For the sake of better readability we repeat the Hamiltonians formulated for the RPI

model in Equation 3.25

$$H_{\tau_P}^A(S_i) = - \sum_P \tau_P \prod_{i \in P} S_i, \quad (5.1)$$

with the sum running over all plaquettes P , each consisting of the product of the four surrounding Ising spins $S_i = \{-1, 1\}$. Respectively the RACAT model from Equation 3.29

$$H_{\tau^\mu}^B(S_i^x, S_i^y) = - \sum_v \sum_{\mu=x,y,z} \tau_v^\mu S_v^\mu S_{v+\hat{\mu}}^\mu \quad (5.2)$$

contains the sum over all vertices v , each adding 3 terms, consisting of nearest neighbour products along the directions μ respectively. Here the special relation $S_i^z = S_i^x S_i^y$ is imposed by the commutation relations of the B terms in the Hamiltonian of the X-cube model in Equation 3.20. The quenched disorder rate p enters via the coupling constants which obey

$$\tau_P = \begin{cases} -1 & \text{with probability } p, \\ 1 & \text{with probability } 1 - p, \end{cases} \quad (5.3)$$

$$\tau_v^\mu = \begin{cases} -1 & \text{with probability } p, \\ 1 & \text{with probability } 1 - p. \end{cases} \quad (5.4)$$

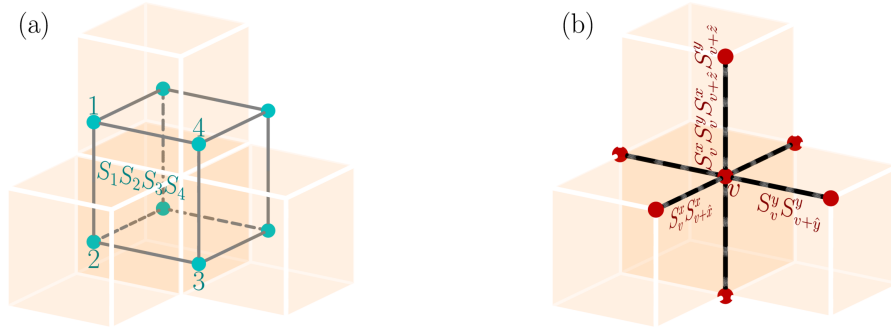


Figure 5.1: (a) **RPI model:** Ising spins are placed on a cubic lattice. Spin interactions take place among the four spins surrounding a plaquette as depicted for the plaquette containing S_1, S_2, S_3, S_4 . (b) **RACAT model:** Two Ising spins S_v^x, S_v^y reside on each vertex v . Anisotropic nearest neighbour interactions are present as visualized with spins in z-direction given by $S_v^z = S_v^x S_v^y$.

5.1.1 Disorder free models

In the special case in which there is absolutely no disorder in the system ($p = 0$), all coupling constants are ferromagnetic and the previously mentioned models in Equation 5.1 and Equation 5.2 can be narrowed down to the PIM with Hamiltonian

$$H_{\text{PIM}}(S_i) = - \sum_P \prod_{i \in P} S_i \quad (5.5)$$

and the ATM, whose Hamiltonian is defined as

$$H_{\text{ATM}}(S_i^x, S_i^y) = - \sum_v \sum_{\mu=x,y,z} S_v^\mu S_{v+\hat{\mu}}^\mu. \quad (5.6)$$

It is easy to realize, that a spin configuration with all spins S_i aligned is a ground state of the PIM, since all plaquettes will contribute a factor -1 , and the energy is minimized. A global rotation of all spins $S_i \rightarrow -S_i$ results in a second ground state, which is nothing special so far as this global symmetry is inherent to many Ising models, like the one discussed in Equation 4.1 in the absence of an external field ($h = 0$). However, the PIM showcases a more peculiar planar sub-system symmetry. One can flip all L^2 spins belonging to a 2D plane in the 3D lattice containing L^3 spins without changing the energy. This symmetry is not affected by the quenched disorder present in the RPI model, and thus results in a subextensive ground state degeneracy ($\sim 2^{3L}$) for both of these models [70, 73].

The ATM and the RACAT model both display a similar sub-system symmetry. The energy of both models is unaffected by a spin-flip of all S_v^x spins, contained in a particular x-z plane. It is also unchanged by a spin-flip of all S_v^y spins in a y-z plane, or a spin-flip of both S_v^x and S_v^y spins in a respective x-y plane. Thus the ground state is similarly degenerate [69].

5.1.2 Order parameters

The usual magnetization m , defined in Equation 4.9, which typically characterizes the ordered phase with $\langle m \rangle \neq 0$ and the disordered phase with $\langle m \rangle = 0$, is not invariant in our models, as it would not preserve the sub-system symmetry and therefore result in $\langle m \rangle = 0$ for both phases. For the PIM and the RPI model we thus define the order parameter, which is invariant under the above mentioned symmetries as

$$Q^A = \frac{1}{L^3} \sum_{z=0}^{L-1} \left[\left\langle \left| \sum_{x,y=0}^{L-1} S_{c(x,y,z)} S_{c(x,y,z+1)} \right| \right\rangle \right], \quad (5.7)$$

with $\langle \cdot \rangle$ and $[\cdot]$ denoting the thermal and disorder average. The disorder average hereby has to be thought of as an average over a finite number N_d of random quenches of the couplings, defined in Equation 5.3. In the disorder free case all quenched couplings are equal by definition. The outer sum in Equation 5.7 is running over all x-y planes, stacked in z-direction, and the inner sum involves a subextensive number ($\propto L^2$) of spins, contained in the two respective adjacent planes. The absolute value makes the order parameter explicitly respecting the planar sub-system symmetry [73]. Similarly we can construct an invariant order parameter for the ATM and the RACAT model as

$$Q^B = \frac{1}{L^3} \sum_{x,y=0}^{L-1} \left[\left\langle \left| \sum_{z=0}^{L-1} S_{v(x,y,z)}^z \right| \right\rangle \right], \quad (5.8)$$

which incorporates the respective spin-flip symmetries. Note that similar to Equation 5.7 and Equation 5.8 analogous formulations are possible with permutations of the spatial directions x, y, z .

Using the above Hamiltonians and order parameters the transition temperature of a first-order PT can be determined by the calculation of the respective histograms $P(E)$, estimating the energy distribution function, the specific heat capacity c_V , expressed by the energy, as well as the the susceptibility χ and the Binder cumulant B . which both are defined according to the model dependent respective order parameter,

$$P(E, \beta, L) = [\langle \delta(E - E') \rangle], \quad (5.9)$$

$$c_V(\beta, L) = \beta^2 \left([\langle E^2 \rangle] - [\langle E \rangle^2] \right), \quad (5.10)$$

$$\chi(\beta, L) = \beta L^3 \left([\langle Q^2 \rangle] - [\langle Q \rangle^2] \right), \quad (5.11)$$

$$B(\beta, L) = 1 - \frac{[\langle Q_n^4 \rangle]}{3 [\langle Q_n^2 \rangle]^2}. \quad (5.12)$$

Here $\beta = 1/T$ is the inverse temperature, and Q the respective model dependent order parameter. Note that the energy densities E in Equation 5.9 and Equation 5.10 are including a normalization factor $\langle E \rangle = \frac{\langle H \rangle}{E_{GS}}$ with $E_{GS}^{PIM} = E_{GS}^{ATM} = 3L^3$. The order parameters Q^A and Q^B are normalized for the calculation of the Binder cumulants as

$$Q_n^A = \frac{L}{L-1} \left(Q^A - \frac{1}{L} \right), Q_n^B = \frac{L}{L-\sqrt{L}} \left(Q^B - \frac{1}{\sqrt{L}} \right) \quad (5.13)$$

to obtain the standard high temperature ($Q_n \rightarrow 0$) and low temperature ($Q_n \rightarrow 1$) behaviour.

The second-moment correlation length

$$\xi_L(\beta, L) = \frac{1}{2 \sin(|\mathbf{k}_{\min}|/2)} \left(\frac{\tilde{G}(\mathbf{0})}{\tilde{G}(\mathbf{k}_{\min})} - 1 \right)^{1/2}, \quad (5.14)$$

which is defined in terms of $\tilde{G}(\mathbf{k}) = \sum_{\mathbf{r}} G(\mathbf{r}) e^{-i\mathbf{k}\cdot\mathbf{r}}$ is calculated. $\tilde{G}(\mathbf{k})$ is the Fourier transformation of the real space correlation function $G(\mathbf{r})$. The sum over \mathbf{r} is running over all sites of the lattice \mathcal{L} , and \mathbf{k}_{\min} denotes the minimal non-zero wavevector [75].

The spatial correlation functions, related to the order parameters Q^A and Q^B , are given by

$$G^A(\mathbf{r}) = \frac{1}{L^3} \sum_{c \in \mathcal{L}} \left[\langle S_c S_{c+\hat{z}} S_{c+(\mathbf{r},0)} S_{c+(\mathbf{r},\hat{z})} \rangle \right], \quad (5.15)$$

$$G^B(r) = \frac{1}{L^3} \sum_{v \in \mathcal{L}} \left[\langle S_v^z S_{v+r\hat{z}}^z \rangle \right]. \quad (5.16)$$

In the limit of far apart spins $|\mathbf{r}| \rightarrow \infty$ these correlation functions are designed to replicate the disorder averaged order parameter values as $G^{A(B)}(\mathbf{r}) \rightarrow [Q^{A(B)}]^2$, thus representing the respective mean magnitude of the order parameter.

5.1.3 Non-standard first-order scaling

In previous studies of the disorder free instances of the PIM and the ATM the PT between the ordered and the disordered phase was found to be discontinuous, i.e. of first-order as described in Section 4.1. However, in contrast to the standard first-order finite size scaling, where the finite-size correction of the transition temperature is in the order of L^{-d} [80, 91] and the transition temperature can be extrapolated as:

$$T_c(L) \sim T_c + bL^{-d}, \quad (5.17)$$

the subextensive degeneracy ($\sim 2^{3L}$), present in all our models, modifies the leading order correction to $L^{-(d-1)}$ [70, 73]. Since the subsystem symmetry persists in the disordered RPI and RACAT models, we assume that the leading finite size correction is still on the order of $L^{-(d-1)}$ for discontinuous PTs at finite p . Thus we can estimate T_c^O for an observable O by fitting the scaling relation

$$T_c^O(L) \sim T_c^O + b^O L^{-(d-1)}, \quad (5.18)$$

where T_c^O and b^O are free fitting parameters. The finite-size transition points $T_c^O(L)$, used in Equation 5.18, are obtained from the location of peaks in $\chi(\beta, L)$ and

$c_V(\beta, L)$, or the location of the dips in $B(\beta, L)$. For $P(E, \beta, L)$ the characteristic feature of a first-order PT is a double peak of equal weight, and the finite-size transition points $T_c^{P(E)}(L)$ are estimated by reweighting the energy density histograms of a temperature close to $T_c^{P(E)}(L)$, as explained in Section 5.1.4.

5.1.4 Numerical results in the disorder free case

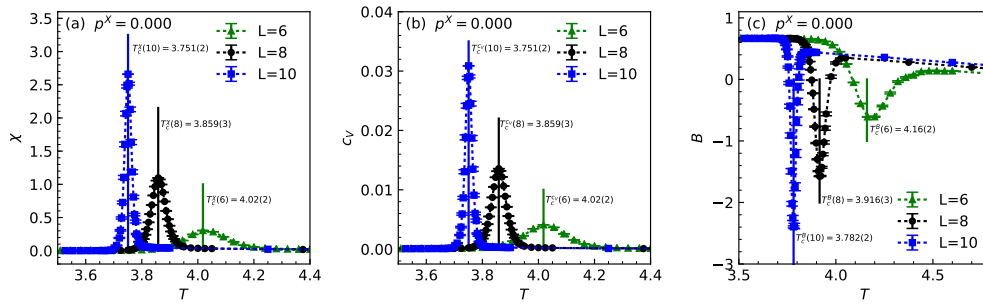


Figure 5.2: (a) Susceptibility, (b) Specific heat capacity and (c) Binder cumulant plotted as functions of the temperature T . Measurements belong to the PIM, thus representing the $p^X = 0$ case of the RPI. For χ and c_V peaks are growing sharper and diverge with increasing system sizes at the finite-size transition points. The corresponding B has a non-monotonic dependence on temperature with a dip developed at an effective transition point [80, 91]. Vertical lines visualize the locations of the respective peaks and dips, with the corresponding values of $T_c^O(L)$ displayed next to them.

Let us now move on to the concrete numerical results from our Monte Carlo method described in Chapter 4. In the subsequent pages we will not mention the detailed parameters of the simulations every single time for the sake of better readability, but refer to Table A.1 for the parameters of the simulations for the PIM and RPI model, and to Table A.2 for the respective parameter sets for the ATM and RACAT model.

We start with validating our method by benchmarking our results, obtained for the PIM and the resulting transition temperature of all measured observables T_c^O , with the value $T_c^{PIM} = 3.6273(5)$, found by a finite size study by Müller et al. [92] with linear system sizes up to $L = 26$. Figure 5.2 displays the temperature dependence of c_V , χ and B , as defined in Equation 5.10, Equation 5.11 and Equation 5.12. The characteristic sharpening and divergence of the peaks of χ and c_V with increasing

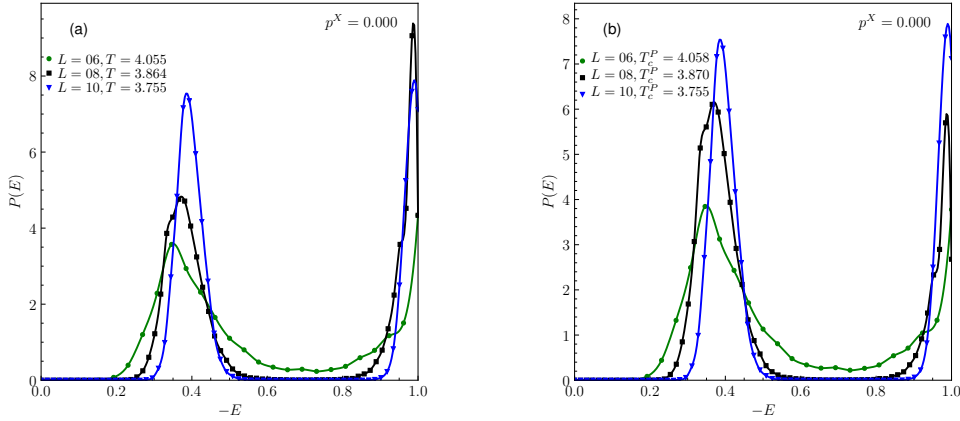


Figure 5.3: (a) **Directly measured energy density histogram:** $P(E)$ measured for the PIM with lattice sizes $L = 6, 8, 10$. Two peaks are clearly visible for each lattice size, but the height of the peaks for e.g. $L = 6$ or $L = 8$ deviates. The distance ΔE between the double peaks reflects the latent heat, associated with a first-order PT [80]. (b) **Reweighted energy density histograms:** By reweighting the original histograms by $e^{-(\beta_0 - \beta)E}$, until the two peaks reach equal height, we determine the respective $T_c^{P(E)}(L)$.

lattice size is a trend fully consistent with a discontinuous PT. The locations of the peaks and dips are used to extrapolate the transition temperature for $L \rightarrow \infty$.

When a PT is discontinuous as in the PIM, the energy density histogram $P(E, \beta, L)$ features a double-peak structure on large enough system sizes and at temperatures close to the transition [93]. In addition, these double peaks shall grow sharper and diverge with increasing system sizes similar to the peaks of c_V and χ . Since the parallel tempering MC technique is allocating the temperatures between T_{\min} and T_{\max} in a way to optimize the upness for the simulations, belonging to a given (p, L) set, as explained in Figure 4.3, a direct observation of the energy density histograms will typically not result in a double peak with equal height, as shown in Figure 5.3(a). The displayed histograms belong to temperatures, which are close to $T_c^{P(E)}(L)$, as they display two pronounced distinct peaks, one corresponding to the ordered, and the other to the disordered phase. To determine $T_c^{P(E)}(L)$ we use a histogram reweighting technique [75, 94]. The technique assumes that during the MC process an energy density histogram at a given temperature $T = \frac{1}{\beta}$ is measured as

$$P(E, \beta, L) \propto \Omega(E, L) e^{-\beta E}. \quad (5.19)$$

Thus it is possible to deduce the histogram at a close temperature $T_0 = \frac{1}{\beta_0}$ as

$$P(E, \beta_0, L) \propto \Omega(E, L) e^{-\beta_0 E} = \Omega(E, L) e^{-\beta E} e^{-(\beta_0 - \beta)E} \propto P(E, \beta, L) e^{-(\beta_0 - \beta)E}. \quad (5.20)$$

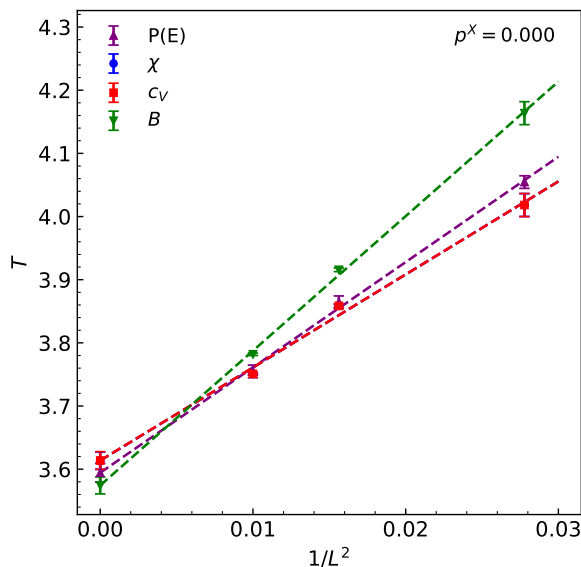


Figure 5.4: Finite size scaling of the relevant observables: The finite-size transition points $T_c^O(L)$ of all observables are plotted as function of $\frac{1}{L^2}$. With the leading finite size correction being quadratic, as noted in Equation 5.18, the respective values of $T_c^O(L)$ are used to extrapolate the transition temperature T_c^{PIM} . All extrapolations show a good agreement within errorbars. As the peaks in χ are more pronounced and sharper we use $T_c^\chi = 3.61(2)$ for our final phase diagram, which is in perfect agreement with the literature value $T_c^{PIM} = 3.6273(5)$ reported in [92].

Thus the histogram at β_0 can be calculated by reweighting the original histogram by the factor $e^{-(\beta_0 - \beta)E}$. The application of the method is presented for the $p^X = 0$ case of the RPI model in Figure 5.3, where the left picture shows the original histograms for different system sizes directly measured in the MC simulations, and the right panel displays the histograms after the respective reweighting, revealing the finite-size transition points $T_c^{P(E)}(L)$.

All order parameters are taken into account individually. For each observable the extrapolated transition temperature in the thermodynamic limit is determined according to the scaling relation, given in Equation 5.18, using the respective finite-size transition points, shown in Figure 5.2 and Figure 5.3(b). The consensus for the resulting transition temperature is shown in Figure 5.4.

Figure 5.4 demonstrates the validity of our numerical approach, where we carefully analyse all figures of interest, and find an agreement of the extrapolated transition temperature. Even though we are limited to smaller system sizes with our simulations using parallel tempering, we are not reliant on guessing an a priori unknown weight

function as used in multicanonical methods. This weight function would be different for every instance of a quenched disorder system. Thus we are able to efficiently perform calculations for finite disorder ($p > 0$).

The same benchmark with simulations for the RACAT model showed a similar qualitative agreement to the literature value, known in the absence of disorder. However, we focused the computational efforts on the finite p regime. For the disorder free case of the ATM we use the exact duality relation to the PIM, valid in the $p = 0$ case, which is discussed in Appendix B,

$$\sinh(2\beta_c^{ATM}) \sinh(2\beta_c^{PIM}) = 1 \quad (5.21)$$

where β_c^{ATM} is the respective transition temperature for the ATM [92, 95]. Using Equation 5.21 we can thus conclude $T_c^{ATM} = 1.522(4)$.

5.2 First-order phase transition regime

In the presence of disorder ($p > 0$) we are not aware of any previous studies, that considered the RPI or the RACAT model. Previous studies that introduced quenched disorder in classical spin systems found ordered phases for finite regions in the $(T - p)$ phase diagram [61]. Even though it is known, that a first-order PT at $p = 0$ can be changed to a second-order PT by introducing quenched disorder in the system [96], for a finite but small amount of disorder the transition is observed to remain discontinuous. Thus we start with small values of p for both models to show how the observables, defined in Equation 5.9-5.12, change with increasing disorder in the system. In Figure 5.5 the energy density histogram is shown in combination with the respective Binder cumulants for increasing values of p^X .

The visibly shrinking dips for the Binder cumulants, displayed in Figure 5.5(f), which are associated with the finite size transition points, indicate that most likely the PT is no longer discontinuous, as the non-monotonic dips are not diverging any more with the system size. The latent heat, characteristic for a first order PT, which is reflected by the distance ΔE between the double peaks of $P(E)$, shown in Figure 5.5[(a)-(c)], shrinks with increasing p , and is further evidence that the quenched disorder weakens the first-order PTs. The alluded trend, from a first-order PT at small values of p to a second-order PT close to the threshold regime, as shown

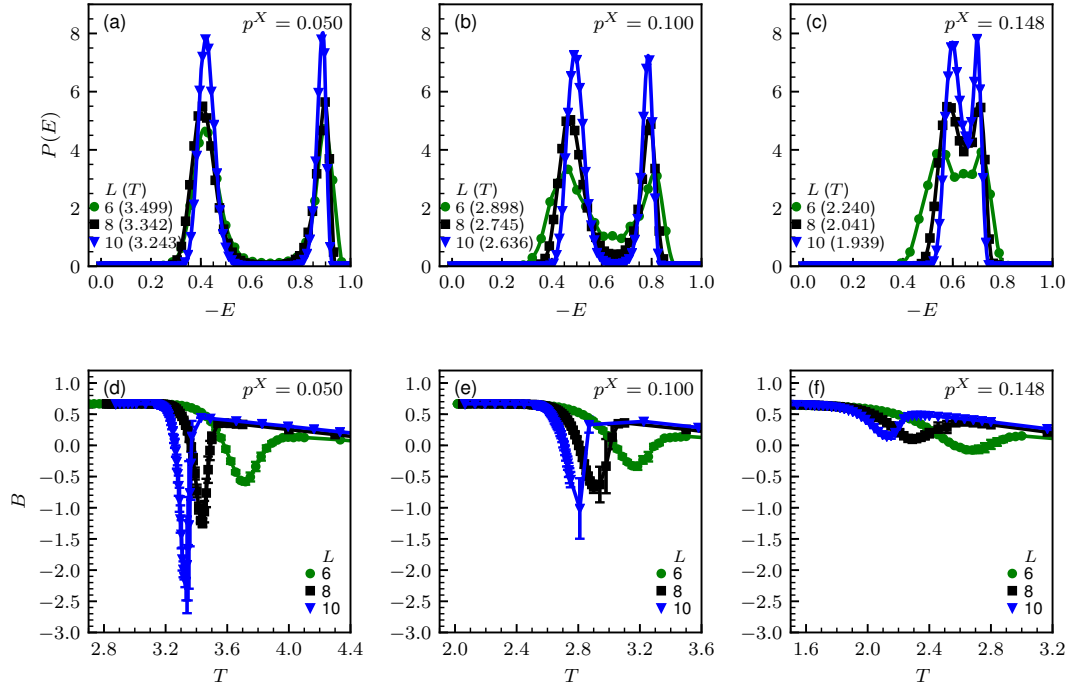


Figure 5.5: [(a)-(c)] The energy density histograms for the 3D RPI model at different error rates. [(d)-(f)] Binder cumulants at the corresponding p^X values. For small p^Z values, both the double-peak structure in $P(E)$ [(a), (b)] and the dip in B [(d), (e)] grow sharper with increasing L , as expected for first-order PTs. When approaching larger p values $p^X \simeq 0.148$, the two $P(E)$ peaks do not evolve towards separated δ -functions, as the weight of the valley retains a finite value with increasing L . Consistently, the B dips also do not diverge. The features visible in (c) and (f), most likely correspond to finite-size effects of a continuous PT. This picture is consistent with Figure 5.6(c) and (f) where χ and c_V is considered for $p^X = 0.148$.

in Figure 5.5, is fully consistent with our measurements of the susceptibility and the specific heat capacity. χ and c_V for the same disorder values are shown in Figure 5.6 for the RPI model. The rounding effect of the disorder is also directly evident in the blurring of the peaks at large p values, shown in Figure 5.6[(c), (f)].

Figure 5.7 presents our findings of the energy density histograms and Binder cumulants for the RACAT model for increasing phase-flip error rates p^Z . Figure 5.6 completes the low p regime for the RACAT model with our results for χ and c_V . The behaviour is reminiscent to our findings for the RPI model with second-order PTs appearing around $p^Z \simeq 0.075$.

Our measurements of the respective figures of merit, defined in Equation 5.9-5.12,

5.2 First-order phase transition regime

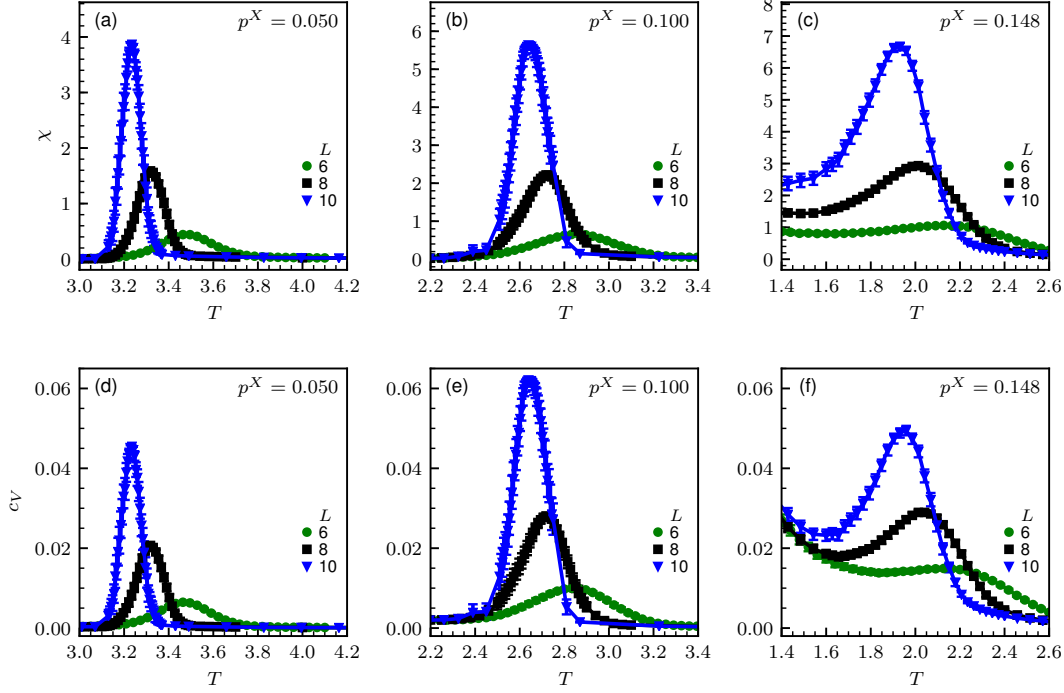


Figure 5.6: [(a)-(c)] The susceptibility for the 3D RPI model at the p values shown in Figure 5.5. [(d)-(f)] The respective specific heat capacities at the corresponding disorder values. For small p^X values both the peaks in χ [(a), (b)] as well as those for c_V [(d), (e)] grow sharper and diverge with increasing L , as expected for first-order PTs. When approaching stronger disorder $p^X \simeq 0.148$, the peaks start to blur out for small lattice sizes. Consistently with Figure 5.5 the observables, defined in Equation 5.9-5.12, do not allow for a reliable extrapolation of the transition temperature close to the error threshold p_c^X , and the features in (c) and (f) most likely correspond to finite-size effects of a continuous PT.

affirm that the PT remains of first-order in the small p regimes of both models. Close to the thresholds, although $P(E)$ in Figure 5.5(c) and Figure 5.7(c) are still showing two peaks, the weight of the valley between them does not evolve towards zero, when increasing L . This implies, that the double peaks will not evolve into two distinct δ -functions at two E values in the infinite size limit. This is in contrast to the case of the first-order PTs in the small p regime. Consistently, the dips in the corresponding B curves do not diverge in Figure 5.5(f) and Figure 5.7(f). Such a non-diverging behavior is also observed as a finite-size effect in simulations of the 2D 4-state Potts model [97], where the PT is analytically known to be continuous [98].

The presented data suggests that the PTs of the 3D RPI and RACAT model are discontinuous in the low p regions. Thus we determine the transition temperature for

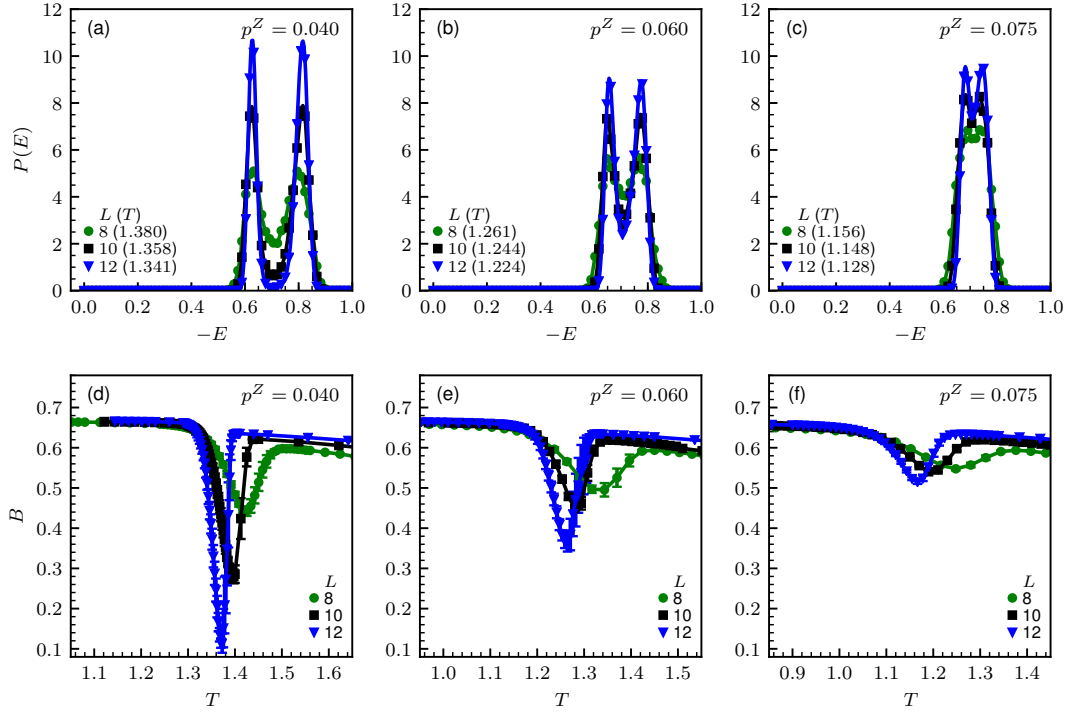


Figure 5.7: [(a)-(c)] The energy density histograms for the 3D RACAT model at different error rates. [(d)-(f)] Binder cumulants at the corresponding disorder values. As in the case of the RPI model the system experiences discontinuous PTs in the small p regime. The quenched disorder weakens the discontinuity as the distance ΔE between the two $P(E)$ peaks shrinks upon increasing p . The non-divergent peaks and dips in (c) and (f) most likely correspond to finite-size effects of a second-order PT.

the first-order PT regime in analogy to the disorder free case.

Figure 5.9 demonstrates the consistency of the transition temperature extrapolated from all observables, defined in Equation 5.9-5.12, for the small p regime. Within error bars all observables extrapolate to the same transition temperature for increasing p values similar to the comparison in Figure 5.4. With increasing p the first-order phase transitions gradually soften. Even though the correlation length will eventually exceed the system sizes of our simulations, and larger system sizes are expected to improve the precision on the transition temperatures, this should only have minimal consequences in determining the error thresholds, as the estimated transition temperatures are sufficiently above the Nishimori line. For the optimal error threshold regime we rely on the correlation length, defined in Equation 5.14. The precise evaluation is described in the next section.

5.2 First-order phase transition regime

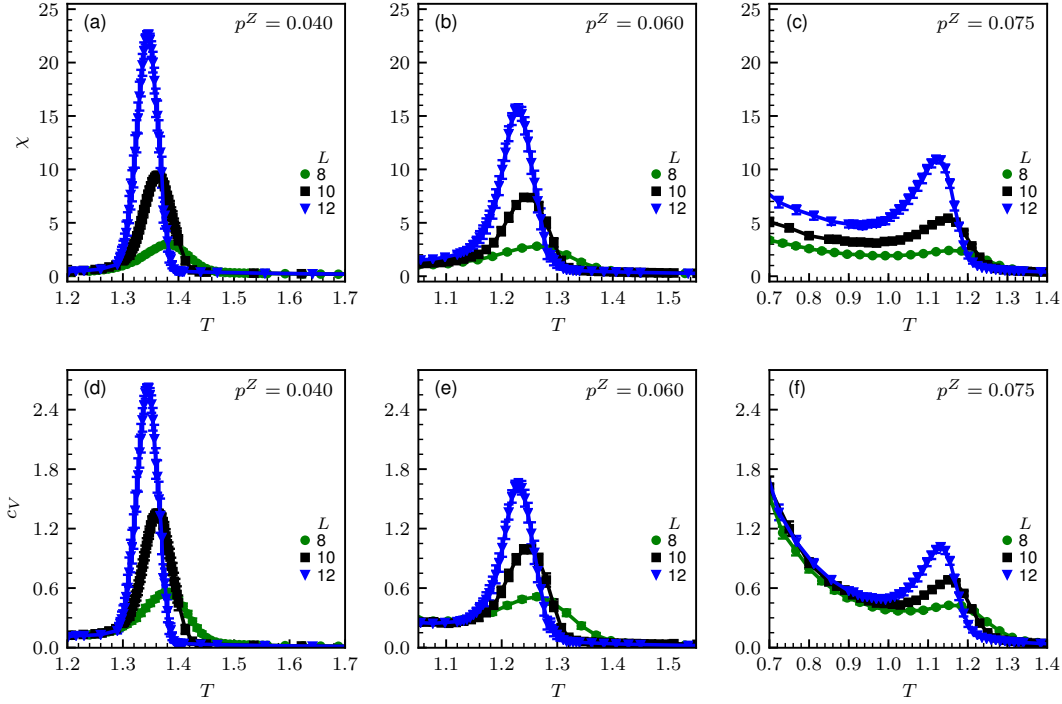


Figure 5.8: [(a)-(c)] The susceptibility for the 3D RACAT model at the p values shown in **Figure 5.7**. [(d)-(f)] The respective specific heat capacities at the corresponding disorder values. As in the case of the RPI model, the χ and c_V measurements support the impression, that the system experiences discontinuous PTs in the small p regime.

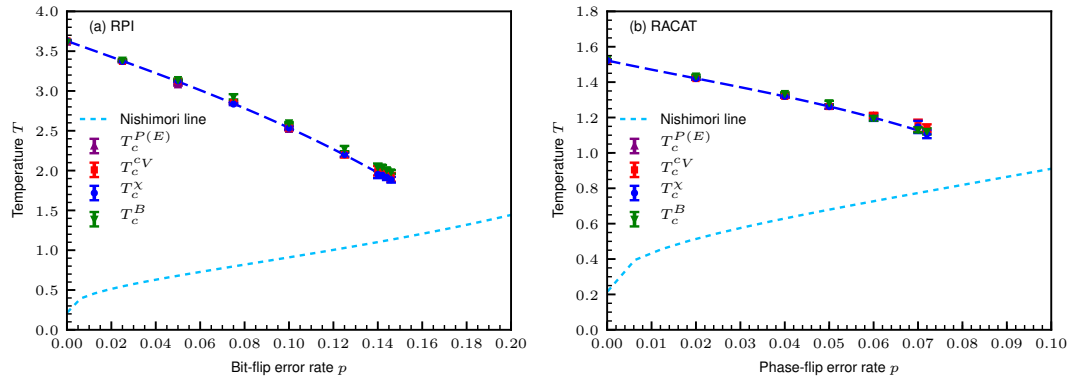


Figure 5.9: (a) Phase boundary of the discontinuous PT of the RPI model. (b) Phase boundary of the discontinuous PT of the RACAT model. The transition temperatures T_c^O are estimated by fitting the non-standard scaling relation Equation 5.18 for each observable individually. The results for $T_c^{P(E)}$, T_c^{cV} , T_c^X and T_c^B are compared.

5.3 Second-order phase transition regime and optimal error-threshold values

In the mapping of local phase- and bit-flip errors, as discussed in Section 3.6, temperature is only introduced auxiliary by Equation 3.27

$$e^{-\frac{2}{T}} = \frac{p}{1-p}, \quad (5.22)$$

which defines the Nishimori line. Only pairs of (p, T) values, satisfying this relation, are directly relatable to the error-correcting code. Namely, a correctable X-cube code configuration corresponds to the part of the Nishimori line inside the ordered phase of the RPI or RACAT model. Clearly, the high-temperature phase for both models is trivially disordered. We can thereby estimate the optimal error-threshold values p_c^X and p_c^Z by the largest error rates exhibiting an order-disorder PT.

As we have shown in Section 5.2 the PTs are continuous for large enough p values in both models. Thus we use $\xi_L(\beta, L)$, as defined in Equation 5.14, as an estimator. In the vicinity of a critical point, ξ_L scales as [99]

$$\frac{\xi_L}{L} = g\left(L^{1/\nu}(T - T_c)\right). \quad (5.23)$$

Thus ξ_L/L for different sizes is expect to intersect near T_c , where g is a universal scaling function, and ν is the critical exponent of correlation length. A "global" fit, as proposed by Katzgraber et al. [99], is not reasonable with our lattice sizes at hand, as ν is not known analytically for our models. Therefore we rely on the evaluation of the crossing behaviour of ξ_L/L as function of the temperature. Figure 5.10 presents the curves of ξ_L/L for increasing p values close to the optimal error thresholds. A clear intersection across all available lattice sizes, which implies a second-order PT, can be observed in Figure 5.10[(a), (b)] for the RPI model and in Figure 5.10[(d), (e)] for the RACAT model.

For larger disorder values $p > p_c^X$ in the RPI model or $p > p_c^Z$ in the RACAT model the intersections become either very ambiguous, as in Figure 5.10(f), or display multiple intersections, as in Figure 5.10(c), indicating strong finite size effects, which will lead to either a continuing flow to $T = 0$, or a T_c far below the Nishimori line, when considering the thermodynamic limit. In either case these p values can serve as upper bound on the optimal error thresholds, which is represented by the crossing of the phase boundary with the Nishimori line.

5.3 Second-order phase transition regime and optimal error-threshold values

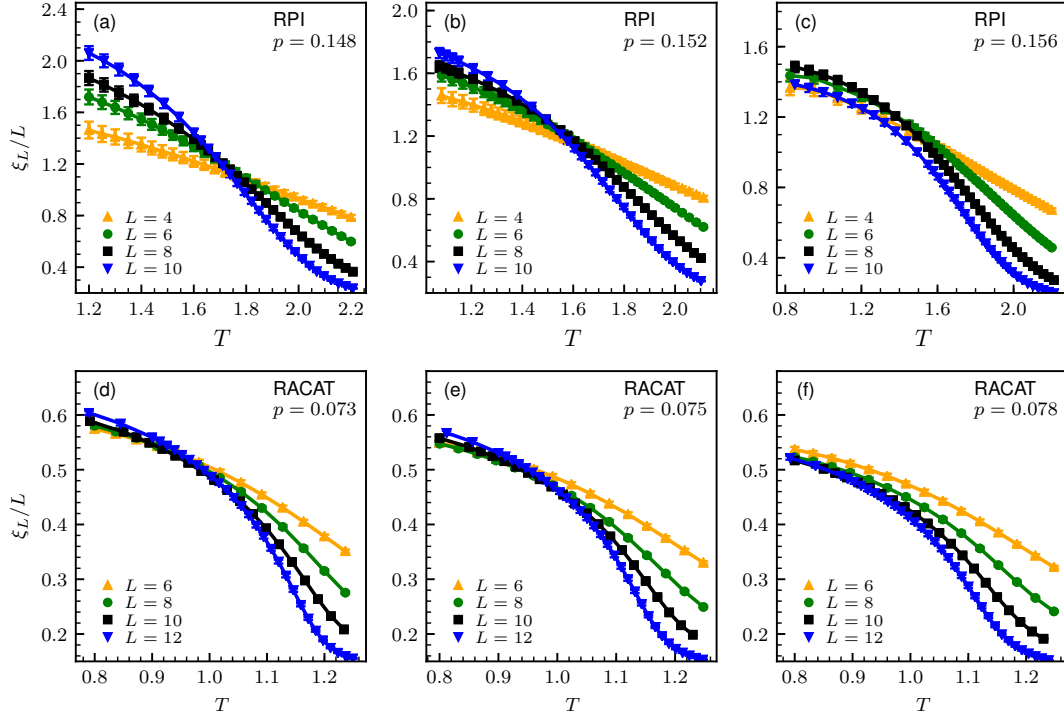


Figure 5.10: [(a)-(c)] Normalized second-moment correlation length for the 3D RPI model across the respective optimal error threshold regime for p_c^X . [(d)-(f)] Normalized second-moment correlation length for the RACAT model in the vicinity of the estimated optimal error thresholds of p_c^Z . A clear intersection of all ξ_L/L curves is visible around $p_c^X \simeq 0.152$ for the RPI model and around $p_c^Z \simeq 0.075(2)$ for the RACAT model. For $p > p_c^X$ or p_c^Z , the intersection becomes ambiguous, or the lines do not intersect in a single point, indicating that no order-disorder PT is present at the relevant temperature regime close to the Nishimori line.

Combining our results from the small p regime, presented in Figure 5.9, with the critical points at larger p values from the crossings of ξ_L/L , we determine the phase diagrams for the RPI model and the RACAT model. They are shown in Figure 5.11.

As error correction in the X-cube model is only feasible, if the (p, T) point, used in the mapping with Equation 3.27, belongs to the ordered phases of the RPI model and the RACAT model, we can determine the optimal error threshold as the largest allowed p value, for which we can find an ordered phase in the respective spin models. Thus we determine the optimal error thresholds to be $p_c^X \simeq 0.152(4)$ from the phase diagram of the RPI model in Figure 5.11(a) and $p_c^Z \simeq 0.075(2)$ from the phase diagram of the RACAT model in Figure 5.11(b). We assumed, that phase-flip and bit-flip errors occur with the same probability p , as

described in Chapter 3, in a symmetric and uncorrelated fashion. Thus the lower error threshold is the dominant one, which has to be satisfied. The minimum error threshold for the X-cube model is thus $p_c = 0.075(2)$ [P1]. It should be noted that our results $H(p_c^X) + H(p_c^Z) \simeq 1.00(2)$ suggest an almost saturated quantum Gilbert-Varshamov bound [100–102]. There H denotes the Shannon entropy from Equation B.8 which is also used for the approximate duality relation in Appendix B. Thus our numerical results coincide with the analytically established result in Equation B.7 [P1].

5.3 Second-order phase transition regime and optimal error-threshold values

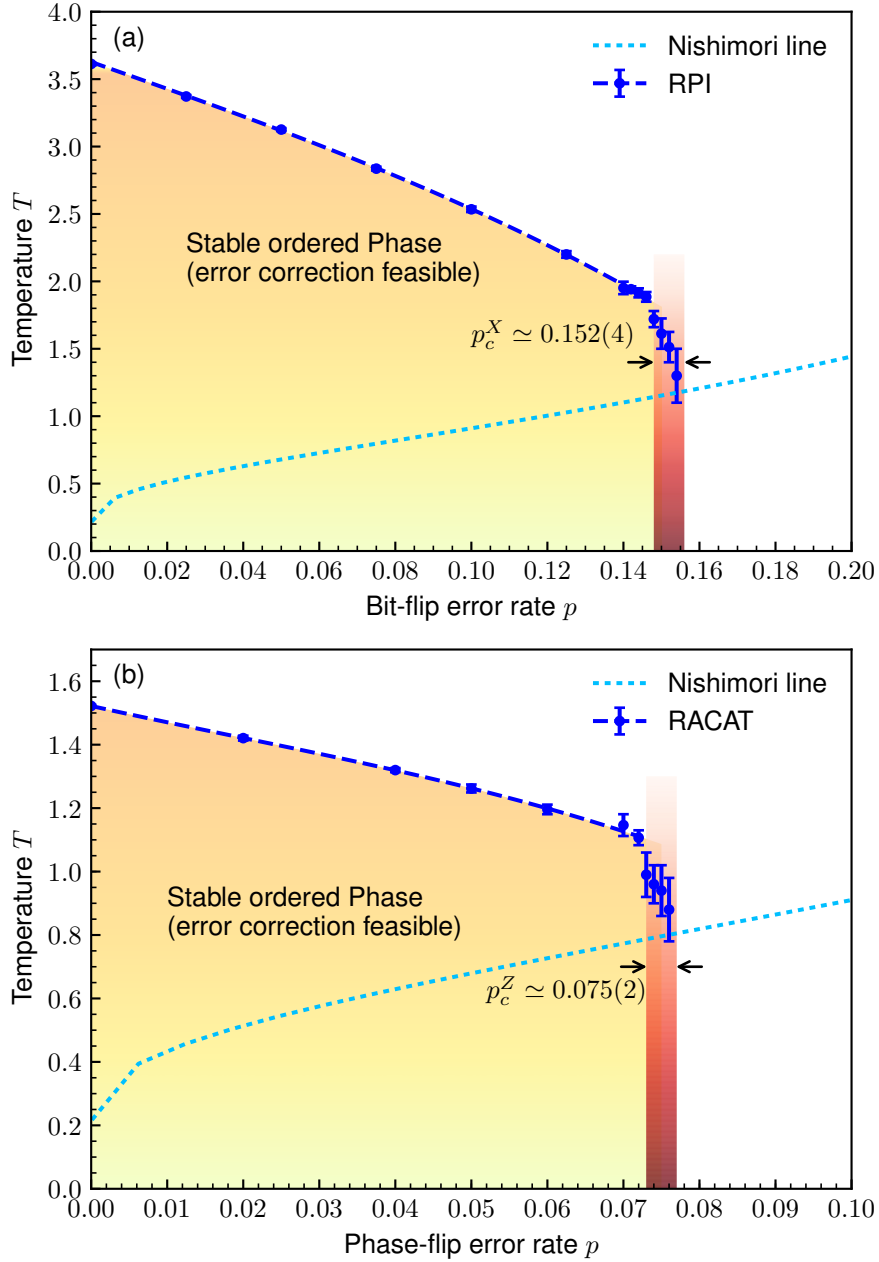


Figure 5.11: (a) The phase diagram for the 3D RPI model. (b) The phase diagram for the 3D RACAT model. We used parallel tempering MC simulations to determine the phase boundary between the ordered low T phase and disordered high T phase. The PTs are discontinuous in the low p regime of both models and turn into second-order PTs close to the optimal error threshold values. The error thresholds are determined by finding the largest p values, displaying a PT from the ordered to disordered phase, as a X-cube model configuration is only correctable, if it corresponds to an (p, T) point within the ordered phase. Thus we find the optimal error thresholds $p_c^X \simeq 0.152(4)$ and $p_c^Z \simeq 0.075(2)$.

Part II

Spinfu! Bose-Fermi-Hubbard Model

Chapter 6

Bosons and Fermions in lattices

Due to their clean and fully controllable, yet versatile set-up quantum gases in optical lattices have proven to represent an ideal candidate to realize a quantum simulator for classically incomputable many-body problems in condensed matter theory [28, 29]. For monoatomic bosonic gases, trapped in a 3D optical lattice, the theoretically predicted [103, 104] quantum phase transition from a Mott insulator to a superfluid was experimentally proven to exist [105]. Recently a quantum simulator for the dynamics of the 1D FHM with spinful fermions was successfully realized [20].

Multicomponent systems comprised of bosons and fermions are ubiquitous in nature as well as in technologically highly relevant materials, like high T_c superconductors [1, 30]. Neutral atom based quantum simulators aiming at a realistic representation of these multicomponent systems thus will need to be able to contain a mixture of bosons and fermions in a single fully controllable optical lattice.

The theoretical and experimental efforts in the study of bose-fermi mixtures picked up momentum after the first succesful demonstration of an experimental confinement of fermionic ^{40}K and bosonic ^{87}Rb atoms in a single 3D optical lattice [106]. Beyond the phases of their individual constituents such mixtures are predicted to display an abundance of exotic quantum phases.

Initially purely fermionic or bosonic systems in optical lattices were realized. Today experimentalists can create multicomponent systems by including different isotopes of the same atom [107], different atoms [106] or different hyperfine states of one type of atom [108]. It was demonstrated, that interspecies interactions are capable of shifting the critical transition line between Mott-insulating and superfluid regimes [109]. A phase with simultaneous superfluidity in both spinful fermionic ^6Li and bosonic ^7Li atoms was realized [107]. Using the same constituents, but slightly changing the lattice parameters, counterflow was observed [110].

Even the simplest theoretical model for mixtures of scalar bosons and spin

polarized fermions, namely the Bose-Fermi-Hubbard model (BFHM) [111], is notoriously challenging to study due to competing energy scales and has been investigated intensively. Using bosonization a first sketch of the spin polarized BFHM in 1D was presented [112], predicting a charge density wave (CDW), a phase with fermion pairing [113] and a regime of phase separation (PS). The same model in the heavy fermion limit was studied with an analytical strong coupling expansion, underpinned by numerical simulations, based on the density matrix renormalization group (DMRG) method [114].

Allowing spinful fermions in the BFHM, introduces yet another interaction parameter U_{FF} . In this scenario bosonization predicts for 1D an even richer phase diagram, including a SDW, CDW, a Wigner crystal phase, singlet and triplet paired states of fermions, and a PS regime [112].

In this part of the thesis we investigate the question, which types of interactions can be induced as intraspecies coupling between the fermions from different bosonic backgrounds, belonging to weak, intermediate and strong coupling regimes. We present the ground state phase diagram for the spinful BFHM at unit filling for the bosons and half filling for the fermions. To study the mutually induced interactions, the bare fermionic interaction is set to zero.

Before we discuss the Hamiltonian of the spinful Bose-Fermi-Hubbard model (sBFHM) in Section 6.3, describing mixtures of bosonic and fermionic systems in a lowest band approximation, we will highlight the most relevant aspects of purely bosonic and purely fermionic Hubbard models in Section 6.1 and Section 6.2.

6.1 Bosonic Hubbard models

To be able to interpret the physics emerging in the BHM, compared to what is visible in optical lattice experiments, let us briefly discuss, how the model is motivated in one dimension. The general many-body Hamiltonian, that allows interactions of up to two particles, can be written as

$$H = \int dx \psi^\dagger(x) \left[-\frac{\hbar^2}{2m} \nabla^2 + V_{latt}(x) + V_{trap}(x) \right] \psi(x) + \frac{1}{2} \iint dx dx' \psi^\dagger(x) \psi^\dagger(x') V_{int}(x, x') \psi(x') \psi(x), \quad (6.1)$$

where the first integration is describing the contributions of each individual particle with the kinetic energy $-\frac{\hbar^2}{2m} \nabla^2$, the external trapping potential $V_{trap}(x)$, which confines the atoms to the lattice regime and the periodic lattice potential $V_{latt}(x)$.

6.1 Bosonic Hubbard models

$V_{int}(x, x')$ is the interaction potential among the particles, located at the spatial coordinates x and x' . $\psi^\dagger(x) = \sum_i \varphi_i^*(x) \hat{b}_i^\dagger$ and $\psi(x) = \sum_i \varphi_i(x) \hat{b}_i$ are the field operators for creation and annihilation at positions x , which satisfy bosonic commutation relations [115, 116]. These operators can be expanded with any complete basis set $\{\varphi_i\}$. How the individual potentials can be realized experimentally depends on the types of atoms, and we refer the reader to the reviews [28, 117] for a precise description of the experimental techniques.

For a general periodic lattice potential the eigenstates of $V_{latt}(x)$ are given by Bloch functions $u_q^n(x)$, which are characterized by a discrete band index n and a quasimomentum q . These Bloch functions are extended over the whole lattice. However, for sufficiently deep lattice potentials and low enough temperatures the bosons are expected to be localized at the centers $x_i = ia$ of the i th minima of $V_{latt}(x)$, with exponential decay away from the minima locations $x - x_i$ [28]. When assuming, that only the lowest Bloch band is occupied, such a behaviour is well described by Wannier functions, which can be represented as Fourier transform of the Bloch functions with quasimomenta, belonging to the first Brillouin zone

$$w(x - x_i) = \frac{a}{2\pi} \int dq u_q(x) e^{-iqx_i}. \quad (6.2)$$

As the Wannier functions provide a full single particle basis, they can be used for the expansion of the field operators in Equation 6.1. With the representation

$$\psi^\dagger(x) = \sum_i w^*(x - x_i) \hat{b}_i^\dagger \quad (6.3)$$

$$\psi(x) = \sum_i w(x - x_i) \hat{b}_i \quad (6.4)$$

it is then possible to rewrite Equation 6.1. The result is

$$H = \sum_{i,j} t_{ij} \hat{b}_i^\dagger \hat{b}_j + \frac{1}{2} \sum_{ijkl} U_{i,j,k,l} \hat{b}_i^\dagger \hat{b}_j^\dagger \hat{b}_k \hat{b}_l + \sum_i \mu_i \hat{b}_i^\dagger \hat{b}_i \quad (6.5)$$

with the kinetic energy rewritten as hopping between lattice sites in the first term. Interactions among particles are summarized in the second term, and the trapping potential is rewritten as site dependent chemical potential. The three resulting parameters are defined as

$$t_{ij} = \int dx w^*(x - x_i) \left[-\frac{\hbar^2}{2m} \nabla^2 + V_{latt}(x) \right] w(x - x_j) \quad (6.6)$$

$$U_{ijkl} = \iint dx dx' w^*(x - x_i) w^*(x - x_j) V_{int}(x, x') w(x - x_k) w(x - x_l) \quad (6.7)$$

$$\mu_i = \int dx w^*(x - x_i) [V_{trap}(x)] w(x - x_i). \quad (6.8)$$

Equation 6.5 is still quite general and not solvable analytically, nor directly accessible numerically in general. To be able to study bosonic gases, it is necessary to further simplify the model and consider certain limiting cases of Equation 6.5, motivated by realistic assumptions. The most prominent model, based on the above description, is the BHM. It assumes, that there are only on site contact interactions with an amplitude U , and restricts the hoppings universally to adjacent next neighbour sites with a hopping amplitude t . In Subsection 6.1.1 we will discuss the most important physics relevant for our studies. Furthermore in Subsection 6.1.2 we highlight some of the findings for the eBHM, which is an extension of the BHM. It introduces additional interactions among next neighbour sites with coupling constant V .

6.1.1 Bose-Hubbard model

The last term in Equation 6.5 takes the effect of a trapping potential V_{trap} on the system into account. This term has interesting effects on the quantum system and can for example result in local differences in the occupation number. This was examined theoretically with QMC methods [118] and a numerical renormalization group approach [119]. The theoretical prediction was confirmed experimentally with a bosonic gas in an optical lattice [120]. However, in this thesis we will not consider the implications of the external trapping potential on the system, but study the competition of the internal energy scales. To this end we assume fixed filling factors within the simulations, which is done by choosing the correct chemical potential. However, the chemical potential is never explicitly site dependent and is therefore omitted from the Hamiltonians.

The BHM Hamiltonian without an external trapping potential can be written as

$$H_{\text{BHM}} = -t_b \sum_{\langle i,j \rangle} \hat{b}_i^\dagger \hat{b}_j + \frac{U_{BB}}{2} \sum_i \hat{n}_{i,b} (\hat{n}_{i,b} - 1), \quad (6.9)$$

where $\langle i, j \rangle$ denotes a summation over all pairs of next neighbours and $\hat{n}_{i,b} = \hat{b}_i^\dagger \hat{b}_i$ is the local bosonic density operator. The second sum is running over all L lattice sites. It is obtained from Equation 6.5 by the choice $U_{iii} \equiv U_{BB}$ and zero amplitude for any other combination of indices and the hopping restricted to next neighbours with amplitude $t_{ij} \equiv -t_b$. The density-density coupling results from $\hat{b}_i^\dagger \hat{b}_i^\dagger \hat{b}_i \hat{b}_i = \hat{n}_{i,b} (\hat{n}_{i,b} - 1)$, which takes the bosonic commutation relations into account.

As the quantum PT, present in this model, is driven by the ratio of the coupling constants U and t , let us consider the two limiting cases of $U_{BB} = 0$ or $t_b = 0$.

In the noninteracting limit $U_{BB} = 0$ all bosons will be in the zero momentum Bloch eigenstate in the thermodynamic limit [28]. For small, but finite values of $U \ll t$ the system is well described by the Bogoliubov approximation and is in the SF phase. It assumes, that a large fraction N_0 of the bosons is still in the condensate state, and the expectation values of the Fourier transformed creation and annihilation operators can be approximated as $\langle \tilde{b}_0^\dagger \rangle \approx \langle \tilde{b}_0 \rangle \approx \sqrt{N_0}$ with small additional fluctuations, which are again described as creation and annihilation operators respectively. This approximation is inserted in Equation 6.9, and only terms up to second order in \tilde{b}_0^\dagger and \tilde{b}_0 are kept. The resulting Hamiltonian is quadratic and can be diagonalized by a Bogoliubov transformation [121], resulting in a gapless excitation spectrum.

The MI phase is present in the opposite parameter regime $U_{BB} \gg t_b$ for integer lattice fillings. Let us consider the case of an average filling of one boson per lattice site $\langle n_b \rangle = 1$. In the limiting case of $t = 0$ the obvious many-body ground state is a Fock state with one particle residing on each lattice site $|\psi_G^{t=0}\rangle = \prod_i \hat{b}_i^\dagger |0\rangle$, as any double occupancy would cost an energy U_{BB} . For finite, but small values of $t \ll U$, the ground state is no longer a simple product as in $|\psi_G^{t=0}\rangle$. It is more favorable to localize the bosons on each site, rather than to have them in plane wave states. Analytically mean field approximations predict a phase diagram including a MI and a SF regime.

These perturbative arguments only hold in their respective parameter regimes $U \ll t$ (SF) and $U \gg t$ (MI). Thus numerical methods have to be applied to determine the physical properties of the system in the intermediate regime.

The BHM has been investigated extensively, studying the ground state phase diagrams in various dimensions as well as dimensional crossovers [P2, 127]. The phase diagram in 3D, including SF and MI regimes, was predicted by theory [103, 104], and the respective phase transition was realized experimentally [105]. A discussion on recent developments and various extensions of the model can be found in the review by Dutta et al. [30].

In higher dimensions $d > 1$ the transition at fixed density is of second-order and the Mott lobes have a round shape, but in 1D this transition is of KT type. Figure 6.1 shows the phase diagram of the BHM in 1D with the characteristic sharp tip of the Mott lobe [122]. In contrast to the phase diagrams of the BHM in higher dimensions here it is possible, to reenter the superfluid phase at fixed chemical potential by tuning the ratio U/t .

In 1D superfluidity is described as a Luttinger liquid (LL). The MI-SF PT, at commensurate density, can be characterized by the Luttinger parameter K_b [128] and

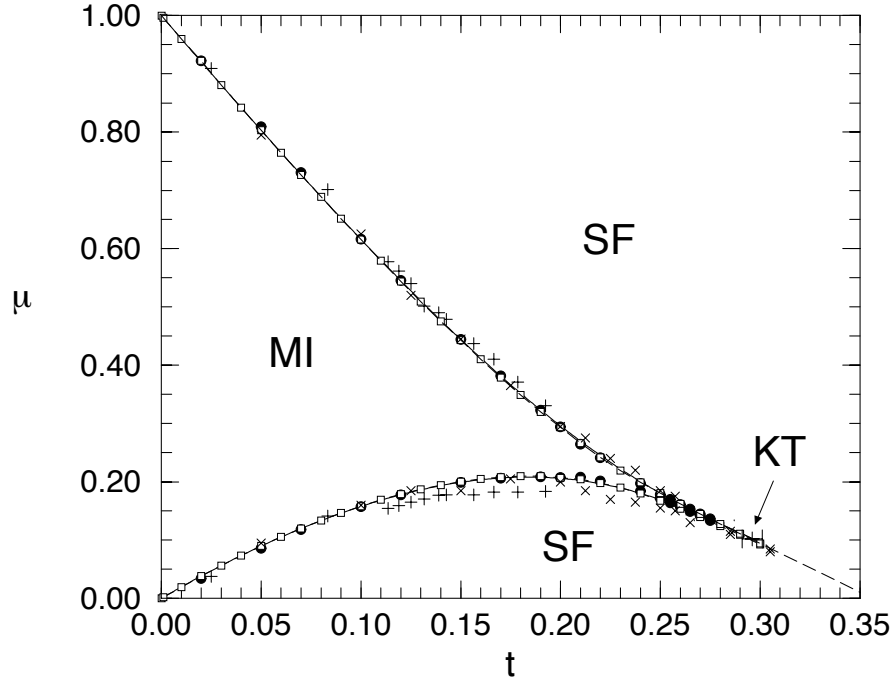


Figure 6.1: $(\mu - t)$ phase diagram of the 1D BHM, reprinted from [122]. The energy scale is fixed by setting $U_{BB} = 1$. The hopping $t_b = t$ is plotted versus the chemical potential μ . The MI phase with unity filling $\langle n_b \rangle = 1$ is present for small values of t , and the SF phase is found at large values of t . The phase diagram shows multiple numerical results, based on a Padé analysis [123], QMC simulations [124, 125] and DMRG [122, 126]. The dashed line visualizes the line corresponding to $\langle n_b \rangle = 1$ in the SF. The phase transition at constant density is of the Kosterlitz-Thouless (KT) type.

the bosonic speed of sound v_b . Later on we consider multiple interactions, and our energy scale is fixed by setting $t = 1$. In these units the critical interaction strength for this transition is $U_{BB}^c = 3.29(2)$ [125]. To study the thermodynamical limit, while only being able to simulate finite systems, it is useful to consider the lowest order renormalization group flow equations of the sine-Gordon model

$$\frac{dK_b}{d\ln(L)} = -\delta g^2, \quad (6.10)$$

$$\frac{dg}{d\ln(L)} = (2 - K_b)g, \quad (6.11)$$

which are governing the above KT transition. The phase transition happens at $K_b^c = 2$, with $K_b < 2$ belonging to the MI phase, whereas $K_b > 2$ indicates a SF phase [128].

In the worm algorithm, described in Chapter 7, the Luttinger parameter is accessible by two methods.

The bosonic Green's function $\mathcal{G}^b(i-j) = \langle \hat{b}_i^\dagger \hat{b}_j + h.c. \rangle$, which decays either as power law or exponentially with the distance $x = (i-j)$, is able to characterize the system [128, 129]. In the LL phase of a finite system of size L with periodic boundary conditions it decays asymptotically as a power law

$$\mathcal{G}^b(x) \propto (d(x|L))^{-\frac{1}{2K_b}}, \quad (6.12)$$

where the cord function $(d(x|L)) = \left| \sin\left(\frac{\pi x}{L}\right) \right|$ accounts for the boundary conditions.

Alternatively the bare Luttinger parameter can be determined as

$$K_b = \pi \sqrt{\kappa \rho_{s,b}} = \pi \sqrt{\langle W_{b,x}^2 \rangle \langle W_{b,\tau}^2 \rangle}, \quad (6.13)$$

where κ is the compressibility and $\rho_{s,b}$ the bosonic superfluid density. These quantities are accessible through the winding numbers as

$$\kappa = \frac{\beta}{L} \langle W_{b,\tau}^2 \rangle = \frac{\beta}{L} \left(\langle N_b^2 \rangle - \langle N_b \rangle^2 \right) \quad (6.14)$$

$$\rho_{s,b} = \frac{L}{\beta} \langle W_{b,x}^2 \rangle. \quad (6.15)$$

From the winding numbers, also the speed of sound, which is not renormalizable in the LL [125], can be calculated as

$$v_b = \frac{L}{\beta} \sqrt{\frac{\langle W_{b,x}^2 \rangle}{\langle W_{b,\tau}^2 \rangle}}. \quad (6.16)$$

It should be noted, that the commensurate-incommensurate transition, away from the tip of the lobe, is not of the KT type, and thus has to be analysed differently [122].

6.1.2 Extended Bose-Hubbard model

One of the most prominent extensions for the BHM is to take nearest neighbour interactions into account. Particles are then attracting or repelling each other, if they occupy adjacent sites, dependent on the sign of V . The Hamiltonian of the extended Bose-Hubbard model (eBHM) is given by

$$H_{\text{eBHM}} = -t_b \sum_{\langle i,j \rangle} \hat{b}_i^\dagger \hat{b}_j + \frac{U_{BB}}{2} \sum_i \hat{n}_{i,b} (\hat{n}_{i,b} - 1) + V \sum_i \hat{n}_{i,b} \hat{n}_{i+1,b}. \quad (6.17)$$

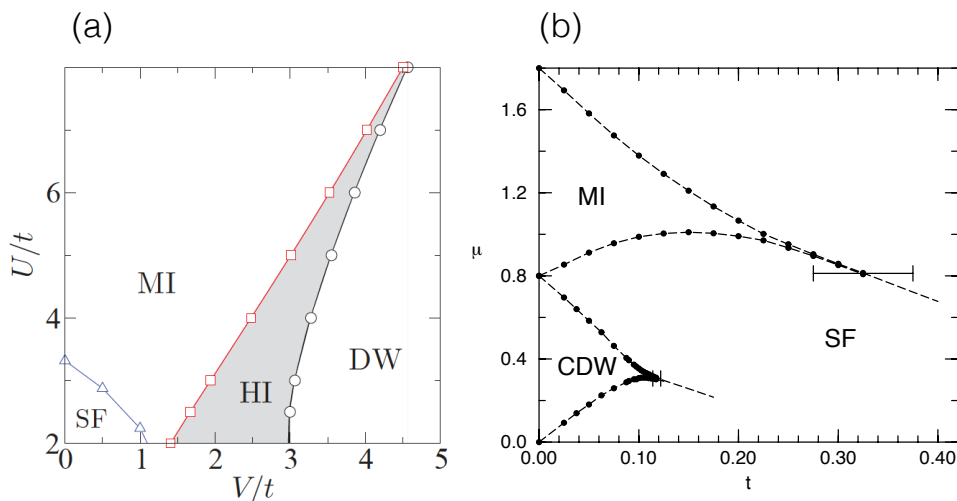


Figure 6.2: (a) $(U - V)$ phase diagram of the 1D eBHM reprinted from [131]. The energy scale is fixed by setting $t_b = t = 1$ and $U_{BB} = U$. The bosonic density is fixed to $\langle n_b \rangle = 1$. The DMRG method allowed at most two bosons per lattice site. In the limit $V = 0$ the SF-MI transition is replicated. The SF phase extends to finite, but small values of V , but the repulsive next nearest neighbour interactions in this regime favour the MI state, thus the transition line bends downward. For larger values of V there is no superfluid phase found anymore, but the system can traverse into a Haldane insulator (HI) and then into a CDW with doubly occupied sites as $V \gg U$ (Here referred to as DW). (b) $(\mu - t)$ phase diagram of the 1D eBHM reprinted from [126]. The energy scale is fixed by $t = 1$ and $V = 0.4t$. Apart from the MI lobe with commensurate density $\langle n_b \rangle = 1$, also a CDW lobe with $\langle n_b \rangle = \frac{1}{2}$ can be found at this parameter choice.

The model was studied by a meanfield approximation with numerical support of a QMC algorithm in two dimensions [130]. For one dimension Figure 6.2 shows the $(\mu - t)$ phase diagram for $V = 0.4$ on the right and the $(U_{BB} - V)$ phase diagram on the left. When μ is increased within the system, more and more particles are added.

When t_b is small enough and the next nearest neighbour interactions are present, a CDW phase appears with half filling, as displayed in Figure 6.2(b), where every second lattice site is occupied. This phase is easily understood, if one considers the $t = 0$ and $V \gg U > 0$ case. The bosons are completely localized and have no kinetic energy. As $U > 0$, it is energetically not favourable for the bosons to be on the same site. However, as $V \gg U$, being on neighbouring sites is energetically even less favourable, and thus the bosons are spread across the system on every second lattice site. A CDW is also stable at higher half integer filling fractions [122]. The order parameter for the CDW is given by the structure factor $S^{\text{bos}}(k)$ at $k = \pi$, since the

period is 2 lattice sites, with

$$S^{\text{bos}}(k) = \sum_j e^{ikj} C^b(j), \quad (6.18)$$

where $C^b(j) = \langle \hat{n}_{i,b} \hat{n}_{0,b} \rangle - 1$ is the connected density-density correlation function. Figure 6.3 shows the typical strong, local fluctuations in the bosonic occupation number $\langle n_{b,i} \rangle$, with oscillations between 0.2 and 0.8. Even though it is not possible to break a continuous symmetry in one or two dimensions due to the Mermin-Wagner theorem [132], it is possible to break a discrete symmetry in 1D. Thus true CDW order is possible in the eBHM, which is defined on a lattice, and is seen as an oscillation $A \cos(\pi x)$ with constant amplitude $A > 0$ for large enough distances x .

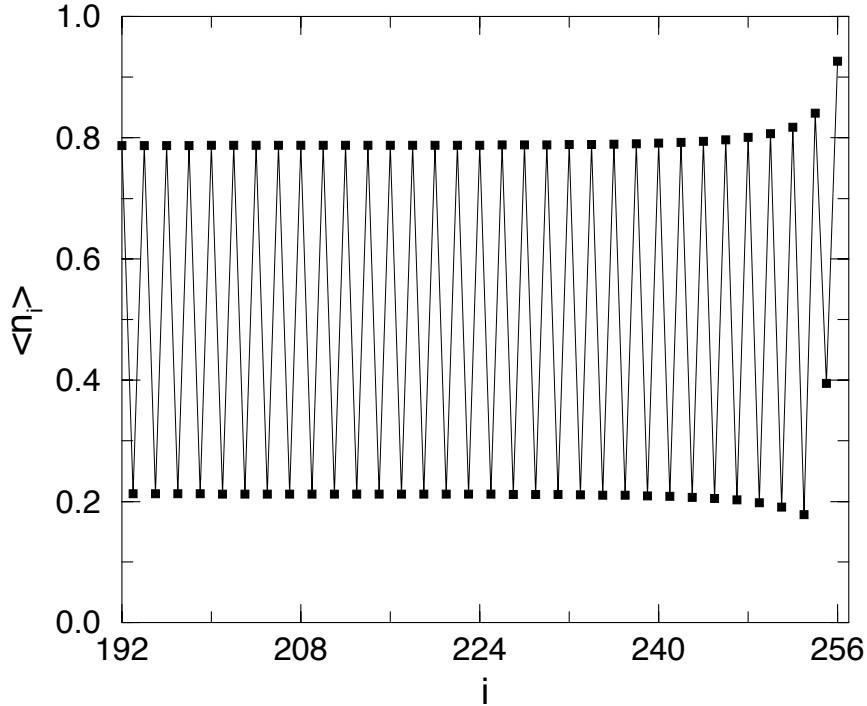


Figure 6.3: Local density fluctuations in the CDW phase reprinted from [122]. These fluctuations belong to the CDW lobe displayed in Figure 6.2 with half filling in a lattice with $L = 256, U = 1, t = 0.1$ and $V = 0.4$.

Figure 6.2(a) also displays another quantum phase, the HI. In spin systems a long range anti-ferromagnetic order can emerge. If that order has no characteristic momentum, the state is referred to as Haldane phase. Reminiscent of this phase it is possible for the intermediate regime with fixed integer filling, where the local density

is close to one, to introduce $\delta n_{b,i} = n_{b,i} - 1$ and the nonlocal string and parity order parameters:

$$\mathcal{O}_s(|i-j| \rightarrow \infty) = \langle \delta n_{b,i} e^{i\theta \sum_{k=1}^j n_{b,k}} n_{b,j} \rangle \quad (6.19)$$

$$\mathcal{O}_p(|i-j| \rightarrow \infty) = \langle e^{i\theta \sum_{k=1}^j n_{b,k}} \rangle. \quad (6.20)$$

\mathcal{O}_p is zero for the HI, whereas \mathcal{O}_s is finite [133]. However, this phase is only found for an average filling of one boson per lattice site in one dimension, and long range interactions are found to suppress this phase [134].

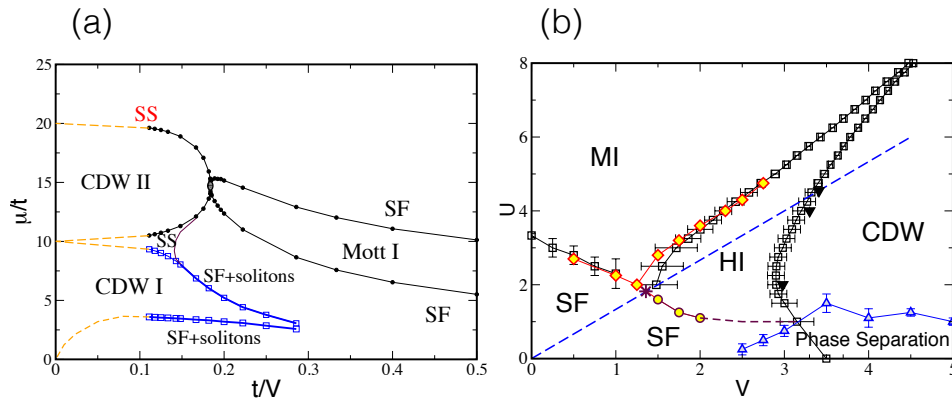


Figure 6.4: (a) $(\mu - t)$ phase diagram of the 1D eBHM for $U = 10t$ reprinted from [135]. In the large U, V regime a phase with both the typical density oscillations, found in a CDW, and additional SF is found. This coexistence phase is called supersolid (SS) and is for example found between the lobes of the CDW-I with half filling and CDW-II with integer bosonic filling. (b) $(U - V)$ phase diagram of the 1D eBHM at integer filling reprinted from [133]. DMRG results from [136], are combined with QMC results from [133]. Additionally to the previously established phases a PS regime is found by jumps in the mean density plotted versus μ .

A coexistence phase, called SS, was predicted in the mean field study for more than 2 dimensions [130]. A SS is a phase where interaction stabilized CDW and superfluidity coexist. Even though the SS phase was not found in the studies of the 1D eBHM, presented in Figure 6.2. However, later numerical studies demonstrated the existence of a SS phase in a parameter regime with large values of U and V . The respective phase diagram is shown in Figure 6.4(a)[135].

To finalize our discussion on the bosonic phases, we display the phase diagram, found by a recent MC study in Figure 6.4(b). The PS state consists of a mixture of two or more thermodynamic phases. It is thus not enough to simply look at the

averaged order parameters, as there might be contributions from all present phases. For Figure 6.4(b) the jumps in the density, plotted as a function of μ , were studied [133].

Even though it is possible to create two component mixtures of bosons, by trapping ^{87}Rb atoms in different Hyperfine states in a single lattice [137], and there are various other interesting variations of the BHM [30, 117, 138], we finish our discussion on purely bosonic Hubbard models here and move on to fermionic Hubbard models in the next section.

6.2 Fermionic Hubbard models

This section highlights some aspects of the Hubbard models, which describe trapped gases of interacting spin $\frac{1}{2}$ fermions. The original FHM was initially introduced in 1963 to describe fermions in solids [139]. The Hamiltonian with on site interactions reads as

$$H_{\text{FHM}} = -t_f \sum_{\langle i,j \rangle, \sigma} \hat{c}_{i,\sigma}^\dagger \hat{c}_{j,\sigma} + U_{FF} \sum_i \hat{n}_{i,\uparrow} \hat{n}_{i,\downarrow}. \quad (6.21)$$

It can be motivated for fermions in optical lattices in a similar fashion, as the Hamiltonian of the BHM [140]. The applicability was studied experimentally [141]. Here $\hat{c}_{i,\sigma}^\dagger$ and $\hat{c}_{j,\sigma}$ create or destroy a fermion at the respective lattice sites, and $\sigma = \{\uparrow, \downarrow\}$ indicates the spin of the fermion. $\hat{n}_{i,\sigma} = \hat{c}_{i,\sigma}^\dagger \hat{c}_{j,\sigma}$ is the fermionic occupation operator. The interaction U_{FF} is restricted to fermions on the same site with different spin.

Although there is no consensus concerning the mechanisms responsible for high- T_c superconductors, the FHM might eventually provide important insights to help in their understanding [142]. Analytically the model is only soluble in 1D with a Bethe ansatz [143], which is described in the book by Essler et al. [144]. Here it was shown, that at double half filling ($\langle n_\uparrow \rangle = \langle n_\downarrow \rangle = \frac{1}{2}$), the system always has a charge-excitation gap for any positive U_{FF} . For higher dimensional systems it is necessary to consult numerics or rely on approximations, but the model has attracted substantial interest [30, 145–148]. At zero temperature the parameters, characterizing the system, are the respective average densities $\langle n_\uparrow \rangle = \langle n_\downarrow \rangle$ and the ratio U_{FF}/t_f . For a detailed discussion on the effects of varying filling factors and finite temperature we refer the reader to the literature [28, 30, 128, 140]. In this work we restrict our discussion on the 1D ground state phase diagram of the extended Fermi-Hubbard model (eFHM) at half filling.

6.2.1 Extended Fermi-Hubbard model

To get some insight into some of the possible quantum phases, found in fermionic gases, trapped in optical lattices, we consider the eFHM. The Hamiltonian for this system is given by

$$H_{\text{eFHM}} = -t_f \sum_{\langle i,j \rangle, \sigma} \hat{c}_{i,\sigma}^\dagger \hat{c}_{j,\sigma} + U_{FF} \sum_i \hat{n}_{i,\uparrow} \hat{n}_{i,\downarrow} + V \sum_i \hat{n}_i \hat{n}_{i+1}. \quad (6.22)$$

The notation is the same as for the FHM, given in Equation 6.21, but with an additional interaction V between fermions on adjacent sites. $\hat{n}_i = \hat{n}_{i,\uparrow} + \hat{n}_{i,\downarrow}$ is the total fermionic density operator. This interaction is taking place between fermions irrespective of their spin polarization, and can be either positive or negative.

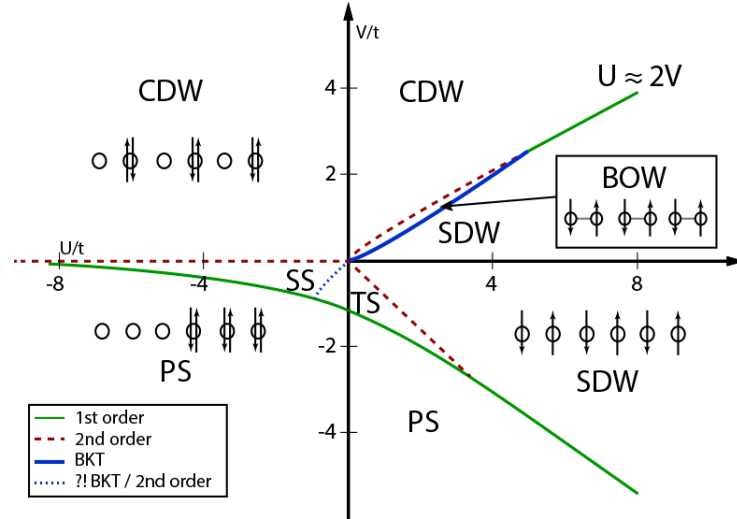


Figure 6.5: (a) $(U - V)$ phase diagram of the 1D eFHM at half filling reprinted from [149]. The energy scale is fixed by taking $t = 1$. The transition lines of the various stable phases together with a sketch of some phase are shown for positive and negative on site $U_{FF} = U$ and next neighbour interactions V . Note that in this figure "SS" denotes the singlet superconducting phase and not the supersolid phase introduced earlier. TS denotes the triplet superconducting state.

The 1D phase diagram for the half filling $\langle n_\uparrow \rangle = \langle n_\downarrow \rangle = \frac{1}{2}$ case is displayed in Figure 6.5 for finite $t = 1$. In the limit $V = 0$ the system trivially reproduces the FHM.

We first consider the regime, in which both interaction parameters are repulsive ($U_{FF}, V > 0$). In the strong coupling limit $U_{FF}, V \gg t$ the local density distribution depends on the rate $\frac{U_{FF}}{2V}$.

6.2 Fermionic Hubbard models

For $2V \gg U_{FF}$ the system will be in a CDW phase. Similar to the bosonic CDW phases, discussed in Subsection 6.1.2, the CDW phase has a broken discrete symmetry. Thus the phase is characterized by alternating, predominantly empty or doubly occupied lattice sites, where the double occupancy consist of a spin-up and a spin-down fermion. The order parameters, describing this system, are given by the connected density-density correlation $C^{CDW}(x) = \langle (n_\uparrow + n_\downarrow)(x)(n_\uparrow + n_\downarrow)(0) \rangle - 1$ and the respective structure factor $S^{CDW}(k) = \sum_j e^{ikj} C^{CDW}(j)$ at $k = \pi$. The oscillations of $C^{CDW}(x)$ are described by $C \cos(\pi x)$ for large x and a constant amplitude $C > 0$, which is dependent on U and V .

In the contrary case $2V \ll U_{FF}$ the system is predominantly singly occupied, and virtual hopping processes induce a quasi long-range SDW order, as depicted in the phase diagram. The spin spin correlation function is decaying algebraically. For our simulations later on we measure the connected density-density correlation function in the spin channel $C^{SDW}(x) = \frac{1}{4} \langle (n_\uparrow - n_\downarrow)(x)(n_\uparrow - n_\downarrow)(0) \rangle$ and the respective structure factor $S^{SDW}(k) = \sum_j e^{ikj} C^{SDW}(j)$.

For intermediate values of U_{FF}, V , QMC showed the phase boundary between these two phases to be slightly shifted away from $2V = U_{FF}$ towards smaller values of U_{FF} [150]. Furthermore for small to intermediate interactions, Nakamura suggested the existence of a new phase, initially called the bond charge density wave, situated in a narrow strip between the CDW and SDW regime [151, 152]. This phase, later commonly referred to as bond order wave (BOW) phase was controversially discussed [153–157]. The phase is characterized by true long range order with a staggered modulation of the kinetic energy density. It can be characterized with the kinetic energy operators $\hat{k}_i = \sum_\sigma (\hat{c}_{i+1,\sigma}^\dagger \hat{c}_{i,\sigma} + h.c.)$ and the respective structure factor $S^{BOW}(q) = \frac{1}{L} \sum_{j,k} e^{iq(j-k)} (\langle k_j k_k \rangle - \langle k_j^2 \rangle)$ [153].

For $U_{FF} < 0$ and $V > 0$ the system can always be characterized as a CDW.

For strong attractive couplings $U_{FF}, V < 0$ and $|U_{FF}|, |U_{FF}| \gg t$ the ground state becomes inhomogeneous with varying local occupancy in different spatial regions of the lattice. Reminiscent to the bosonic case this state is called PS phase. Still in the strong coupling limit, but now for repulsive U , the PS is transitioning into the SDW.

Finally for weak couplings there appear two metallic phases, where either singlet or triplet superconducting correlations dominate.

We complete our discussion on purely fermionic systems with the definition of the observables, used in our study, to probe the fermionic sector. The respective individual superfluid densities of the fermions, which are simulated as hard-core

bosons, are measured as

$$\rho_{s,\sigma} = \frac{L}{\beta} \langle W_{\sigma,x}^2 \rangle, \quad (6.23)$$

with the fermionic winding numbers $W_{\sigma,x}$. Additionally we measure the paired superfluid density (PSF) and the counter-rotating superfluid density (SCF), defined as

$$\rho_{\text{PSF}} = \frac{L}{\beta} \langle (W_{\uparrow,x} - W_{\downarrow,x})^2 \rangle, \quad (6.24)$$

$$\rho_{\text{SCF}} = \frac{L}{\beta} \langle (W_{\uparrow,x} + W_{\downarrow,x})^2 \rangle, \quad (6.25)$$

to probe for pairing correlations between the fermions [158]. As one dimensional systems can be characterized by the slowest decaying mode, we also measure the equal time Green's functions of the individual components and the 4-point correlation functions in the particle-hole and particle-particle channel as well. These are defined as

$$\mathcal{G}^\sigma(x) = \langle \hat{c}_\sigma^\dagger(x) \hat{c}_\sigma(0) + h.c. \rangle, \quad (6.26)$$

$$\mathcal{G}^{pp}(x) = \langle \hat{c}_\uparrow^\dagger(x) \hat{c}_\downarrow^\dagger(x) \hat{c}_\uparrow(0) \hat{c}_\downarrow(0) + h.c. \rangle, \quad (6.27)$$

$$\mathcal{G}^{ph}(x) = \langle \hat{c}_\uparrow^\dagger(x) \hat{c}_\downarrow(x) \hat{c}_\uparrow(0) \hat{c}_\downarrow^\dagger(0) + h.c. \rangle. \quad (6.28)$$

From the fermionic Green's function the momentum distribution can be obtained as Fourier transform $n^\sigma(k) = \sum_x e^{ikx} \mathcal{G}^\sigma(x)$.

6.3 Bose-Fermi-Hubbard models

In this section we introduce the models, which describe mixtures of bosonic and fermionic atoms, trapped in an optical lattice. Some aspects of the zero temperature ground state phase diagram for a mixture of identical fermions and scalar bosons are discussed in the first subsection. For this system the BFHM was introduced with on site interactions and next neighbour hoppings [111]. Subsection 6.3.2 introduces the sBFHM, whose ground state phase diagram is examined in this thesis at unit filling for the bosons and half filling in both fermionic components. We briefly describe, what is known about the model to date, before we continue with the discussion of our QMC algorithm in the next chapter.

6.3.1 Spin polarized Bose-Fermi-Hubbard model

With a single band approximation, as we have seen it in the previous sections, the BFHM was first derived for a mixture of neutral atoms, consisting of spin

polarized fermions and scalar bosons. When only contact interactions are present, the Hamiltonian, in lowest order, can be written as

$$H_{\text{BFH}} = -t_b \sum_{\langle i,j \rangle} \hat{b}_i^\dagger \hat{b}_j + \frac{U_{BB}}{2} \sum_i \hat{n}_i^b (\hat{n}_i^b - 1) - t_f \sum_{\langle i,j \rangle} \hat{c}_i^\dagger \hat{c}_j + U_{BF} \sum_i \hat{n}_i^b \hat{n}_i^f,$$

where U_{BF} is the on site interaction energy between a fermion and a boson on the same lattice site. The other parameters have been introduced in the previous section, but a precise definition in terms of the Wannier functions can be found in the derivation of Albus et al.[111]. For these mixtures new phases of matter are expected to be realizable by cold atom experiments [159].

For a system in infinite dimensions a generalized dynamical mean-field theory has been used to study the ground state phase diagram at half filling for both components [160]. For hard-core bosons, which are bosons with a maximal local occupation number of one, and spin polarized fermions an alternating MI with CDW order was found for $U_{BF} \gg t$ and a SS for $U_{BF} \ll t$. The existence of MI phases at non integer bosonic fillings was not observed in the purely bosonic BHM. When soft-core bosons are considered, the same phases can be found, but additionally a PS regime emerges, where the bosons and fermions occupy spatially distinct regions of the lattice.

Mixtures of spinless fermions and scalar bosons have been studied in 2D [161] and 3D optical lattices [162, 163]. Here we restrict our discussion on the ground state phase diagram of the 1D BFHM.

Figure 6.6 shows the phase diagram for a double half filled lattice with equal hopping of bosons and fermions $t_b = t_f = 1$, found by a QMC study [158]. The system can be characterized by the slowest decaying Green's function. Except for the fermionic Green's function $\mathcal{G}^f(x)$, defined in Equation 6.26, and the bosonic Green's function $\mathcal{G}^b(x)$, used in Equation 6.12, the composite pair Green's function has to be considered which can be written as

$$\mathcal{G}^{bf}(x) = \langle \hat{b}_\uparrow^\dagger(x) \hat{c}_\downarrow^\dagger(x) \hat{b}_\uparrow(0) \hat{c}_\downarrow(0) + h.c. \rangle. \quad (6.29)$$

The study found a crossover between two LL regimes, which are characterized by the decay of the measured Green's functions, as noted in the figure. For strong enough repulsion between the bosons and fermions a PS regime was found, with bosons and fermions predominantly occupying distinct spatial domains. In the pseudo SDW both individual Green's function decay exponentially, and only the composite $\mathcal{G}^{bf}(x)$ decays as power-law.

The case of different masses of bosons and fermions has been investigated as well. Such a mass imbalance can lead to unequal hopping amplitudes $t_b \neq t_f$ [164]. In the

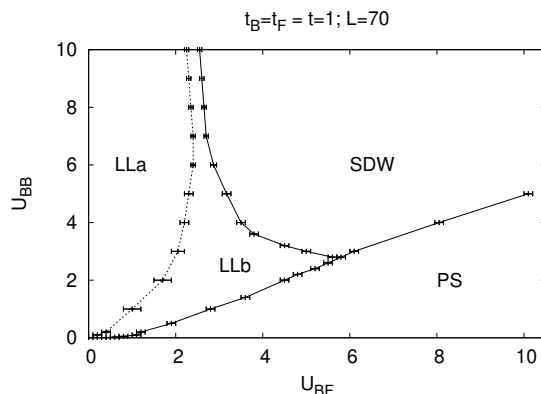


Figure 6.6: $(U_{BF} - U_{BB})$ phase diagram of the 1D BFHM at double half filling reprinted from [158]. The energy scale for the equal hopping case is fixed by taking $t_b = t_f = 1$. A first order transition to the PS regime is found. In the regions, indicated as LLa and LLb, the system consists of a composition of two weakly interacting LLs. In LLa $\mathcal{G}^f(x)$ decays slower than the composite $\mathcal{G}^{bf}(x)$, whereas in LLb $\mathcal{G}^f(x)$ decays faster. In both LL regimes $\mathcal{G}^b(x)$ has the slowest decay. The 'pseudo' SDW is associated with an assignment of a pseudo spin 'up' to the bosons and 'down' to the fermions.

heavy-fermion limit small fermionic hoppings allow for an effective mapping to a disordered BHM with site dependent chemical potential, caused by the presence or absence of fermions. This has been investigated by a strong coupling expansion with support of a numerical DMRG study [114]. The ground state phase diagram for the anisotropic hoppings $t_f = 4$ and $t_b = 1$ has been investigated by a QMC study as well, and found an Neel (Ising) state with true long range order in addition to the phases reported in Figure 6.6 [158].

In experiments mixtures of fermionic ^{40}K and bosonic ^{87}Rb atoms have been realized in a 3D optical lattice [106, 165]. These experiments report a strong decrease in bosonic visibility, if the bosons interact with the fermions, which is in contrast to low temperature calculations and has been attributed to an increase in temperature in the presence of trapping potentials [166].

Even though the induced interactions between fermions and bosons have been studied intensively, for example by bosonization [112, 167], they lack a full analytical description. In this work we address the question, which interactions can be induced between fermions from their interaction with either SF or MI bosonic background. Therefore we introduce the sBFHM in the next subsection.

6.3.2 Spinful Bose-Fermi-Hubbard model

For the Hamiltonian in the BFHM the fermions were identical, e.g. by keeping only one spin polarization. In our work we consider the sBFHM, which also describes a mixture of bosonic and spin- $\frac{1}{2}$ fermionic atoms. As there are two spin components, they can either attract or repel each other, if occupying the same lattice site. Thus the Hamiltonian is given by

$$\begin{aligned}
 H_{\text{sBFH}} = & -t_b \sum_{\langle i,j \rangle} \hat{b}_i^\dagger \hat{b}_j + \frac{U_{BB}}{2} \sum_i \hat{n}_i^b (\hat{n}_i^b - 1) - t_f \sum_{\langle i,j \rangle, \sigma} \hat{c}_{i,\sigma}^\dagger \hat{c}_{j,\sigma} \\
 & + U_{FF} \sum_i \hat{n}_{i,\uparrow}^f \hat{n}_{i,\downarrow}^f + U_{BF} \sum_i \hat{n}_i^b \hat{n}_i^f.
 \end{aligned} \tag{6.30}$$

The system is subject to the two hopping amplitudes t_b and t_f , the two intraspecies interaction parameters U_{BB} and U_{FF} , the interspecies coupling U_{BF} and the respective filling factors of the individual components as well.

The sBFHM was studied within a mean field approach [168]. In this work multiple combinations of SF, MI and CDW phases in the individual components were found. Numerical evidence of SS, CDW and SF phases was found for 3D systems within a dynamical mean-field theory (DMFT) calculation [169].

For a 1D system bosonization predicts an even richer phase diagram compared to the case of spinless fermions, including a SDW, CDW, a Wigner crystal phase, singlet and triplet paired states of fermions and a PS regime [112, 167]. In the same work the renormalization group equations for the model were derived.

Numerically the one dimensional case has been studied with the restriction of a maximum bosonic occupation number of 1, thus hard-core bosons, in combination with spin- $\frac{1}{2}$ fermions with DMRG. Here the MI and SF phases have been reported at some fixed interaction strengths for varied chemical potential [170]. The large local Hilbertspace seems to pose a challenge to state of the art DMRG simulations. We therefore investigate the system with a QMC simulation, described in the next chapter. We study the mutual influence on the intraspecies coupling constants, caused by the interaction between bosons and fermions. The bare fermionic interaction is set to $U_{FF} = 0$, and the system is considered at unit filling for the bosons, to allow for both SF and MI bosonic backgrounds, and half filling for each fermionic component.

Chapter 7

Path integral Monte Carlo method

Albeit the MC scheme introduced in Chapter 4 is widely used, it can not directly be used for the calculation of the quantum mechanical partition function. The problem is the lack of knowledge about the eigenstates and eigenenergies of the system. For a statistical evaluation based on a Markov chain it is thus necessary to find a representation of the partition function, which allows for an assignment of weights to each configuration. This chapter first introduces the required basis set at the example of an exact diagonalization (ED) algorithm, which was used for benchmarking purposes of our worm algorithm. The application of the worm algorithm is necessary, as ED is restricted to very small system sizes, due to the large local Hilbert space of the model. Then Section 7.2 introduces the path integral formalism, which is used for an accessible representation of the quantum mechanical partition function. Section 7.3 reviews the bosonic worm algorithm based on a world line representation as discussed in the paper by Pollet et al. [171]. How the different observables are measured in the algorithm is showcased in Section 7.4. The chapter concludes with a presentation on how the algorithm can be adapted to multiple components and two worms, which move synchronously in the respective extended configuration space.

7.1 Exact diagonalization as benchmark method

The noninteracting case ($U_{BF} = 0$) of the sBFHM is physically equivalent to a bosonic gas, accurately described by the BHM Hamiltonian, given in Equation 6.9, and spinful free fermions combined in one optical lattice. Thus the MI-SF transition discussed in Subsection 6.1.1 should be reproducible as the ($U_{BF} = 0$) case of our sBFHM. To be able to verify the results of our worm algorithm beyond the noninteracting case, we use the Lanczos method, which is an exact diagonalization technique, calculating a few extremal many-body eigenstates like the ground state and

the low energy spectrum.

Instead of addressing the methodical details of the Lanczos method, which can be found in numerous reviews [172, 173], or the technical details of our implementation, which are discussed in [174], in this work we restrict our discussion to the general perspective of how thermal expectation values for observables are calculated within the method.

As outlined in the previous chapter characterizing the various possible quantum phases in ultracold quantum gases in optical lattices requires to evaluate several carefully chosen observables. In contrast to Equation 4.8, which defines the thermal expectation value of an observable for a classical system in quantum mechanical systems, we typically do not know the eigenstates with their corresponding eigenenergies a priori. As an arbitrary basis will result in a nondiagonal matrix representation of the hamiltonian the formal definition of the thermal expectation value for an operator \hat{O}

$$\langle \hat{O} \rangle = \frac{1}{Z} \text{tr}[\hat{O} e^{-\beta \hat{H}}] \quad (7.1)$$

is not directly evaluable. In the above equation β is the inverse temperature and Z is the partition function of the system with hamiltonian \hat{H} defined as

$$\langle \hat{Z} \rangle = \text{tr}[e^{-\beta \hat{H}}]. \quad (7.2)$$

At the low temperatures (large β), which are present in ultracold atomic systems, the term $e^{-\beta \hat{H}}$ in Equation 7.1 will exponentially suppress contributions of excited eigenstates to $\langle \hat{O} \rangle$. Thus a benchmark of the thermal expectation value obtained by the Lanczos method with our worm algorithm is possible.

The first step within any ED algorithm is choosing a suitable basis for the problem hamiltonian. As we consider the Hamiltonian given in Equation 6.30 the local Hilbert space of each lattice site i contains $4(n_{max} + 1)$ states of the form

$$|\psi_i\rangle = |n_{i,\downarrow}, n_{i,\uparrow}, n_{i,b}\rangle, \quad (7.3)$$

where $n_{i,\downarrow}, n_{i,\uparrow}, n_{i,b}$ are the respective occupation numbers of spin \downarrow, \uparrow fermions and soft core boson with $n_{i,b} \leq n_{max}$ being the maximal occupation number of bosons per lattice site. Each type of spin polarization of the fermions contributes an occupied or an empty state. The respective basis for the Hilbert space describing a finite system of linear length L will thus consist of $(4(n_{max} + 1))^L$ states of the form

$$|\phi_k\rangle \equiv |\psi_1, \psi_2, \dots, \psi_i, \dots, \psi_L\rangle \equiv |\psi_1\rangle \otimes |\psi_2\rangle \otimes \dots \otimes |\psi_i\rangle \otimes \dots \otimes |\psi_L\rangle. \quad (7.4)$$

These states are then labeled to define a normal order in the desired fashion with the indice k .

The matrix representation of the Hamilton operator with respect to this basis is then calculated for each matrix element H_{kl} as

$$H_{kl} = \langle \phi_k | \hat{H} | \phi_l \rangle. \quad (7.5)$$

The resulting Hamiltonian matrix is not diagonal, as the basis we have chosen is not the respective eigenspectrum. In contrast to the full ED, which diagonalizes the complete matrix, the Lanczos method is an iterative method approximating a set of extremal eigenstates and eigenvalues. The computational effort is drastically reduced compared to a complete ED, as the approximation converges towards the true extremal eigenstates and eigenvalues within a few iterations. For the execution of the Lanczos algorithm we used the ARPACK library [175] within the SciPy implementation [176] using the "Implicitly Restarted Lanczos Method".

The result of the Lanczos method is a set of eigenvectors $\{|\alpha_n\rangle\}$ represented in the above basis with weights $c_{n,k}$ and the corresponding eigenenergies $\{E_n\}$

$$|\alpha_n\rangle = \sum_k c_{n,k} |\phi_k\rangle, \quad (7.6)$$

thus satisfying the stationary Schrödinger equation

$$\hat{H} |\alpha_n\rangle = E_n |\alpha_n\rangle. \quad (7.7)$$

Equation 7.1 is then easy to evaluate using the finite set of eigenstates $\{|\alpha_n\rangle\}$ with the respective energies $\{E_n\}$ and having the basis states $|\phi_k\rangle$ at hand with the trace running only over the finite set $\{|\alpha_n\rangle\}$. However, the method only is applicable for very small system sizes, as each element of the hamiltonian matrix H_{kl} has to be calculated. For system sizes up to $L = 6$ we get results within reasonable time with the Lanczos method. These approximate expectation values serve as benchmark for our QMC method, and the results are presented in Appendix C. In this chapter we now continue with the formalism of path integral necessary for the worm algorithm.

7.2 Path integral formulation

Although the goal of calculating thermal expectation values of physical observables is quite the same in QMC methods as in ED methods, the approach is completely different. As the eigenspectrum is not known, it is not a trivial task to assign physical

weights to certain states as done in Chapter 4 for classical MC methods. To avoid the diagonalization of the hamiltonian matrix the idea is thus to find an alternative representation, in which a weight can directly be assigned to each configuration and thus allowing an effective sampling through a Markov process. This is achieved by changing the perspective onto the quantum partition function given in Equation 7.2 towards a higher dimensional classical partition function within the path integral formulation of quantum mechanics [115].

The first step is a splitting of the hamiltonian \hat{H} into

$$\hat{H} = \hat{H}_0 + \hat{H}_I \quad (7.8)$$

with the diagonal part \hat{H}_0 and the nondiagonal part \hat{H}_I with respect to a given basis. The basis states are thus eigenstates of the diagonal part and satisfy the stationary Schrödinger equation $\hat{H}_0 |\phi\rangle = E_\phi |\phi\rangle$.

For the previously considered case of the occupation number basis, given in Equation 7.4, our Hamiltonian of interest consists of the parts

$$\hat{H}_0 = \frac{U_{BB}}{2} \sum_i \hat{n}_i^b (\hat{n}_i^b - 1) + U_{FF} \sum_i \hat{n}_{i,\uparrow}^f \hat{n}_{i,\downarrow}^f + U_{BF} \sum_{i,\sigma} \hat{n}_i^b (\hat{n}_{i,\uparrow}^f + \hat{n}_{i,\downarrow}^f) \quad (7.9)$$

$$\hat{H}_I = -t_b \sum_{\langle i,j \rangle} \hat{b}_i^\dagger \hat{b}_j - t_f \sum_{\langle i,j \rangle, \sigma} \hat{c}_{i,\sigma}^\dagger \hat{c}_{j,\sigma} \quad (7.10)$$

with \hat{H}_0 representing the potential energy and \hat{H}_I the kinetic energy. With the above introduced interaction picture the exponential factor $e^{-\beta\hat{H}}$ in the partition function can be rewritten as

$$e^{-\beta\hat{H}} = e^{-\beta\hat{H}_0} \hat{\mathcal{U}}(\beta, 0), \quad (7.11)$$

with the evolution operator defined as

$$\hat{\mathcal{U}}(\beta, 0) = e^{-\int_0^\beta dt \hat{H}_I(t)}. \quad (7.12)$$

The time dependent interaction is defined as $\hat{H}_I(t) = e^{-t\hat{H}_0} \hat{H}_I e^{t\hat{H}_0}$. With this expansion we write the quantum partition function given in Equation 7.2 in the path integral formalism

$$Z = \text{tr} \sum_{n=0}^{\infty} \int_0^\beta dt_n \int_0^{t_n} dt_{n-1} \dots \int_0^{t_2} dt_1 e^{-t_1 \hat{H}_0} \hat{H}_I e^{-(t_2-t_1) \hat{H}_0} \dots \dots e^{-(t_n-t_{n-1}) t \hat{H}_0} \hat{H}_I e^{-(\beta-t_n) \hat{H}_0}, \quad (7.13)$$

where the times $t_1 < \dots < t_n$ are ordered through the integrals.

7.2 Path integral formulation

In general QMC methods are sampling configurations locally within the representation in Equation 7.13 and assign a weight to each such configuration. The worm algorithm, used for our work, was first introduced by Prokof'ev et al. in 1998 [177]. In contrast to other methods it does not directly change configurations in the partition function, defined in Equation 7.13, but is using the extended Green's function sector

$$Z_e = \text{tr} \left[\mathcal{T} \left(\left(\hat{b}_i(t_0) \hat{b}_j^\dagger(\tau) + h.c. \right) e^{-\beta \hat{H}} \right) \right]. \quad (7.14)$$

where \mathcal{T} denotes the time ordering. The operators $\left(\hat{b}_i(t_0) \hat{b}_j^\dagger(\tau) + h.c. \right)$ are called the worm operators and correspond to creation and annihilation operators at times t_0 and τ . Even though a reasonable estimation of physical expectation values relies on configurations, which belong to the normal partition function, the extended partition function enables a more efficient sampling of those configurations by adding the additional worm operators to the system and thereby introducing additional degrees of freedom in changing the configurations. Our algorithm is based on the locally optimal implementation, discussed in the work by Pollet et al. [171] and allows for multiple worm operators in the system.

Let us now derive the necessary weights associated with a partition sum configuration and derive the graphical representation for a more intuitive understanding of the operators. Comparing Equation 7.14 to Equation 7.2 reveals that for a representation similar to Equation 7.13 for the extended partition function we need to insert the worm operators at the correct positions according to their time dependency $\hat{b}_i(t_0) = e^{-t_0 \hat{H}_0} \hat{b}_i e^{t_0 \hat{H}_0}$ and $\hat{b}_j^\dagger(\tau) = e^{-\tau \hat{H}_0} \hat{b}_j^\dagger e^{\tau \hat{H}_0}$. Furthermore the extended partition sum requires a summation over all possible permutations of lattice sites i, j and times t_0, τ . Thus we need to incorporate

$$\sum_{i,j,t_0,\tau} \dots e^{-t_0 \hat{H}_0} \hat{b}_i e^{t_0 \hat{H}_0} \dots e^{-\tau \hat{H}_0} \hat{b}_j^\dagger e^{\tau \hat{H}_0} \dots \quad (7.15)$$

into Equation 7.13. To evaluate the operators and obtain scalar weights complete sets of basis states

$$\mathbb{1} = \sum_{\phi_k} |\phi_k\rangle\langle\phi_k| \quad (7.16)$$

from the occupation number basis are inserted between any occurrence of operators. As \hat{H}_0 is diagonal by construction in this basis the exponential functions are easily evaluated through the stationary Schrödinger equation, and the extended partition

function can be evaluated as

$$\begin{aligned}
 Z_e = \sum_{n=2}^{\infty} \sum_{\{\phi_1, \dots, \phi_n\}} \sum_{i,j} \int_0^{\beta} dt_n \int_0^{t_n} dt_{n-1} \dots \int_0^{t_2} dt_1 \langle \phi_1 | \hat{H}_I | \phi_2 \rangle \\
 e^{-(t_2-t_1)E_{\phi_2}} \langle \phi_2 | \hat{H}_I | \phi_3 \rangle e^{-(t_3-t_2)E_{\phi_3}} \dots \\
 \dots e^{-(t_k-t_{k-1})E_{\phi_k}} \langle \phi_k | \hat{b}_i | \phi_{k+1} \rangle e^{(t_{k+1}-t_k)E_{\phi_{k+1}}} \dots \\
 \dots e^{-(t_l-t_{l-1})E_{\phi_l}} \langle \phi_l | \hat{b}_j^\dagger | \phi_{l+1} \rangle e^{(t_{l+1}-t_l)E_{\phi_{l+1}}} \dots \\
 \dots e^{-(t_n-t_{n-1})E_{\phi_n}} \langle \phi_n | \hat{H}_I | \phi_1 \rangle e^{-(\beta+t_1-t_n)E_{\phi_1}}.
 \end{aligned} \tag{7.17}$$

Here the expansion order starts at $n = 2$ in contrast to $n = 0$ due to the worm operators, which we have to integrate over and treat on equal terms as the times of the interactions as $t_0 = t_k$ and $\tau = t_l$. This partition function is now accessible to a Markov process relying on weights of configurations \vec{x} . All terms apart from the summations and integrals in Equation 7.17 are considered as positive weights

$$\begin{aligned}
 W(\vec{x}) = W(n, t_1, \dots, t_n, i, j, \{|\phi_i\rangle\}) \\
 = \langle \phi_1 | \hat{H}_I | \phi_2 \rangle e^{-(t_2-t_1)E_{\phi_2}} \langle \phi_2 | \hat{H}_I | \phi_3 \rangle e^{-(t_3-t_2)E_{\phi_3}} \dots \\
 \dots e^{-(t_k-t_{k-1})E_{\phi_k}} \langle \phi_k | \hat{b}_i | \phi_{k+1} \rangle e^{(t_{k+1}-t_k)E_{\phi_{k+1}}} \dots \\
 \dots e^{-(t_l-t_{l-1})E_{\phi_l}} \langle \phi_l | \hat{b}_j^\dagger | \phi_{l+1} \rangle e^{(t_{l+1}-t_l)E_{\phi_{l+1}}} \dots \\
 \dots e^{-(t_n-t_{n-1})E_{\phi_n}} \langle \phi_n | \hat{H}_I | \phi_1 \rangle e^{-(\beta+t_1-t_n)E_{\phi_1}}.
 \end{aligned} \tag{7.18}$$

Thus a configuration is characterized by its order of expansion n , the associated times of the operators t_1, \dots, t_n , the corresponding sites i, j of the worm operators and the basis states $\{|\phi_i\rangle\}$ between the operators. Considering the sums and integrations as integration over all these configurations

$$\int_{\mathcal{C}} dx = \sum_{n=2}^{\infty} \sum_{\{\phi_1, \dots, \phi_n\}} \sum_{i,j} \int_0^{\beta} dt_n \int_0^{t_n} dt_{n-1} \dots \int_0^{t_2} dt_1 \tag{7.19}$$

we end up with

$$Z_e = \int_{\mathcal{C}} dx W(\vec{x}), \tag{7.20}$$

which is an integral in the shape as considered in our discussion of classical MC methods in Equation 4.14.

Let us now introduce the graphical representation of an exemplary configuration in Figure 7.1, which will be useful in the next section, where we discuss the individual updates, contained in the worm algorithm, to enable a sampling across all

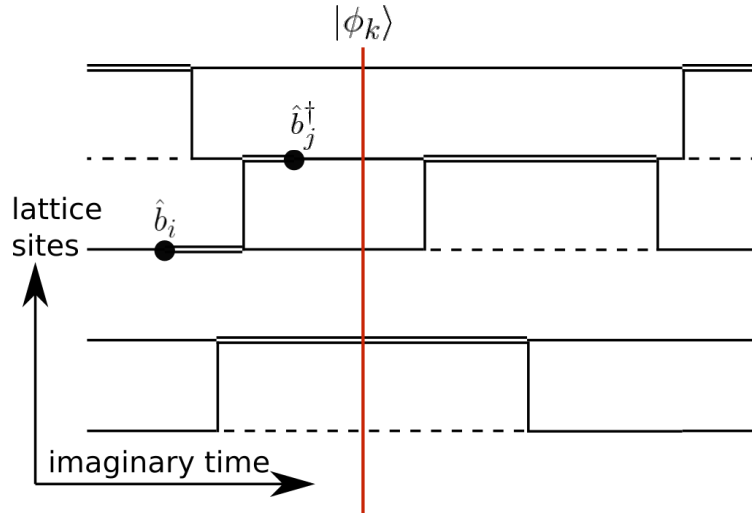


Figure 7.1: Graphical representation of a configuration in the Green's function sector. The imaginary time evolves from left $t = 0$ to right $t = \beta$. Real space lattice sites are displayed as horizontal lines. The type of the line denotes the occupation of a lattice site at the respective imaginary time. A dashed line denotes that the site is empty, single lines denote that the site is occupied by one boson, double lines denote double occupancy and so on. Black vertical lines correspond to next neighbour hopping elements. The two black circles represent the worm operators, which create and annihilate a particle. At each timestep, here visualized as vertical red line, it is possible to assign a Fock state. In this example the basis state at the red line is $|\phi_k\rangle = |11120\rangle$.

configurations \vec{x} . Each horizontal line represents a lattice site, with its occupancy represented by the linestyle. Black lines in the figures notation correspond to soft-core bosons, and vertical lines between two lattice sites denote a hopping of a single boson from one site to the neighbouring site.

7.3 Bosonic worm algorithm

In this section the general update structure for bosonic configurations, as depicted in Figure 7.1, is introduced. This type of worm algorithm [171] is able to simulate a wide range of interaction parameters in models like the BHM and detect phase transitions, as the SF-MI transition, discussed in Subsection 6.1.1. The adaption to hard-core bosons and multiple components will be subject of Section 7.5.

The fundamental idea of the worm algorithm is to connect two configurations, belonging to the partition function in Equation 7.13, by entering the regime of

the extended partition function given in Equation 7.17. A configuration in Z is called diagonal, and those belonging to Z_e nondiagonal. Starting at one diagonal configuration the second diagonal configuration is created by inserting a pair of worm operators, and moving one of those operators (annihilation or creation operator) through the system, taking the physical weights into account until both operators are residing on the same lattice site and imaginary time again. Once reconnected, the operators are taken out of the system with the respective probability. Such a process is presented in Figure 7.2.

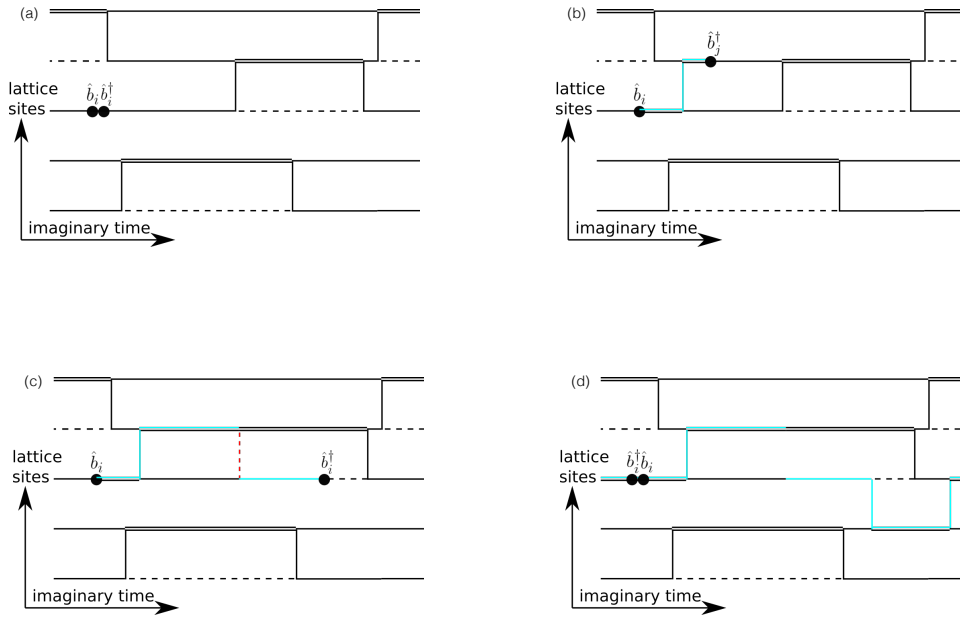


Figure 7.2: Illustration of a possible transition from a diagonal to another diagonal configuration. (a) **Configuration after the update *Insertworm*.** Into a diagonal configuration a pair of worm operators is inserted with $\hat{b}_i^\dagger(t_0)$ being the head of the worm. (b) **Updates *Move - Insertkink - Move* are applied.** The first *Move* update changes the imaginary time of the worm head to $t_0 + \tau$, adding an additional particle, marked by the cyan line along its path. At this time the worm head hops to site j , which introduces a kink (hopping element represented by a vertical cyan line here for illustrative purposes, normally it would be black). Then it moves in imaginary time again. (c) **Updates *Move - Deletekink - Move* are applied.** The first movement is stopping at a kink connecting j and i . The worm head deletes the kink by transitioning to site i and continues its movement there. (d) **The updates *Insertkink - Move - Insertkink - Move* connect the worm operators again.** As with the previous updates the worm continues its path through the system, until reaching the worm tail. When the worm head and tail are connected, they are allowed to be taken out of the system to end up with the new diagonal configuration.

The crucial part is that the update chain presented in Figure 7.2 can be split into individual updates with easily accessible acceptance ratios. Every update step is done locally and in an optimal way, to ensure an efficient transitioning between diagonal configurations. The individual allowed updates are thus quite simple and can be summarized as:

Insertworm

Inserting a pair of creation and annihilation Heisenberg operators, e.g.

$\hat{b}_i(t_0)\hat{b}_i^\dagger(t_0)$ into the current diagonal configuration, choosing a site i and a time t_0 at random.

Move

Move the worm operator, which is chosen to be the head, e.g. $\hat{b}_i(t_0)$ by a finite distance τ in beta. So it changes to $\hat{b}_i(t_0 + \tau)$.

Insertkink

Assuming the head is at imaginary time t_i without an interaction, it can insert a kink by hopping to a neighbouring site and continue from there.

Deletekink

Assuming the head is at imaginary time t_i with an interaction. it can remove it by following the kink to the neighbouring site and continue from there.

Glueworm

If the tail and the head are next to each other in imaginary time and both on the same lattice site i , they can be removed from the system.

Ergodicity is satisfied by the above set of updates, as the head can explore through the entire extended configuration space. Then acceptance ratios are chosen according to Equation 4.23 from the Metropolis algorithm to satisfy equal balance in each step. Thus we are sampling the extended partition function Z_e correctly, allowing for the measurement of off-diagonal observables like the equal time Green's function. Simultaneously every time the update *Glueworm* is accepted, a sample for Z is generated, which allows the calculation of diagonal physical observables, as discussed in Section 7.4. The updates with their respective acceptance ratios are discussed in more detail in the subsequent subsections.

7.3.1 Insertworm and Glueworm

As discussed in the previous section, the first step of the worm algorithm, starting from a diagonal configuration, is always to insert a pair of creation and annihilation operators $\hat{b}_i(t_0)\hat{b}_i^\dagger(t_0)$ into the current diagonal configurations. The insertion is called *Insertworm*. The *Insertworm* update in combination with the *Glueworm* update, which takes the worm operator pair out of the system, thus connect the partition functions Z and Z_e .

The reason the worm algorithm is able to efficiently sample configurations is that all the individual updates are only performing local changes to the current

configuration. Thus the weights $W(\vec{x})$ and $W(\vec{y})$ present in Equation 4.23 for the acceptance ratio do not have to be evaluated separately each time, but only the affected part, changed during an update, has to be considered as only the relative weight $\frac{W(\vec{y})}{W(\vec{x})}$ enters Equation 4.23. All unaffected parts of the configurations, contributing to the weights, will cancel.

Let us take a closer look at the example, shown in Figure 7.2(a), where a worm is inserted into the configuration on a lattice site, occupied by a single boson. In Figure 7.3 only the relevant area is shown, and in the following discussions we will denote only the relevant contributions, changed during an update by $W(\vec{y})$ and $W(\vec{x})$.

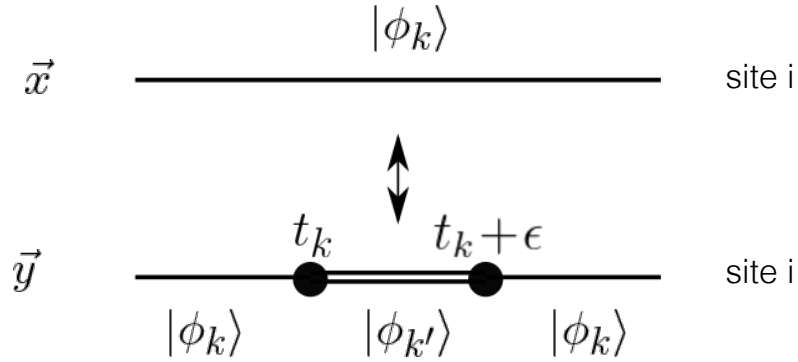


Figure 7.3: Graphical representation of the *Insertworm* update. A worm is inserted on lattice site i at time t_0 . As the density between the worm operators is increased by one in \vec{y} relative to \vec{x} , the left black circle is a \hat{b}_i operator, and the right circle the \hat{b}_i^\dagger operator. In configuration \vec{x} the state $|\phi_k\rangle$ is present at the time t_0 . In configuration \vec{y} the same state is still present at times $t < t_0$ (left of \hat{b}_i) and times $t > t_0 + \epsilon$ (right of \hat{b}_i^\dagger), but in between the two operators the state is changed to $|\phi_{k'}\rangle$.

In the notation of Figure 7.3 the respective weights are given by:

$$W(\vec{x}) = C_Z \quad (7.21)$$

$$W(\vec{y}) = \langle \phi_k | \hat{b}_i | \phi_{k'} \rangle \langle \phi_{k'} | \hat{b}_i^\dagger | \phi_k \rangle, \quad (7.22)$$

where C_Z is the relative weight between the sectors of Z and Z_e . The matrix elements of the operators are set to unity instead of the physical $(n_i + 1)$, and therefore the Green's function sector has to be reweighted.

For an optimal choice let us first consider the proposal procedure of the update. In our classical MC algorithms in each algorithmic timestep it is predetermined, what

the next update will be. In the worm algorithm the situation is slightly different, as the choice of the next update depends on the current state of the configuration. This partially probabilistic choice has to be taken into account in determining the acceptance ratios. Thus we can split up the proposal probability as

$$P(x \rightarrow y) = P_{alg}(Update) \cdot P_{Update}(\vec{x} \rightarrow \vec{y}). \quad (7.23)$$

where $P_{alg}(Update)$ is the probability to choose a certain update type, and $P_{Update}(\vec{x} \rightarrow \vec{y})$ is the probability to produce configuration \vec{y} from configuration \vec{x} with this chosen update.

For a diagonal configuration the only possible option is to insert a worm and for a diagonal worm we never insert a worm. Thus the probabilities are given by

$$\{P_{alg}(Insertworm) = 1 \mid x \in Z\} \quad (7.24)$$

$$\{P_{alg}(Insertworm) = 0 \mid x \in Z_e\}. \quad (7.25)$$

The worm algorithm chooses a random time t_k uniformly between 0 and β and one lattice site i out of the L lattice sites at random for the insertion location. Similar to the Lanczos method there is the notion of a maximal occupancy of each lattice site n_{max} . However, this number is not restricted to very small numbers as in DMRG or ED methods. If $|\phi_k\rangle$ has 1 to n_{max} bosons residing on lattice site i , the worm can increase or decrease the occupation number in between the worm operators, thereby fixing their relative orientation. If no boson is present or the upper bound is already met, there is only one physically valid option to insert the worm. Thus the probability of orientation and thereby annihilating (an) or creating (cr) a particle can be given by:

$$P_{rising}(an) = \frac{1 - \delta_{n_i, n_{max}}}{2} \quad P_{rising}(cr) = \frac{1 - \delta_{n_i, 0}}{2}, \quad (7.26)$$

Although we only depicted movements in positive imaginary time in Figure 7.2, a movement in the opposite direction would be equally valid at any time. Thus it is possible to choose either one of the two worm operators as the moving head during an *Insertworm* update with equal probability $P_{dir}(\rightarrow) = P_{dir}(\leftarrow) = \frac{1}{2}$. The resulting update probability for the *Insertworm* update can then be written as

$$P_{Insertworm}(\vec{x} \rightarrow \vec{y}) = \frac{1}{\beta} \frac{1}{L} P_{rising}(worm) P_{dir}(worm), \quad (7.27)$$

For the inverse Glueworm update, which is changing a nondiagonal configuration to a diagonal configuration, we can only propose to remove the worm, if possible, which leads to

$$P_{Glueworm}(\vec{y} \rightarrow \vec{x}) = 1. \quad (7.28)$$

Using Equation 4.23 with the respective probabilities and weights the acceptance ratios for the above updates reduce to

$$q_{\text{Insertworm}} = \frac{4\beta L}{C_Z} P_{\text{alg}}(\text{Glueworm}) \quad (7.29)$$

and

$$q_{\text{Glueworm}} = \frac{1}{q_{\text{Insertworm}}}. \quad (7.30)$$

7.3.2 Moveworm

Once there is a worm present in the system, the worm head transitions through the configuration. Changes in imaginary time of the worm operators are done by the *Moveworm* update. Figure 7.4 displays such a move on lattice site j .

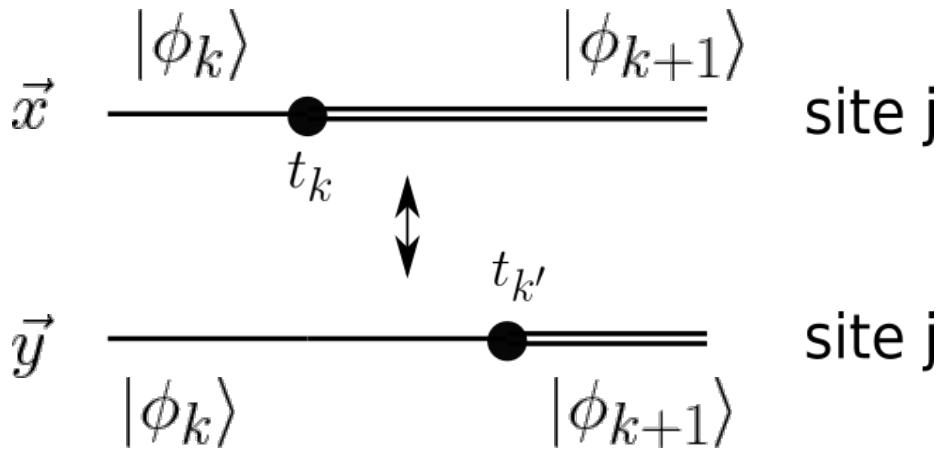


Figure 7.4: Graphical representation of the *Moveworm* update. The worm head operator is changing its imaginary time from t_k to $t_{k'}$, affecting occupation on its current lattice site. All other lattice sites are not affected by the update. The length of the covered distance is denoted by $\tau = t_{k'} - t_k$.

The varied contributions to the weights of the two configurations are

$$W(\vec{x}) = e^{-t_k E_{\phi_k}} \langle \phi_k | \hat{b}_j | \phi_{k+1} \rangle e^{t_k E_{\phi_{k+1}}} \quad (7.31)$$

$$W(\vec{y}) = e^{-t_{k'} E_{\phi_k}} \langle \phi_k | \hat{b}_j | \phi_{k+1} \rangle e^{t_{k'} E_{\phi_{k+1}}}. \quad (7.32)$$

In the proposal of the new configuration it is possible to move the worm head in either direction, and we choose them with equal probability $P_{dir}(\rightarrow) = P_{dir}(\leftarrow) = \frac{1}{2}$. Thus the *Moveworm* update is reversed by itself with opposite movement direction and same proposal of τ . All contributions to the acceptance ratio thus can be written as

$$q_{Moveworm}(\vec{x} \rightarrow \vec{y}) = \frac{e^{-t_{k'} E_{\phi_k}} \langle \phi_k | \hat{b}_j | \phi_{k+1} \rangle e^{t_{k'} E_{\phi_{k+1}}} P_{alg}(Moveworm) P_{dir}(\leftarrow) P_{Moveworm}(\vec{y} \rightarrow \vec{x})}{e^{-t_k E_{\phi_k}} \langle \phi_k | \hat{b}_j | \phi_{k+1} \rangle e^{t_k E_{\phi_{k+1}}} P_{alg}(Moveworm) P_{dir}(\rightarrow) P_{Moveworm}(\vec{x} \rightarrow \vec{y})}. \quad (7.33)$$

Here we have chosen the example depicted in Figure 7.4, where the black circle corresponds to a \hat{b}_j operator, but as the term $\langle \phi_k | \hat{b}_j | \phi_{k+1} \rangle$ or the respective term with a creation operator is present in both the nominator and in the denominator, the acceptance ratio can always be reduced to

$$q_{Moveworm} = \frac{e^{-\tau E_{\phi_k}} P_{Moveworm}(\vec{y} \rightarrow \vec{x})}{e^{-\tau E_{\phi_{k+1}}} P_{Moveworm}(\vec{x} \rightarrow \vec{y})}. \quad (7.34)$$

It is possible to cancel the exponential prefactors by an elegant choice of the proposal functions, if we define their transition probabilities as

$$P_{Moveworm}(x \rightarrow y) d\tau = C_1 e^{-\tau E_{\phi_k}} d\tau \quad (7.35)$$

$$P_{Moveworm}(y \rightarrow x) d\tau = C_2 e^{-\tau E_{\phi_{k+1}}} d\tau \quad (7.36)$$

with C_1 and C_2 being constants, subject to the normalization equation $\int_0^\infty P_{Moveworm}(\vec{x} \rightarrow \vec{y}) d\tau = 1$.

In the unbound case, depicted in Figure 7.4, this results in $C_1 = E_{\phi_k}$ and $C_2 = E_{\phi_{k+1}}$ for the constants and the acceptance ratio

$$q_{Moveworm} = \frac{E_{\phi_{k+1}}}{E_{\phi_k}}. \quad (7.37)$$

The proposed timeshift, satisfying the above equation, can be generated from an uniform random number $r \in [0, 1[$ as $\tau = \frac{-\log r}{E_{\phi_k}}$.

However, there may be bound cases, where it is not possible to move the proposed distance τ in imaginary time. The energies in Equation 7.37 in principle are the

7.3 Bosonic worm algorithm

eigenenergies of the many body eigenstates $|\phi_k\rangle$ and $|\phi_{k+1}\rangle$, but as only relative energies matter, we will always only consider the local energy contributions

$$E_L = E_{\phi_k} - \min \{E_{\phi_k}, E_{\phi_{k+1}}\} + E_{off} \quad (7.38)$$

$$E_R = E_{\phi_{k+1}} - \min \{E_{\phi_k}, E_{\phi_{k+1}}\} + E_{off}, \quad (7.39)$$

which makes the evaluation of the acceptance rate much easier, as we do not have to calculate the energy of the complete system. The factor E_{off} is a positive energy offset to ensure ergodicity within the code and is discussed in more detail in [171].

From this argument it is obvious that the worm head has no problem with moving past a kink, present only on different sites, which is showcased in the second *Moveworm* update in Figure 7.2(c), due to the fact that the worm operator \hat{b}_i^\dagger commutes with every interaction term $\hat{b}_j^\dagger \hat{b}_k$, whose sites are different $i \neq j, k$, and thus the local energy is not changed.

Even though a worm operator \hat{b}_i^\dagger could pass certain kinks, present on its own current lattice site, as the corresponding commutator is zero ($[\hat{b}_i^\dagger, \hat{b}_i^\dagger \hat{b}_k] = 0$), the local energy would change. A worm movement in the algorithm therefore is always forced to stop at such an interaction.

There are four possible scenarios with different acceptance ratios, which are presented in Figure 7.5. The weights in all four cases are the same for nominator and denominator. Let us consider the example shown in Figure 7.5. Assume the worm head is moving to a time t_y , the transition probability density with a forced stop at $t_{k'}$ can be written as

$$P_{Moveworm}(\vec{x} \rightarrow \vec{y}) dt_y = \begin{cases} E_{\phi_k} e^{-(t_y - t_k) E_{\phi_k}} dt_y & t_y < t_{k'} \\ C \delta(t_y - t_{k'}) dt_y & t_y \geq t_{k'}, \end{cases} \quad (7.40)$$

with the constant C subject to the above mentioned normalization equation

$$\int_{t_k}^{\infty} P_{Moveworm}(\vec{x} \rightarrow \vec{y}) dt_y = \int_{t_k}^{t_{k'}} E_{\phi_k} e^{-(t_y - t_k) E_{\phi_k}} dt_y + \int_{t_{k'}}^{\infty} C \delta(t_y - t_{k'}) dt_y = 1, \quad (7.41)$$

resulting in $C = e^{-(t_{k'} - t_k) E_{\phi_k}}$. Thus inserting these transition probabilities in Equation 7.34, the acceptance ratio for this scenario is given by

$$q_{Moveworm} = \frac{E_{\phi_{k+1}}}{1}. \quad (7.42)$$

The acceptance ratios for all four scenarios are shown in Figure 7.5.

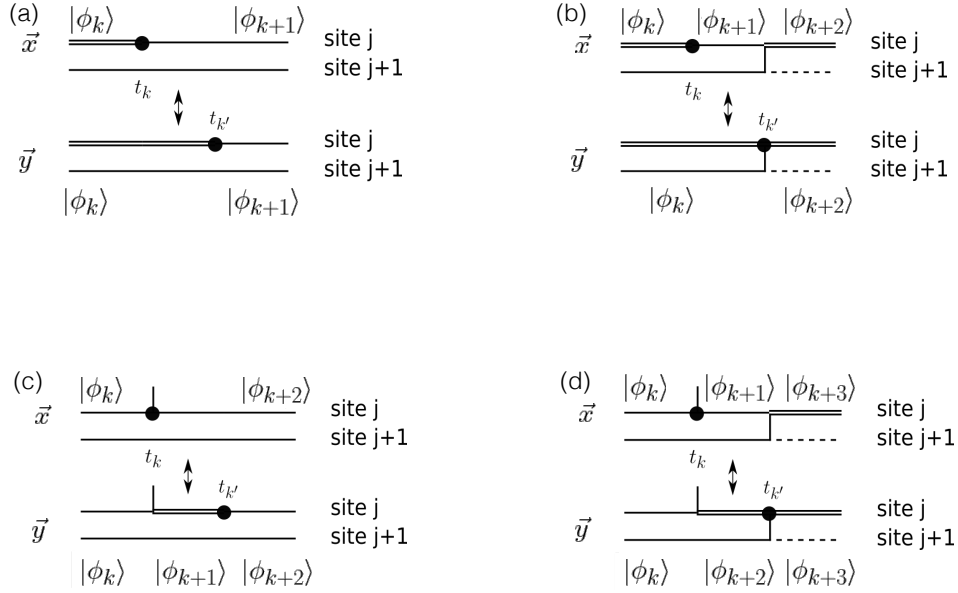


Figure 7.5: Different scenarios for the *Moveworm* update with their respective acceptance ratios. (a) **Starting free and ending free:** $q_{\text{Moveworm}} = \frac{E_{\phi_{k+1}}}{E_{\phi_k}}$ (b) **Starting free and ending at a kink:** $q_{\text{Moveworm}} = E_{\phi_{k+1}}$ (c) **Starting at a kink and ending free:** $q_{\text{Moveworm}} = \frac{1}{E_{\phi_{k+1}}}$ (d) **Starting and ending at a kink:** $q_{\text{Moveworm}} = 1$

7.3.3 Insertkink and Deletekink

The remaining updates are inserting and deleting kinks, and thereby moving the worm head to adjacent lattice sites. In Figure 7.6 an insertion of a kink is shown, starting from configuration \vec{x} . When the wormhead for whatever reason is at a kink on its lattice site, it is not possible to add another kink at the same imaginary time. The weights are given by

$$W(\vec{x}) = \langle \phi_k | \hat{b}_j^\dagger | \phi_{k+1} \rangle \quad (7.43)$$

$$W(\vec{y}) = \langle \phi_k | \hat{H}_I | \phi_{k'} \rangle \langle \phi_{k'} | \hat{b}_{j+1}^\dagger | \cdot \rangle \phi_{k+1} \quad (7.44)$$

In one dimension the proposal of an insertion has two available lattice sites, and for each of them either direction of movement on the new lattice site is possible for the worm head, which results in $P_{\text{Insertkink}}(\vec{x} \rightarrow \vec{y}) = \frac{1}{4}$. If a movement would create an unphysical state, the update is simply rejected and the algorithm continues.

Whenever a worm is residing at a kink, and the *Deletekink* update is chosen, there is no ambiguity, and the corresponding transition probability can be written as

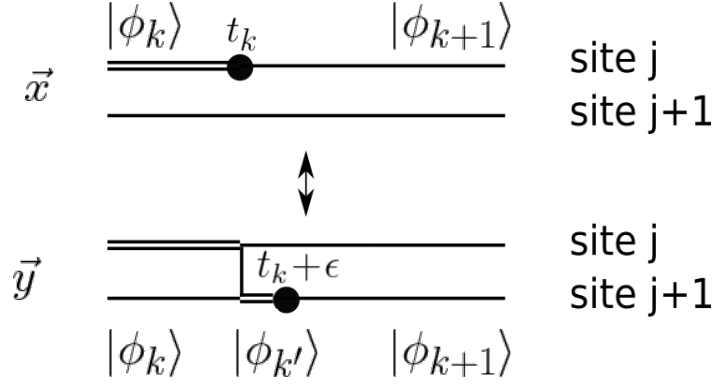


Figure 7.6: Graphical representation of the *Insertkink* and *Deletkink* updates. The worm head, currently residing on site j at time t_k , is introducing a hopping element $\hat{b}_j \hat{b}_{j+1}^\dagger$. The worm head is moved to site $j + 1$, and in this example placed by an infinitesimal small time ϵ to the right of the added kink. This determines the direction of a subsequent *Moveworm* update, which creates the state $|\phi'_k\rangle$.

$P_{Deletkink}(\vec{y} \rightarrow \vec{x}) = 1$. Inserting this into the usual equation for the acceptance ratio results in

$$q_{Insertkink} = \frac{4 \langle \phi_k | \hat{H}_I | \phi_{k'} \rangle P_{alg}(Deletkink)}{P_{alg}(Insertkink)}, \quad (7.45)$$

7.4 Observables

In the previous section it was shown, how the worm algorithm is able to generate configurations, belonging to a bosonic partition function Z and Z_e . However, to study the physical properties of a system, we need to evaluate the various observables, that can serve as order parameters, as discussed in Chapter 6. There are three different types of observables, which are accessible within the above discussed implementation.

Observables \hat{O} that are diagonal in the occupation number basis, which is used for

the worm algorithm, can directly be evaluated. Whenever a diagonal configuration, belonging to Z is generated by a rejected *Insertworm* update or an accepted *Glueworm* update, the expectation value is calculated. For the evaluation according to

$$\langle \hat{O} \rangle_m = \frac{1}{m} \sum_{n=0}^m \langle \phi_n | \hat{O} | \phi_n \rangle \quad (7.46)$$

the algorithm uses the state $|\phi_n\rangle$, present at a fixed reference imaginary time $t = \beta$. With n indexing the states every time a diagonal configuration is created. The reference time is chosen for simplicity in the implementation, and the states $|\phi_k\rangle$, present at the red line in Figure 7.1, would be an equally valid choice for the reference time.

The algorithm is able to keep track of all the kinks, which represent lattice hopping elements, present in a configuration. Every time a diagonal configuration is created, the kinetic energy of the system can thus be estimated as number of kinks averaged over β , and the MC estimate from m configurations can be written as

$$E_{kin}^b = -\frac{1}{m} \sum_{i=0}^m \frac{n_{kink}^b(i)}{\beta} \quad (7.47)$$

with $n_{kink}^b(i)$ being the number of interaction elements, present in the i -th configuration in the Markov process. As there are no restrictions for the worm to introduce kinks at the periodic boundaries of the system, it is possible for the worm head to traverse once through all physical lattice sites and then come back to the worm tail. The bosonic winding number W_b characterizes, how many times the worldlines span across the system by passing the periodic boundaries. This can also directly be calculated in the worm algorithm for every diagonal configuration, when taking the directions of the hopping elements into account, and calculate the difference of the number of right N_b^+ and left N_b^- directed hopping elements in real space (up and down in the figures)

$$W_b = \frac{N_b^+ - N_b^-}{L}. \quad (7.48)$$

The usage of the extended partition function Z_e is not merely a numerical trick for effective sampling, but corresponds to the Green's function sector, as it samples according to those weights. It is possible to measure the equal time Green's function, which corresponds to the single particle density matrix $\mathcal{G}^b(i, j) = \langle \hat{b}_i^\dagger(\tau) \hat{b}_j(\tau) \rangle$ while the worm is moving through the configuration. Each time the worm head passes or connects to the worm tail one has a measurement for the equal time Green's function.

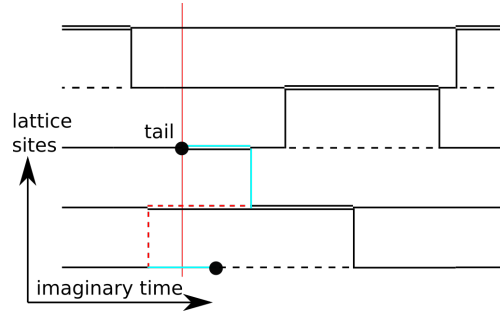


Figure 7.7: Measurement of equal time Green's function. A possible movement of the worm head is presented, using the same iconography as in Figure 7.2. Every time the head crosses the imaginary time of the tail, denoted by the red line this is noted for the density matrix similar to a histogram. What is added to the respective bins may depend on the actual occupation on the lattice sites.

As in the implementation of the *Insertworm* update the weights of the worm operators $\langle \phi_k | \hat{b}_i | \phi' \rangle \langle \phi' | \hat{b}_i^\dagger | \phi_k \rangle = n_i + 1$ were chosen as unity, we have to reweight the measurements of the respective bins for $\mathcal{G}^b(i, j)$ by the factor $n_i + 1$ for $i \neq j$, and the bosonic density outside of the worm operators if $i = j$. Further reweightings for the *Insertworm* update are possible to increase the acceptance ratios, if desired, but have to be taken into account respectively.

7.5 Two worm algorithm

To simulate the 1D sBFHM with a worm algorithm, we map both of the fermionic spin polarizations to a respective hard-core boson component by the Jordan-Wigner transformation. This requires an odd number of fermions in the system, when using periodic boundary conditions, but resolves the infamous sign problem otherwise present for fermions, which results from negative weights for certain configurations in the path integral representation of the partition function. Our simulation thus has one species of soft-core bosons and two species of hard-core bosons present in the same 1D lattice. Except for adjustments of the updates, respecting the new physical weights and proposal functions, we also add the possibility to insert two sets of worm operators into a diagonal function simultaneously. This allows for two worm heads are moving through the system at once. Not only do the equilibration and autocorrelation times in certain parameter regimes get reduced, but entering these extended regimes also enables the measurement of 4-point correlation functions. These correlation functions are for example used to probe the system for the existence

of Cooper pairing of two fermions with opposite spin.

The graphical representation, introduced in Figure 7.1, is straightforward to extend to multiple types of bosons, and a possible configuration is showcased in Figure 7.8. Each component corresponds to one of the three color coded line representations. The

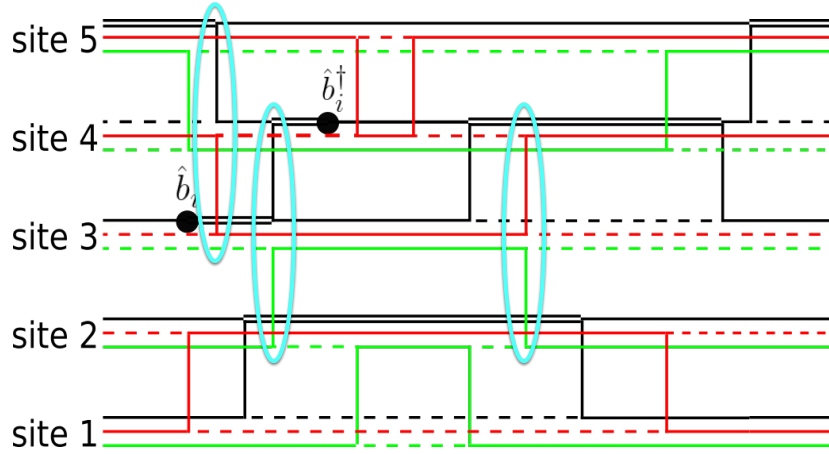


Figure 7.8: Graphical representation of a configuration in the Green's function sector of the soft-core bosons. The time and space directions are defined as in Figure 7.1. The black lines and filled circles correspond to the soft-core bosons in the sBFHM. Each lattice site has now additionally an occupation number for the two hard-core boson species, corresponding to the spinful fermions of the model, denoted by red and green lines. Those occupation numbers are limited to either 0 or 1. Worm heads are allowed to move through the system, following the MC updates, but can not introduce kinks at times of other kinks, where they stopped artificially. Thus the cyan encircled kinks would not be allowed.

new algorithm not only performs updates in the regime of the bosonic extended partition function

$$Z_e^b = \text{tr} \left[\mathcal{T} \left(\left(\hat{b}_i(t_0) \hat{b}_j^\dagger(\tau) + h.c. \right) e^{-\beta \hat{H}} \right) \right], \quad (7.49)$$

but also in the Green's function sector of the fermionic extended partition function of both fermion species

$$Z_e^\uparrow = \text{tr} \left[\mathcal{T} \left(\left(\hat{c}_{i,\uparrow}(t_0) \hat{c}_{j,\uparrow}^\dagger(\tau) + h.c. \right) e^{-\beta \hat{H}} \right) \right], \quad (7.50)$$

$$Z_e^\downarrow = \text{tr} \left[\mathcal{T} \left(\left(\hat{c}_{i,\downarrow}(t_0) \hat{c}_{j,\downarrow}^\dagger(\tau) + h.c. \right) e^{-\beta \hat{H}} \right) \right]. \quad (7.51)$$

\hat{H} is the respective Hamiltonian, we consider the Hamiltonian of the sBFHM, given in Equation 6.30. Thus the diagonal energies, that enter the acceptance ratios for the *Moveworm* update, now have to be calculated accordingly, and the *moveworm* update has to be adapted, as will be discussed in Subsection 7.5.2. The updates *Insertworm*, *Glueworm* and *Insertkink* in either of the three above sectors are otherwise trivial to adapt from the soft-core bosonic updates, presented in Section 7.3. One should only note that it is not allowed to insert kinks at the same imaginary time due to no well defined time ordering for these configurations.

7.5.1 Four operator Insertworm and Glueworm update

Except for the above extended regimes we also update diagonal configurations by entering extended regimes with two open worldlines, which correspond to the extended partition functions

$$Z_e^{(b,\uparrow)} = \text{tr} \left[\mathcal{T} \left((\hat{b}_i(t_0) \hat{b}_j^\dagger(\tau) + h.c.) (\hat{c}_{i,\uparrow}(t'_0) \hat{c}_{j,\uparrow}^\dagger(\tau') + h.c.) e^{-\beta \hat{H}} \right) \right], \quad (7.52)$$

$$Z_e^{(b,\downarrow)} = \text{tr} \left[\mathcal{T} \left((\hat{b}_i(t_0) \hat{b}_j^\dagger(\tau) + h.c.) (\hat{c}_{i,\downarrow}(t'_0) \hat{c}_{j,\downarrow}^\dagger(\tau') + h.c.) e^{-\beta \hat{H}} \right) \right], \quad (7.53)$$

$$Z_e^{(\uparrow,\downarrow)} = \text{tr} \left[\mathcal{T} \left((\hat{c}_{i,\uparrow}(t_0) \hat{c}_{j,\uparrow}^\dagger(\tau) + h.c.) (\hat{c}_{i,\downarrow}(t'_0) \hat{c}_{j,\downarrow}^\dagger(\tau') + h.c.) e^{-\beta \hat{H}} \right) \right]. \quad (7.54)$$

Figure 7.9 displays how, we insert two pairs of operators into the system. In principle it would be a valid possibility to choose two random imaginary times and two random lattice sites, to enter the above regimes with two open worldlines. One for each pair of worm operators. However, as we are interested in the measurement of the equal time 4–point correlation functions $\mathcal{G}^{pp}(x)$ and $\mathcal{G}^{pp}(x)$, we can only measure those, if all four operators reside at the same imaginary time. An insertion at different randomly chosen times would thus make these measurements impossible, as the worm tails are immobile. We thus choose to insert both worm pairs at the same imaginary time and the same lattice site i , both chosen at random as in the case of a single wormpair. After the insertion both wormheads are restricted to reside at the same imaginary time, but are allowed to spread to different lattice sites across the lattice. Thus there is only one direction to be chosen. We can write the weights for Figure 7.9 as

$$W(\hat{x}) = C_{Z_2}, \quad (7.55)$$

$$W(\hat{y}) = \langle \phi_k | \hat{b}_i | \phi' \rangle \langle \phi' | \hat{b}_i^\dagger | \phi_k \rangle \langle \phi_k | \hat{c}_{i,\sigma} | \phi' \rangle \langle \phi' | \hat{c}_{i,\sigma}^\dagger | \phi_k \rangle, \quad (7.56)$$

where σ denotes the spin of the fermion. C_{Z_2} denotes the relative weight between the partition function sectors Z and $Z_e^{(b,\sigma)}$. Similar to the case of a single worm we end up

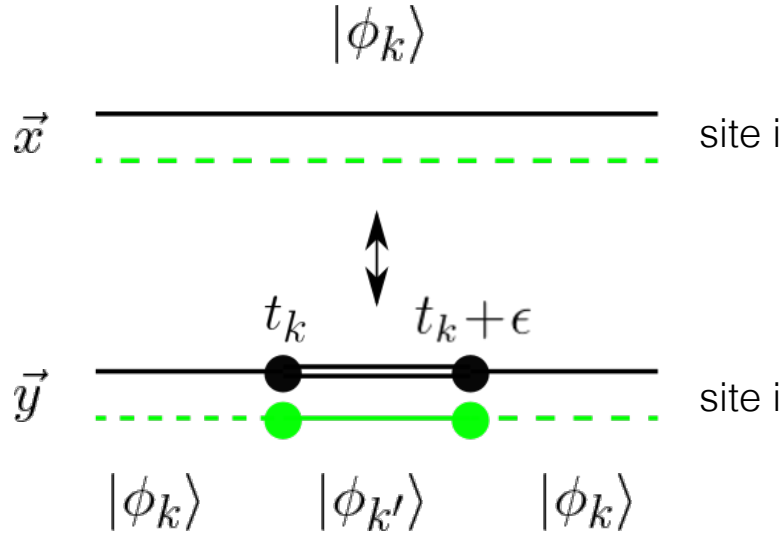


Figure 7.9: Insertworm update with four operators. \vec{x} is a diagonal configuration and \vec{y} a nondiagonal one. The time and space directions are defined as in Figure 7.1. The black symbols correspond to the soft-core bosons and the green symbols to either of the hard-core bosons (fermions). The red lines are present, but are removed for simplicity. Nevertheless all states $|\phi\rangle$ correspond to many body occupation number states, including all lattice sites and all three types of bosons.

with the acceptance ratio

$$q_{\text{Insertworm}} = \frac{8\beta L}{C_{Z_2}} P_{\text{alg}}(\text{Glueworm}) \quad (7.57)$$

for the above cases, with one soft-core and one hard-core boson type, where the additional factor of 2 results from 2 choices of risings. The same equations hold for 4 pairs of hard-core bosonic operators, even though there it would be possible to always choose the correct risings.

7.5.2 New Moveworm

To complete our discussion on the worm algorithm let us take a final closer look at the new *Moveworm* update. Figure 7.10 demonstrates a crucial difference in the new update scheme. It is now possible that the diagonal energies to the left and to the right of the wormhead change. In the shown example from time t_k to t_a the right energy is $E_{\phi_{k+1}}$ and the left one is E_{ϕ_k} . If a timeshift larger than $t_a - t_k$ is proposed,

the wormhead passes t_a , and the movement distance or the acceptance ratio has to change, as now $E_{\phi_{k'}}$ is the energy to the left and $E_{\phi_{k+2}}$ is the energy to the right. Even though it would be possible to account for these energy shifts along the way, it is easier and equally possible to divide those steps and simply stop at kinks of other species, as discussed for kinks of the own species, and then continue movement from there, possibly passing beyond the kink. The *Moveworm* update in the extended

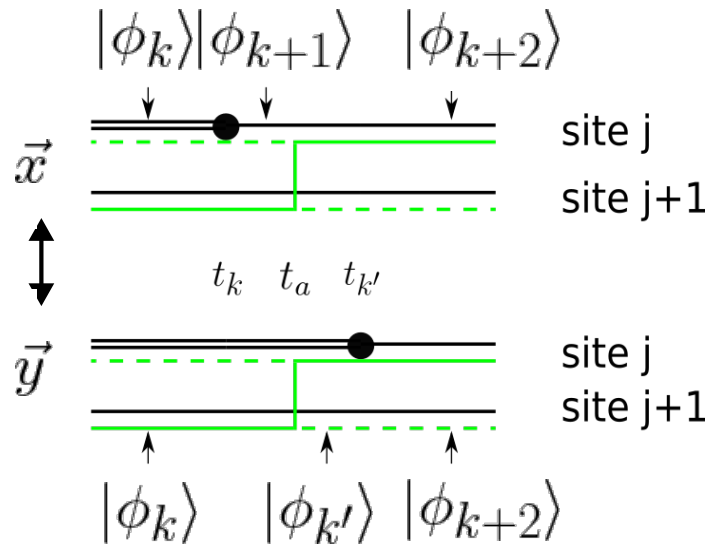


Figure 7.10: Moveworm update for a single wormhead within the new configuration space. A wormhead, belonging to the soft-core bosons, is moving in imaginary time, as explained in Subsection 7.3.2 from t_k to $t_{k'}$. As it does not encounter a kink on its own lattice site, it is in principle allowed to surpass kinks, belonging to other bosonic species, as the commutator is zero. However, the diagonal energy in the plus direction changes at t_a due to the green kink, and thus the acceptance ratios can not be directly calculated as in Equation 7.34.

partition function regime will always keep both wormheads at the same imaginary time. So an update would change two times at once, if accepted, or none of them, if it got rejected. Except from this movement follows the same acceptance ratios, except that now two occupation numbers are changed, and the two worm heads might reside on separate lattice sites thus requiring to check for the next element in movement direction in either site, which might force a stop.

Chapter 8

Phase diagram of the spinful Bose-Fermi-Hubbard model

This chapter is dedicated to the presentation of our results obtained for the sBFHM. We considered the Hamiltonian, given in Equation 6.30, with both fermionic components at half filling and unit filling in the bosons. The bare fermionic interaction is set to zero. Thus for $U_{BF} = 0$ the fermions would be free. We always work in energy units of $t_b = t_f = 1$, if not specified differently. Furthermore in this chapter we use the convention $U = U_{BB}$ for the bosonic intraspecies coupling and $V = U_{BF}$ for the interspecies coupling. In Section 8.1 several limiting regimes are considered, where an analytical understanding can be established. The transition lines, derived from the analytical arguments, are adopted in the phase diagram, which is presented in Section 8.2 and can be seen as the main result of the second part of the thesis. Section 8.3 highlights exemplary numerical results and discusses some of the difficulties in extrapolating the thermodynamically stable phases, which emerged in the finite size analysis of the different competing phases.

8.1 Analytical considerations

As pointed out in Section 6.3 the sBFHM is not completely solvable analytically. However, in this section we will consider certain limiting regimes, where predictions might be possible. The interaction between bosons, induced by the fermions in the weak coupling limit, is discussed first. The effect on the fermions, induced by SF bosons, described in the Bogoliubov approximation, is briefly shown. The section is concluded with a strong coupling expansion.

8.1.1 Weak interspecies coupling regime

At $V = 0$ the Bose-Fermi-Hubbard model naturally resembles the 1D BHM paired with noninteracting spinful fermions. When V changes to small finite values, the fermions and bosons will mutually induce effective intraspecies interactions in the respective other component.

We start with the effect of the fermions on the bosonic part of the system, as discussed with linear response in the work by Büchler and Blatter [161, 178]. A purely bosonic system, described by the BHM Hamiltonian, transitions from the MI phase to the SF phase at $U^c = 3.29(2)$ [125]. Adding fermions to the system with a finite interaction V will result in density perturbations in the bosons δn_b . These bosonic density fluctuations in turn will result in modulations of the fermionic density δn_f . Integrating out the fermions results in an effective onsite potential between the bosons

$$U_{eff} = U + \chi(T, 0)V^2. \quad (8.1)$$

$\chi(T, q)$ is the fermionic response function given by the Lindhard function

$$\chi(T, q) = \int_K \frac{dk}{v_0} \frac{f[\epsilon_F(k)] - f[\epsilon_F(k+q)]}{\epsilon_F(k) - \epsilon_F(k+q) + i\eta}, \quad (8.2)$$

where the integration is over the first Brillouin zone with volume $v_0 = (2\pi/a)^2$, ϵ_F the fermionic energy dispersion and the Fermi distribution function $f(\epsilon) = 1/[1 + \exp(\epsilon/T)]$ [161]. For regular densities of states and low temperatures the response function can be reduced to $\chi(T \rightarrow 0, 0) = -N(0)$ with the fermionic density of states. For free fermions in 1D it is given by

$$N(\epsilon_F) = \frac{1}{\pi t} \sqrt{1 - \left(\frac{\epsilon_F}{2t}\right)^2}. \quad (8.3)$$

Thus the effective bosonic potential can be approximated as

$$U_{eff} = U - \frac{1}{\pi} V^2. \quad (8.4)$$

For weak interactions this induced interaction between the bosons has two implications. First the bosonic SF-MI transition should be shifted upwards with the transition line following $U^c \sim 3.29 + N(0)V^2$. This estimation is drawn as black dash-dotted line in Figure 8.1 and Figure 8.3. The second estimation considers the PS regime. If the initially repulsive bosonic interaction U effectively turns attractive through the fermions, the system will favour phase separation. Therefore when the second term in Equation 8.4 is bigger than the first, namely $\frac{1}{\pi} V^2 > U$, the system

is expected to phase separate. Even though this approach might be too simple, as the mutual influences are not fully respected, and there are other criteria for phase separation [179], the estimation is shown as dotted black line in the lower part of the phase diagram in Figure 8.1.

As we have seen above, the bosons are expected to establish a SF regime in the phase diagram for a finite range of U values at weak interspecies couplings. Let us now turn towards the induced interaction among fermions, caused by this bosonic SF background. In the SF regime the bosons are well described as LL with a linear spectrum. To this end the bosons are described within a Bogoliubov approximation. The validity of this approximation for weakly coupled bosons has been established by the variational cluster approach and the dynamical DMRG method [180]. Here we will highlight the most important steps in the derivation and summarize the results which are relevant to our system. The approximation assumes that the zero momentum ($k = 0$) bosonic mode is macroscopically occupied. The bosonic creation and annihilation operators are first represented in momentum space through

$$\hat{b}_j^\dagger = \frac{1}{\sqrt{L}} \sum_k \hat{b}_k^\dagger e^{-ikr_j}, \quad (8.5)$$

$$\hat{b}_j = \frac{1}{\sqrt{L}} \sum_k \hat{b}_k e^{ikr_j}, \quad (8.6)$$

where r_j is the real space location of lattice site j , and L the linear system size. These momentum space operators are taking the macroscopic occupation of the lowest momentum space into account by replacing them as

$$\hat{b}_k^\dagger \rightarrow \hat{b}_k^\dagger + \sqrt{N_0} \delta_{k,0}, \quad (8.7)$$

$$\hat{b}_k \rightarrow \hat{b}_k + \sqrt{N_0} \delta_{k,0}, \quad (8.8)$$

where N_0 is the number of condensed atoms. The Hamiltonian is rewritten in these terms, and all terms beyond second order in the new operators are discarded, as the fluctuations for higher momentum are assumed to be small in comparison with N_0 . The new approximated Hamiltonian is then by construction quadratic and can be diagonalised with the Bogoliubov transformation [181]. With this approximation the bosons were integrated out, and an effective fermionic system remains, which can be described with the action $S = S_f + S_{ret}$. The effect was found to be twofold, with a shift of the fermionic chemical potential μ_f by $n_0 V$ in S_f , with the condensate fraction $n_0 = N_0/L$, and the induced non-local retarded density-density action term

reported as [182]:

$$S_f = \int_0^\beta d\tau \sum_{\langle i,j \rangle, \sigma} \bar{c}_i^\sigma(\tau) [\delta_{i,j} (\partial_\tau - \mu_f + n_0 V) - t_f] c_j^\sigma(\tau) + U_{FF} \sum_i n_{i,\uparrow}^f(\tau) n_{i,\downarrow}^f(\tau) \quad (8.9)$$

$$S_{\text{ret}} = -\frac{n_0 V^2}{2} \iint_0^\beta d\tau_1 d\tau_2 \sum_{i,j} n_i^f(\tau_1) D_{ij}(\tau_1 - \tau_2) n_j^f(\tau_2). \quad (8.10)$$

Here the kernel is given by

$$D_{ij}(\tau) = \int \frac{dk}{2\pi} e^{ik(r_i - r_j)} \frac{e^{E_k \tau} + e^{E_k(\beta - \tau)} |\bar{\epsilon}_k|}{e^{\beta E_k} - 1} \frac{|\bar{\epsilon}_k|}{E_k}, \quad (8.11)$$

where $\bar{\epsilon}_k = -2(\cos(k) - 1)$ and $E_k = [\bar{\epsilon}_k^2 + 2\bar{\epsilon}_k n_0 U]^{1/2}$ is the dispersion of the Bogoliubov quasiparticles.

When the velocity of the condensate fluctuations is much larger than the Fermi velocity, it is possible to take the instantaneous approximation for the kernel $D_{ij}(\tau)$, which neglects retardation effects, as these are small compared to the contributions of the peaks, located at $\tau = 0$ and $\tau = \beta$ [183]. With this approximation the kernel can be written as

$$D_{\text{static}}^0(x) = \int \frac{dk}{2\pi} e^{ikx} \frac{2|\epsilon_k|}{\epsilon_k^2 + 2\epsilon_k n_0 U}. \quad (8.12)$$

Thus the effect of superfluid bosons, which are fast compared to the fermions, can be seen as an attractive on-site interaction, which scales as $\sim \frac{V^2}{U}$ [182, 183], but repulsive for $x = (r_i - r_j) > 0$. However, the offsite repulsion becomes weaker with increasing distance and scales as $\sim 1/x^2$.

When only the dominant on site attraction is taken into account, the fermions can eventually be described by an attractive 1D FHM at half filling, introduced in Section 6.2, whose solution is known to be the superconducting phase. Even though $1/x^2$ is considered to be a short range interaction, the pairing gap of the fermions might be very weak for the weakly interacting cases, and the next neighbour interaction between the fermions, here denoted as V_{FF} , and described in Subsection 6.2.1 for the eFHM, might suppress the superconducting phase and favour a CDW, as can be seen for the case $V_{FF} > 0$ and $U < 0$ in the phase diagram of the eFHM in Figure 6.5.

However, retardation effects are becoming more important for slower bosons [112, 167, 183], and one thus has to rely on numerics for these cases.

8.1.2 Strong interspecies coupling regime

We start with the limit, where both couplings are strong $V, U \gg 4t$, and as a first approach turn of the hoppings. We can consider Fock product states, discussed in Section 7.1, which satisfy the filling factors $N_b = L$ and $N_\uparrow = N_\downarrow = L/2$. For these constraints it is possible to fill M sites with 2 bosons, costing an energy MU , N sites with one fermion and one boson, contributing an energy NV , and $L - M - N$ sites with up and down fermions. Sites with more than 2 particles of any kind can safely be discarded due to their higher energy. The energy of such a state is $E_g = MU + NV$. Eliminating N with the constraint $2M + N = L$, resulting from the lattice occupation, we can rewrite the energy as $E_g = M(U - 2V)$. Thus the line $2V = U$ signals the transition line which is shown as dashed black line in Figure 8.1. For $V < 0.5U$ the energy is minimized by the states with a homogeneous distribution of one boson and one fermion per lattice site, thus for finite t a bosonic MI with delocalized fermions on top. For $V > 0.5U$ the system will consist of half the lattice sites filled with two bosons and the other half with fermionic doublons. For $t = 0$ all permutations of Fock states will have the same energy. However, for finite values of t the system will realize a PS or a CDW. In second order perturbation theory there is only a diagonal virtual exchange term, described by a term

$$J_z = \frac{6t_b^2}{U - V} + \frac{2t_b^2}{2V - U} - \frac{2t_\sigma^2}{2V}, \quad (8.13)$$

belonging to an effective spin-1/2 XXZ Hamiltonian

$$H^{XXZ} = \sum_i J(\sigma_i^x \sigma_{i+1}^x + \sigma_i^y \sigma_{i+1}^y) + J^z \sigma_i^z \sigma_{i+1}^z. \quad (8.14)$$

This predicts a second transition from the phase with CDW order to the phase separated regime at $V/U \approx 0.717$. This linear estimation is in agreement with our Lanczos results and is plotted as the lower dashed line in Figure 8.1.

8.2 Phase diagram

The ground state phase diagram of the sBFHM, which is the main result of the second part of this thesis, is presented in Figure 8.1. The analytic weak and strong coupling results, discussed in Section 8.1, are visualized in black. The various numerical estimations of the different phase transition lines are explained briefly below the

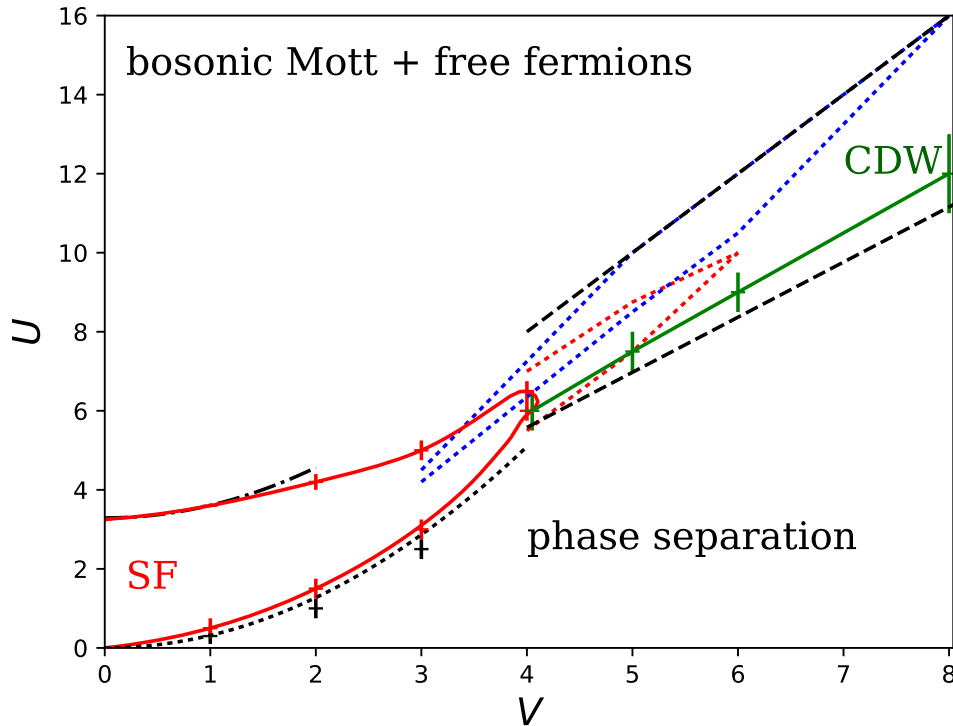


Figure 8.1: Phase diagram of the sBFHM at unit bosonic and double half fermionic filling with all hopping amplitudes set to 1. QMC simulations were performed for the boson fermion couplings $V = 1, 2, 3, 4, 5, 6$ and 8 . The lines between data points thus are only a visual guide. The analytic results are marked by the four black lines, as described in Section 8.1. The stable bosonic SF regime is surrounded by the full red line. CDW order is found in the channel, demarcated by the black dashed lines, however, true long range order can only be found in the region marked by the full green line. Even with lattice sizes of $L \sim 100$ it is not possible to determine for $V \leq 5$, whether the system obeys algebraic or true long range density order. For mesoscopic systems the regimes, demarcated by the red and blue dotted lines indicate bosonic SF and fermionic pair-superflow respectively. For weak couplings the bosonic MI-SF can be clearly identified, but in the intermediate regime a more careful analysis is necessary. Even with system sizes of $L = 250$ it was not possible to predict the behaviour of the fermions in the thermodynamic limit, as the induced interactions are weak across the small to intermediate U, V regime.

figure to give the reader an overview. A more detailed discussion is presented in the next section.

For the regime dominated by strong bosonic repulsion $U \gg V > t$ the system

consists of a bosonic MI and free fermions in agreement with both analytic estimates for weak or strong couplings given for the bosonic MI regime in Section 8.1. PS is found for the contrary regime in the lower part of the phase diagram, where the boson fermion interactions are dominating with $V \gg U > t$. The PS regime extends to small values of V below the dotted line from the weak coupling estimate of induced interactions presented in Subsection 8.1.1. Furthermore in the weak coupling regime we found a stable bosonic superfluid which extends to intermediate interspecies couplings. For the analytically predicted channel at strong couplings $U \gg t$ and $0.5U > V > 0.717U$ we found CDW order, however, the signal is sometimes marginal close to the boundaries but expected to stabilize in the respective regimes in the thermodynamic limit. For mesoscopic systems we find fermionic pair-superflow, induced by the bosons, as the bare U_{FF} is set to zero.

8.3 Numerical results

In this section we highlight some of our numerical findings and check the consistency with the analytical predictions where possible. Subsection 8.3.1 starts with the well known MI-SF transition of the soft-core bosonic component at weak couplings to intermediate interspecies couplings. Then we discuss in details the findings at two fixed V values once at intermediate interspecies couplings $V = 4$ and at stronger interspecies couplings $V = 6$. From these three regimes the rest of the phase diagram presented in Figure 8.1 can be understood.

8.3.1 Bosonic Mott insulator to superfluid transition

In Subsection 6.1.1 the BHM was introduced, and it was shown that it is possible to characterize the MI-SF transition by calculating the bosonic Luttinger parameter K_b . In grand-canonical worm algorithm simulations K_b can be calculated with Equation 6.13 since the compressibility κ , and the bosonic superfluid density $\rho_{s,b}$ are accessible through Equation 6.14 and Equation 6.15.

For the $V = 0$, case discussed in Subsection 8.1.1, we find $U^c = 3.3(1)$, as shown in Appendix C, which is in agreement with the value $U^c = 3.29(2)$, found by other QMC simulations of the pure bosonic system [125]. For weak interspecies couplings $V \leq 2$ our numerics suggests, that the bosonic part of the system is still well described by Luttinger liquid theory. Figure 8.2(a) displays K_b as function of the

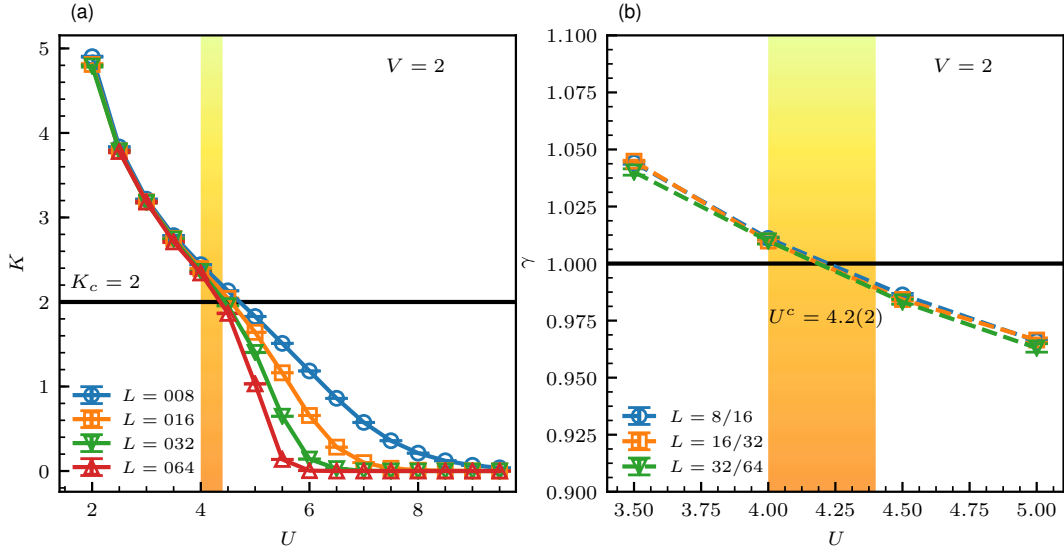


Figure 8.2: (a) Luttinger parameter K over a wide range of U values. The interparticle interaction is fixed to $V = 2$. Different lattice sizes L use respective inverse temperatures $\beta = L/2$. The critical value of K_c is marked by the horizontal black line. (b) The integration parameter γ close to the BKT transition for fixed $V = 2$. γ is independent of the system size for large enough L . Plotted versus U it thus allows for a precise determination of U^C for fixed V . For $V = 2$ we find $U^C = 4.2(2)$.

strenght of the bosonic repulsion U at fixed $V = 2$.

We use the integrated KT equation, which follows from Equation 6.10 and Equation 6.11 and is given by

$$4\ln(L_1/L_2) = \int_{\frac{K_2}{2}}^{\frac{K_1}{2}} \frac{dt}{t^2(\ln(t) - \gamma) + t}, \quad (8.15)$$

where K_1 and K_2 are the Luttinger parameters for two different system sizes L_1 and L_2 , and γ as our fitting parameter. Here pairs of $K_{1,2}$ and $L_{1,2}$ for different system sizes are used to calculate γ numerically [125]. Knowing that $\gamma_c = 1$ is analytic at the transition point, the critical value is estimated by the intersection of γ with γ_c for various combinations of lattice sizes L_1 and L_2 as shown in Figure 8.2(b).

Figure 8.3 displays the results of the simulations in comparison to the weak coupling argument for the MI-SF transition line. For $V = 1$ we still see a very good agreement with the weak coupling line, which assumes free fermions. For $V = 2$ we start to see a small deviation for the system sizes considered in the grand canonical simulations. The values for K_b , determined from Equation 6.13, slightly differ from

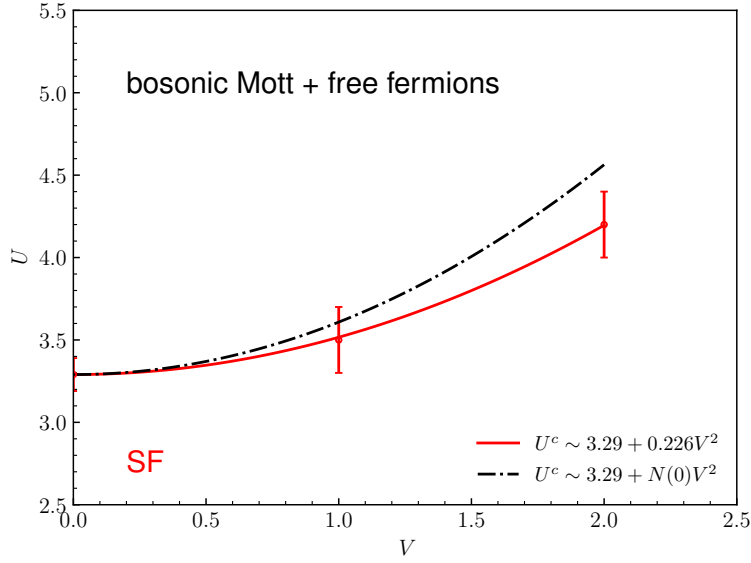


Figure 8.3: $(V - U)$ bosonic MI-SF phase transition line. The weak coupling expectation of a upward shift, discussed in Subsection 8.1.1, is displayed as black dash-dotted line. The numerically found values, based on evaluating Equation 8.15, at $V = 0, 1$ and 2 are shown in red, with the red full line obtained as fit to the weak coupling estimate $U^c = 3.29 + Ax^2$, with A as free fitting parameter. Assuming free fermions the black line uses $A = N(0) = \frac{1}{\pi}$ from Equation 8.3.

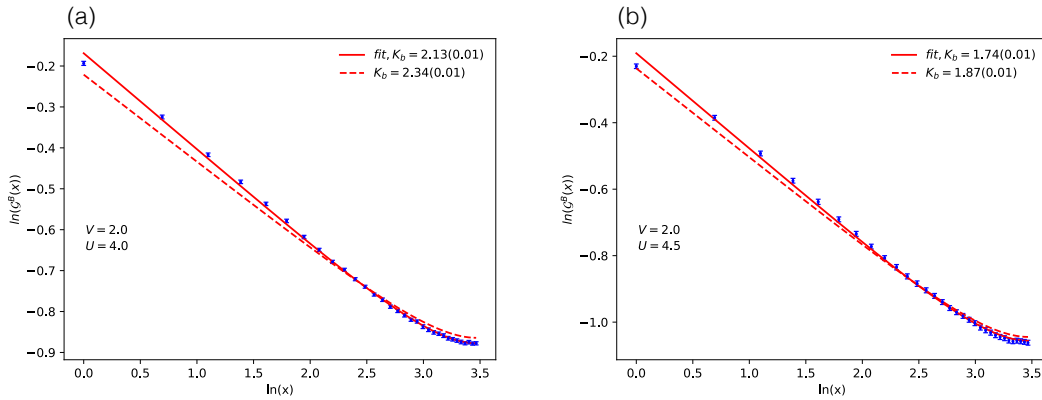


Figure 8.4: (a) **The equal time bosonic density matrix.** The data points for $\mathcal{G}^b(x)$ are depicted in blue, and the corresponding fit with the cord function $\sim d(x|L)^{-1/(2K_b)}$, showing a powerlaw decay with the respective exponent K_b for $V = 2, U = 4, \beta = 0.5L$ and $L = 64$ is showcased in red. The dashed red line shows the powerlaw, assuming the K_b resulting from Equation 8.15. (b) **The same plot but for $U = 4.5$.** All other simulation parameters and notations are the same as for (a).

the ones extrapolated from the equal time Green's function for the largest grand canonical system $L = 64$, considered in this study, as shown in Figure 8.4. If the system is simulated canonically, it is possible to thermalize larger system sizes within reasonable time. With a canonical simulation for $L = \beta = 150$ and $V = 2$ a value of $K_b = 2.02(2)$ was found at $U = 4$ and a decreasing value for $U = 4.5$ as function of the system size, which further supports the transition.

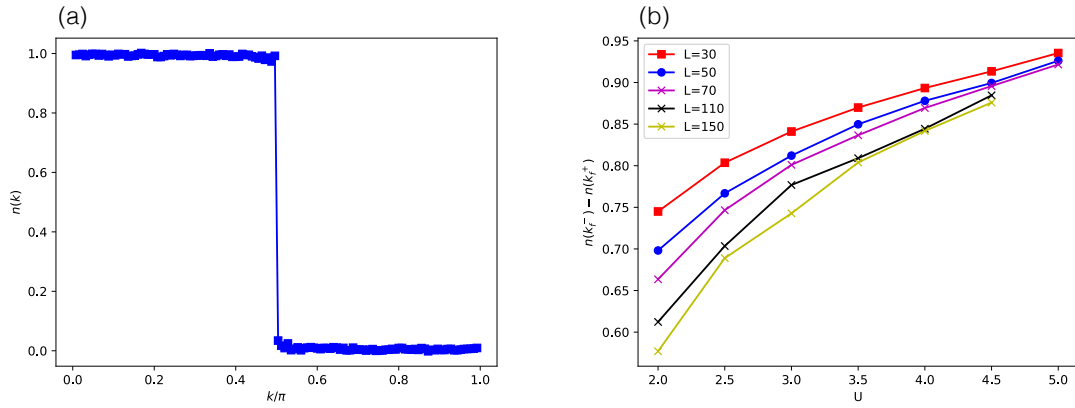


Figure 8.5: (a) **Fermionic occupation number in momentum space.** $n_\sigma(k)$ for weak inter-species interactions $V = 1$, $U = 3.5$ and $\beta = L = 250$. The induced interaction is extremely weak with fermionic Z -factors (jump at k_F) above 0.95, which signals almost free fermions in this regime. (b) **Jump in the fermionic occupation number at k_F .** For $V = 2$ the fermionic jump at the fermi momentum is shown for increasing system sizes at several values of U . The inverse temperature is scaled with system size $\beta = L$.

The deviation between the numerically found value (red) and the black dashdotted estimate from the weak coupling predictions, which assumes free fermions, can be understood, when we consider the fermionic jump. For free non-interacting fermions the momentum dependent occupation number $n_\sigma(k)$ is given by a rectangle function, almost as showcased in Figure 8.5(a) for $V = 1$. All states up to k_F are occupied, and all states above the fermi surface at k_F are empty. Thus there is a jump of 1 visible at $k = \pm k_F = \pm \frac{\pi}{2}$. For $V = 0$ our fermions are indeed non-interacting, as the bare U_{FF} is set to zero. However, for finite V this jump can decrease with increasing system size. This jump can thus be used as indicator for how strongly the renormalization flow away from the non-interacting case has developed. Taking this change in the fermionic density of states into account, the jump is called Z -factor, the quadratic correction, shown in Figure 8.4, can be improved with replacing $\frac{1}{\pi} \rightarrow \frac{Z}{\pi}$. From the jumps for $V = 2$, shown in Figure 8.5(b), the Z -factor close to the transition can

be estimated as $Z \approx 0.85$. Thus the improved weak coupling estimate suggests a transition at $U^c = 3.29 + \frac{Z}{\pi}V^2 = 3.29 + \frac{0.85}{\pi}4 \approx 4.37$, which is then in fair agreement with the value $U^c = 4.2(2)$, reported in Figure 8.2.

Beyond this correction the fermionic jumps in this parameter regime also indicate that the flow in the fermions has just begun. Thus a reliable extrapolation, which of the possible phases is dominant in the thermodynamic limit within the fermions, will not be possible with the system sizes under consideration here, or any system thermalizable in reasonable time with the current numerical approach. Thus even though for $V = 2$ we found no evidence of a CDW for system sizes up to $L = 150$, and pair-flow is visible in mesoscopic system sizes, the option that a CDW order emerges in larger systems, eventually with a small finite amplitude, can not be excluded.

For larger values of the interspecies interaction the deviation from the black dash-dotted line becomes stronger, however, a stable SF, which can be extrapolated to the thermodynamic limit, can be found for interactions up to $V = 4$. For the lower bound of the SF regime we found a sudden drop in the winding numbers in close proximity to the lower dashed black line in the phase diagram, indicative for a first order phase transition towards the PS regime.

8.3.2 Exemplary scan at intermediate interspecies coupling

In Figure 8.6 and Figure 8.7 we display a subset of the various measured observables to analyse the system at $V = 4$. Starting from weak bosonic repulsions U we find signatures of phase separation for the regime below $U < 5$.

For $U = 6$ and $U = 6.5$ the bosonic winding numbers, shown in Figure 8.6(a), suggest the bosonic SF phase. Even though the bare Luttinger parameter K_b , calculated from Equation 6.13 in grand canonical simulations, is suggesting a $K_b > 2$ for this parameter regime, the effective K_b obtained from the algebraic decay of $\mathcal{G}^b(x)$, which by itself is another signature of superfluidity, is systematically resulting in smaller values of K_b below 2 across all lattice sizes. However, this counterintuitive result can be understood considering the framework given in the bosonization approach of Mathey et al. [112, 167]. Based on the assumption of bosons deep in the superfluid regime [112], allowing for a neglect of the Umklapp scattering and backward scattering of bosons, they find a decay of the bosonic Green's function as

$$\mathcal{G}^b(x) \sim x^{-\frac{1}{2K_b}}, \quad (8.16)$$

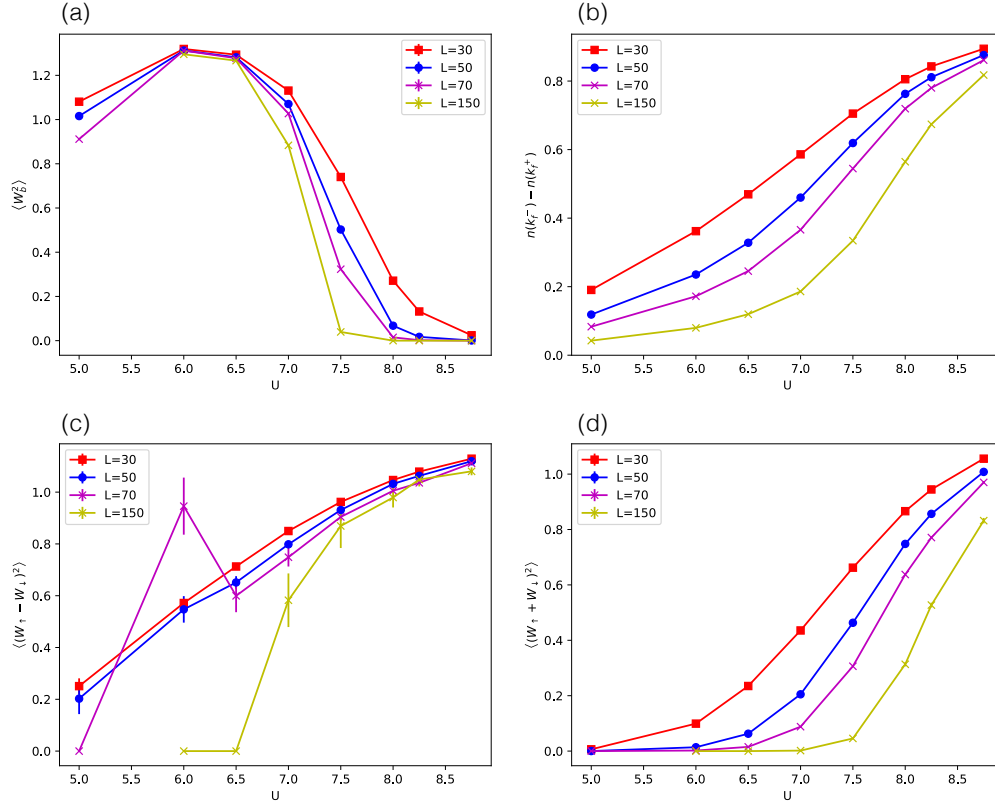


Figure 8.6: Measurements for $V = 4$ and $\beta = L$ from canonical simulations. (a) **Squared bosonic windings:** Constant $\langle W_b^2 \rangle$ is visible for $U = 6$ and $U = 6.5$. In mesoscopic systems a large finite $\langle W_b^2 \rangle$ is observed down to $U = 5$ and up to $U = 7$. (b) **Jump in the fermionic occupation number at k_F :** Non-Fermi-liquid behavior can be observed up to $U \approx 8.5$. At larger U values the Z -factor suggests essentially free fermions. (c) **Squared winding numbers in the pair-flow channel:** Only taking $\langle (W_\uparrow - W_\downarrow)^2 \rangle$ into account, this data suggests a stable pair-flow for U -values in the range $U = 7 - 8$. (d) **Squared winding numbers in the counterflow channel:** The $\langle (W_\uparrow + W_\downarrow)^2 \rangle$ suggests a flow towards zero with increasing system size.

where K_ϵ differs from the bare bosonic luttinger parameter K_b due to a renormalization from the boson fermion interaction, and thus can be smaller than 2 in the superfluid regime. In their approach the bosonic Mott transition would be determined by $K_\delta = 2$, which in turn could be estimated from the $2k_b$ component of the bosonic density-density correlation function which decays as [167]

$$C^b(x) \sim \cos(2k_b x) x^{-2K_\delta}. \quad (8.17)$$

K_δ is always greater than K_b , which also predicts a 'melting' of the MI due to the

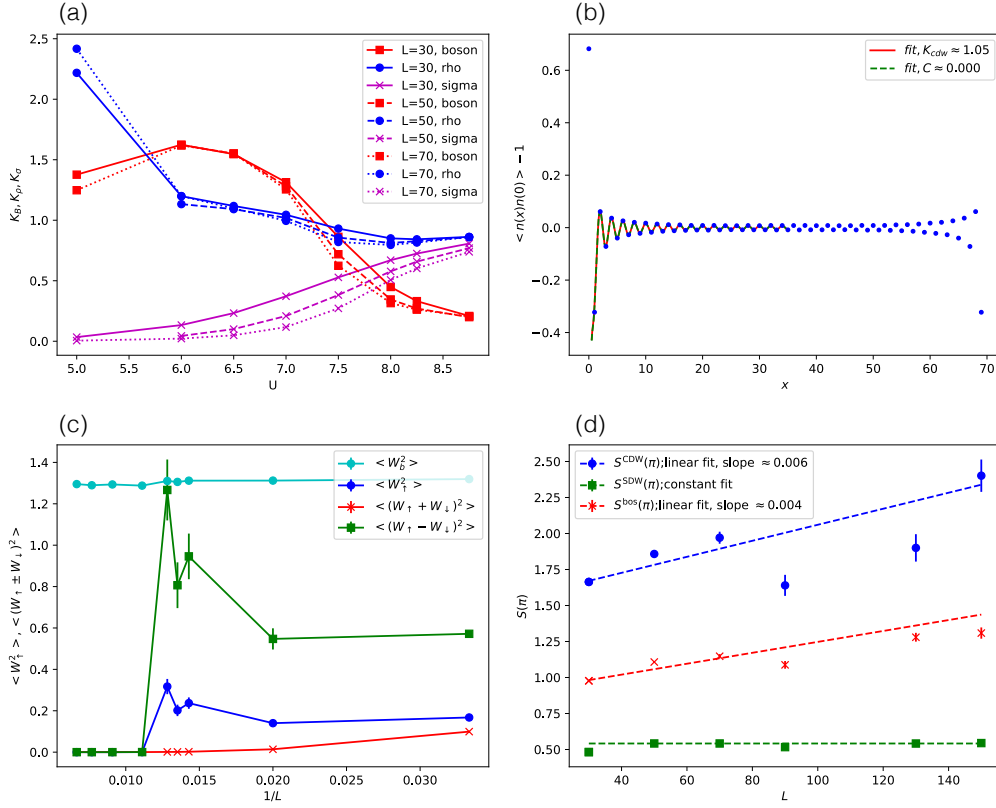


Figure 8.7: Measurements for $V = 4$ and $\beta = L$ from canonical simulations. (a) **Luttinger Parameters:** K is measured in the relevant bosonic and fermionic channels. (b) **CDW correlation function:** Quasi-long range order is visible for $U = 6.5$. (c) **Finite size analysis of the winding numbers at $U = 6$:** Mesoscopic length scales $L < 90$ suggest a tendency towards pairing in the fermions, which vanishes in larger systems. On length scales up to $L < 90$ the bosonic superflow is constant. A small drop is visible when the mesoscopic fermionic superflow vanishes and stabilizes again at a slightly smaller constant value for $L > 90$. (d) **Finite size analysis of structure factors at $U = 6$:** The approximately linear increase in the CDW structure factor suggests that the system develops the lattice symmetry breaking in the thermodynamic limit.

presence of the fermions in their notation, which is the equivalent prediction of our upwards shift, discussed in Subsection 8.1.1. For $g = 0$, which is the fermion-phonon coupling, we retrieve the behaviour of Equation 6.12 [167]. This correction to a smaller extent can also be observed at smaller V values, e.g. in Figure 8.4. Even though their approach would predict a singlet pairing for our parameters, it assumes $v_b \gg v_f$, which might not be fulfilled in all parameter regimes considered in this work and the formation of CDW order is possible.

Turning back to the phase diagram for mesoscopic systems the SF phase extends down to $U \approx 5.5$ and up to $U \approx 7$. However, the bosonic windings in the regime $5.5 \leq U < 6$ and $6.5 < U \leq 7$ indicate a flow towards an insulator in the thermodynamic limit. Thus we indicate this regime by the red dotted line in the phase diagram. Also a fully developed spin gap can be seen for this regime in Figure 8.7(a).

For $U = 6$ pair-flow in the fermions first seems to stabilize on mesoscopic length scales, and even an increase in the flow is visible for $L = 70$, but then the respective winding channel $\langle (W_\uparrow - W_\downarrow)^2 \rangle$ in Figure 8.6(c) jumps to 0, which is also highlighted in Figure 8.7(c). The jump to ~ 0 around $L \approx 90$ preserved across multiple annealing protocols, and the observed bimodality and metastability in the simulations can hint to a first order transition. Further evidence for an fermionic insulator in the presence of superfluid bosons here is found in Figure 8.7(d), where the finite size analysis of the relevant structure factors for this U value is showcased. The simultaneous linear increase in $S^{bos}(\pi)$ and $S^{CDW}(k)$ from Equation 6.18 and Subsection 6.2.1 suggests a marginal SS in the bosons and a CDW in the fermions.

For slightly higher $U = 6.5$ the oscillations of $C^{CDW}(x)$ indicate quasi-long range order in Figure 8.7.

From the upper boundary of the marginal mesoscopic SF at $U = 7$ to $U = 8$ the pairflow seems to be stable on the observed system sizes considering $\langle (W_\uparrow - W_\downarrow)^2 \rangle$. In the phase diagram this regime is indicated by the blue dotted lines.

Continuing to larger U values the fermions cross over to the free fermion behaviour at $U \gtrsim 8.5$, as can be seen in the spin gap in Figure 8.7(a) and the fermionic jump in Figure 8.6(b), which is in qualitative agreement with the upper black dashed strong coupling line, predicting the transition to the MI regime.

8.3.3 Exemplary scan at strong interspecies coupling

Here we discuss the behaviour of the system at $V = 6$, which can be seen as example for the strong coupling regime. In Figure 8.8 we display the same quantities for $V = 6$ as it was done for $V = 4$ in Figure 8.6. Figure 8.8(a) and (c) highlight the decay of $\mathcal{G}^{pp}(x)$ and $\mathcal{G}^{ph}(x)$, defined in Equation 6.27 and Equation 6.27. The connected density-density correlation function $C^{CDW}(x)$ is showcased in Figure 8.8(b) and (d).

Below $U = 8.5$ phase separation is seen in fair agreement with the strong coupling prediction value $\sim 1.39V \approx 8.37$.

Above this regime the bosonic windings indicate that in the thermodynamic limit

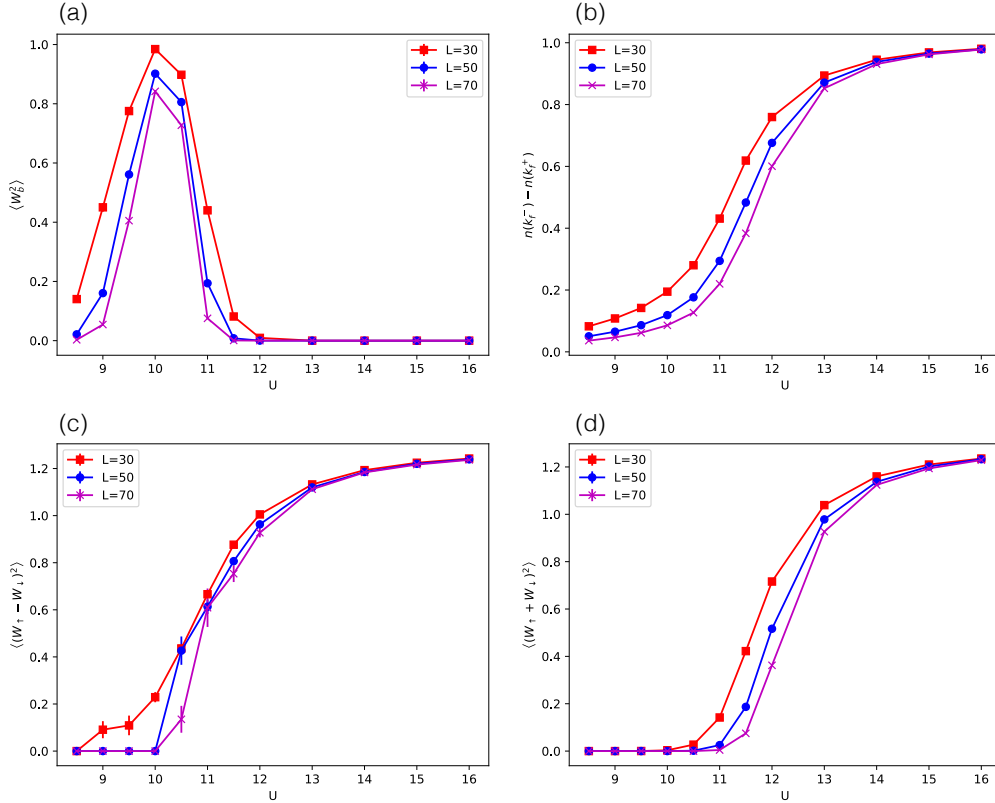


Figure 8.8: Measurements for $V = 6$ and $\beta = L$ from canonical simulations. (a) **Squared bosonic windings:** No constant $\langle W_b^2 \rangle$ is visible anymore. In mesoscopic systems a large finite $\langle W_b^2 \rangle$ is observed for $U = 10$ and $U = 10.5$, however, even there the extrapolation to larger systems suggests insulating bosons. (b) **Jump in the fermionic occupation number at k_F :** Non-Fermi-liquid behavior can be observed except for U values deep enough in the bosonic MI phase. (c) **Squared winding numbers in the pairflow channel:** $\langle (W_\uparrow - W_\downarrow)^2 \rangle$ approaches a finite value for mesoscopic systems in the regime $11 \leq U \leq 12$. (d) **Squared winding numbers in the counterflow channel:** The $\langle (W_\uparrow + W_\downarrow)^2 \rangle$ suggests a flow towards zero for $11 \leq U \leq 12$ with increasing system sizes.

the system turns insulating everywhere, but on small system sizes large bosonic winding numbers can be observed with slow renormalization flow peaked somewhere between $U = 10$ and $U = 10.5$. However, the flow is faster than in the previously discussed case at $V = 4, U = 7$ or at the respective regime at $V = 5$.

Even though the bosons turn insulating in this regime, the fermions display a strong renormalization, as can be seen in the fermionic jump, displayed in Figure 8.8(b), except for $U \gtrsim 13$, where the bosons are deep in the MI regime. For the regime $U \gtrsim 13$, the fermions are expected to be well characterized by free fermions. This is

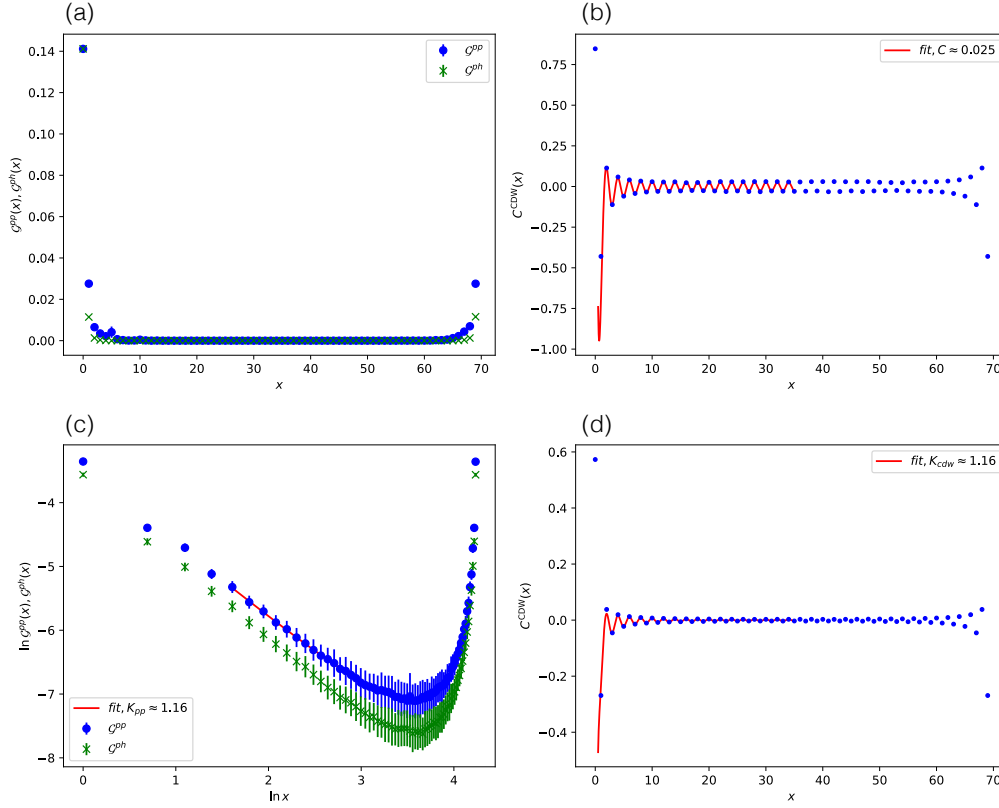


Figure 8.9: Measurements for $V = 6$ and $\beta = L = 70$ from canonical simulations. (a) Decay of the four-point correlators: Both channels $\mathcal{G}^{pp}(x)$ and $\mathcal{G}^{ph}(x)$ display an exponential decay at $U = 9$. **(b) CDW correlation function:** True long-range order is visible at $U = 9$ with an amplitude $C = 0.025$. **(c) Decay of the four-point correlators:** $\mathcal{G}^{ph}(x)$ is still exponential, but $\mathcal{G}^{pp}(x)$ is decaying algebraically at $U = 13$. **(d) CDW correlation function:** Algebraic decay is visible, which indicates quasi-long range order at $U = 13$.

also supported by the behaviour of $\langle (W_{\uparrow} - W_{\downarrow})^2 \rangle$ and $\langle (W_{\uparrow} + W_{\downarrow})^2 \rangle$, displayed in Figure 8.8(c) and Figure 8.8(d), which show no signatures of pairing correlations in either channel.

For the intermediate regime between the two black dashed lines we see a competition between fermionic pairing correlations and the formation of a CDW. Close to the upper black dashed line, indicating the transition to the MI regime, the winding numbers in Figure 8.8(c) for the regime $11 \leq U \leq 12$ seem to stabilize at mesoscopic length scales, suggesting pair-flow and a superconducting regime here. This is indicated by the blue dotted lines in the phase diagram. The winding numbers of the counter-flow channel, showcased in Figure 8.8(c), flow to zero at these U values.

For the regime $9 \leq U \leq 12$ we find indications for lattice symmetry breaking. For $U = 9$ the particle particle and the particle hole four point correlators are shown in Figure 8.9(a). Both channels show an exponential decay here. The oscillations of $C^{CDW}(x)$, showcased in Figure 8.9(b), display true long range order, which can be described by $C \cos(\pi x)$. At this U value a linear growth in the CDW structure factor at $k = \pi$ was observed, similar to the case shown in Figure 8.7(d). Away from $U = 9$ the amplitude C becomes smaller, and for $U = 13$ only quasi-long range order is visible in Figure 8.9(d). Figure 8.9(c) displays the decay of $\mathcal{G}^{pp}(x)$ and $\mathcal{G}^{ph}(x)$ at $U = 13$. In contrast to $U = 9$ $\mathcal{G}^{pp}(x)$ now decays algebraically.

Even though, the bosonic density-density correlator does not display any signs of lattice symmetry breaking on these system sizes ($L = 70$), and the above findings indicate a pairing correlation in the fermions, it should be noticed that the fermionic jump at $U = 13$ in Figure 8.8(b) is still rather large. Thus at larger system sizes we expect, that the mesoscopic pairflow is again misleading and will vanish in larger systems and give rise to the emerging CDW order.

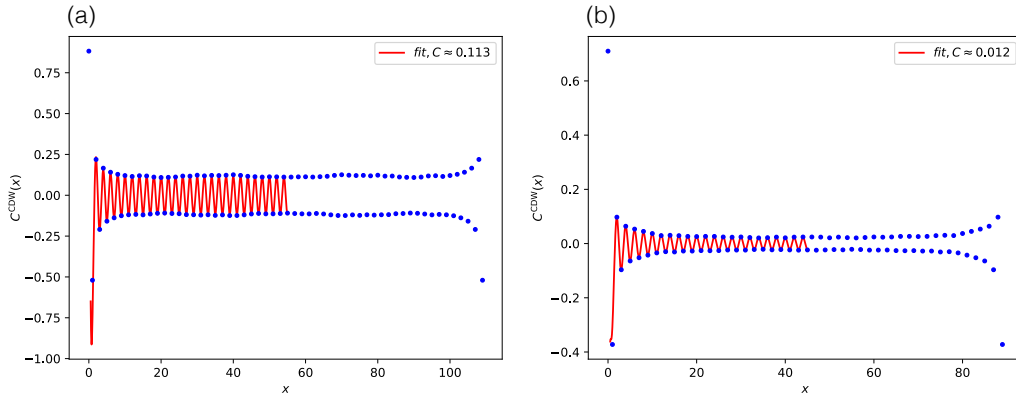


Figure 8.10: Measurements for $V = 8$ and $\beta = L$ from canonical simulations. (a) **CDW correlation function:** True long-range order is visible at $U = 13$ with an amplitude $C = 0.113$ for a system with $L = 110$. (b) **CDW correlation function:** Still true long-range order is visible at $U = 15$, but with a smaller amplitude $C = 0.012$ for a system with $L = 90$.

For even larger values of $V = 8$ we find the dominant CDW across the regime, demarcated by the black dashed lines, and two examples of the true long-range order are showcased in Figure 8.10.

Chapter 9

Conclusions and perspectives

In this thesis exhaustive numerical analyses have been carried out, based on two state-of-the-art MC techniques for interacting many-particle problems, both in the classical and the quantum mechanical realm. Even though the models studied within this thesis can be assigned to the field of statistical physics and display interesting physics by themselves, the relevance of the results of the studied phase diagrams for other research areas has been established.

In the first part we elaborated the connection between quantum error correction codes and classical spin models. With suitable statistical mappings we have succeeded in computing the optimal error thresholds for the X-cube model. As for any CSS code with zero-encoding rate, the resulting respective error thresholds satisfy the quantum Gilbert-Varshamov bound with $H(p_c^X) + H(p_c^Z) \simeq 1.00(2) \leq 1$ and are close to its upper bound. The encouraging result of a minimum error threshold of 7.5% considerably exceeds previously known estimates for conventional topological codes like the 3D Toric code (3.3%) or the Color code (1.9%). Thus it would be interesting to investigate, how future experimental realizations of fracton codes compete against their topological counterparts, which have recently been implemented experimentally for the 2D Toric code [27, 184]. The promising result for this exemplary fracton model paves the way for further theoretical studies of other fracton models like the checkerboard model and type-II fracton codes [66], whose optimal error thresholds are unknown to date. For the statistical physics community the models, which were derived in Chapter 3, have previously only been studied in the absence of quenched disorder. The numerical results, presented in this thesis, were restricted towards the relevant phase boundary of the order-disorder transition, as its crossing with the Nishimori line, which was proven to be free of spin glass features for fracton models by specially designed fracton glass order parameters [P1], gave rise to the error thresholds. However, other parts of the respective phase diagrams remain unexplored

and might display further interesting physics, considering the inherent subsystem symmetry, and therefore call for further investigations.

The second part of this thesis considered a numerical approach to understand the interesting physics and mutual interactions in the sBFHM. Despite the fact that our multi component worm algorithm works well beyond the limits of a smaller restricted Hilbert space, as it was done in the latest DMRG calculations for the sBFHM with a restriction of the maximum soft-core bosonic occupation number $n_{max} = 3$ [170, 185, 186], we are able to thermalize systems beyond the mesoscopic scale. The presented algorithm works well across all parameter regimes, except for the regime in close proximity of PS, which dominates the lower part of the presented phase diagram. For the upper part, where $U \gg V$, we found a bosonic MI with superimposed free fermions. The narrow regime in between was first estimated analytically for both, the weak coupling regime and the strong coupling regime. Then we carefully analysed, considering the various relevant order parameters, the finite size effects, present in the system, to determine the thermodynamically stable phases. For strong interactions we established the qualitative agreement of the CDW regime with the analytically estimated phase boundaries, despite the remarkably weak CDW order. For weak couplings we found a good agreement of the bosonic MI-SF phase boundary with the predicted quadratic upwards shift, which was elaborated in Chapter 8. For the intermediate coupling regime the data hints to the necessity of very large systems, to reliably extrapolate to the thermodynamic limit. However, on mesoscopic system sizes pair-flow and SS behaviours can be found. This calls for extreme caution in further studies of regimes with competing instabilities, since initially visible flows for small system sizes can be misleading, and only large enough length scales give rise to a reliable extrapolation. Especially for weak couplings the pairing interaction between the fermions, induced by the weak interspecies interactions, are so weak that an observation of the flow to large enough system sizes seems impossible with the current computational method.

Appendix A

Simulational parameters for the RPI and RACAT model

Simulating quenched disorder systems with first-order PTs is generally a challenging task. In the simulations of the 3D RPI and RACAT model we use parallel tempering updates, as described in Section 4.4, combined with the local heat bath updates, in analogy to those in Subsection 4.3.2, and a planar spin-flip update to equilibrate the systems [75]. The distribution of temperatures is carefully chosen for each (p, L) set to ensure optimal acceptance ratios in the parallel tempering updates across the majority of the quenched disorder systems [99]. Large numbers (N_d) of quenched random coupling systems are considered, with $N_d = 200$ in the low p regimes and $N_d = 800, 1600$ for p values near the error thresholds where necessary.

Statistical error bars for all post processing estimations are calculated by the bootstrap method [187, 188], and statistical error bars of individual observables, directly implemented in the simulation, are estimated by a "FullBinningAccumulator" within the ALPSCore library [189]. Proper equilibration of individual quenched systems is tested by a binning analysis. The system is considered as equilibrated, when at least the last three bins agree within statistical uncertainty [61]. Parameters of the simulations are summarized in Table A.1 and Table A.2.

Even though the production runs for each quenched system consists of $2^{\tau_{\max}}$ MC sweeps and thus represents well equilibrated simulations, the statistics for the order parameters is much smaller. The update structure consists of several lattice sweeps, followed by one parallel tempering update. One lattice sweep hereby consists of L^3 local heat-bath updates, randomly chosen across the lattice, and one planar spin-flip update. The planar spin-flip update utilizes the degeneracy of the system and thus

Appendix A Simulational parameters for the RPI and RACAT model

traverses the system from the current configuration to one of the randomly chosen degenerate states. After each of these update blocks a measurement is carried out, and the current configuration is stored. By skipping the intermediate configurations we end up with less statistics, but in exchange each stored configuration is less correlated to its predecessor.

p	L	N_d	τ	N_T	T_{\min}	T_{\max}
0.000	04,06	200	23	56	2.50	6.23
0.000	08	200	23	56	2.50	6.00
0.000	10	200	22	56	3.50	6.00
0.025	04,06	200	23	56	2.00	5.70
0.025	08	200	23	56	3.10	5.50
0.025	10	200	22	56	3.10	5.50
0.050	04,06	200	23	56	2.00	5.73
0.050	08	200	23	56	2.80	5.50
0.050	10	200	22	56	2.85	4.50
0.075	04,06	200	23	56	2.00	5.80
0.075	08	200	23	56	2.40	5.50
0.075	10	200	22	56	2.40	5.50
0.100	04,06	200	23	56	2.00	5.83
0.100	08	200	23	56	2.00	5.50
0.100	10	200	22	56	2.00	5.00
0.125	04,06	200	23	56	1.70	5.88
0.125	08	200	23	56	1.65	5.50
0.125	10	200	22	56	1.65	5.36
0.140	04,06	200	23	56	0.30	5.93
0.140	08	200	23	56	0.30	5.50
0.140	10	200	22	56	1.10	5.00
0.142	04,06	800	23	56	1.30	5.50
0.142	08	800	23	56	1.30	5.00
0.142	10	800	22	56	1.30	5.00
0.144	04,06	800	23	56	1.15	5.50
0.144	08	800	23	56	1.15	5.36
0.144	10	800	22	56	1.15	5.36
0.146	04,06	800	23	56	1.10	5.33
0.146	08	800	23	56	1.10	5.00
0.146	10	800	22	56	1.10	5.00
0.148	04,06	800	23	56	1.10	5.33
0.148	08	800	23	56	1.10	5.00
0.148	10	800	22	56	1.10	5.00
0.150	04,06	800	23	56	1.00	5.38
0.150	08	800	23	56	1.00	5.46
0.150	10	800	22	56	1.00	5.46
0.152	04,06	1600	23	56	1.00	5.
0.152	08	1600	23	56	1.00	5.46
0.152	10	1600	22	56	1.00	5.46
0.154	04,06	1600	23	56	1.00	5.
0.154	08	1600	23	56	1.00	5.
0.154	10	1600	22	56	1.00	5.
0.156	04,06	1600	23	56	0.7	5.
0.156	08	1600	23	56	0.7	5.
0.156	10	1600	22	56	0.7	5.

Table A.1: Simulation parameters for the 3D RPI model. L is the linear size of the system. N_d denotes the number of random coupling configurations at the error rate p^X . More quenched disorder systems N_d are considered near the X error threshold $p_c^X \simeq 0.148$. $2^{\tau_{\max}}$ represents the number of MC sweeps in a simulation. N_T temperatures between T_{\min} and T_{\max} are simulated in parallel. The same conventions are used for the 3D RACAT model in Table A.2.

Appendix A Simulational parameters for the RPI and RACAT model

p	L	N_d	τ	N_T	T_{\min}	T_{\max}
0.020	06,08	200	22	64	0.80	2.79
0.020	10	200	22	64	1.17	2.29
0.020	12	200	22	64	1.27	2.13
0.040	06,08	200	22	64	0.98	2.41
0.040	10	200	22	64	1.10	2.14
0.040	12	200	22	64	1.13	2.07
0.050	08	200	22	64	0.44	2.74
0.050	10	200	22	64	0.81	2.37
0.050	12	200	22	64	1.08	2.11
0.060	06,08	200	22	64	0.39	2.78
0.060	10	200	22	64	0.61	2.36
0.060	12	200	22	64	0.91	2.14
0.070	06,08	200	22	64	0.30	2.60
0.070	10	200	22	64	0.50	2.45
0.070	12	200	22	64	0.66	2.25
0.072	06,08	200	22	56	0.30	2.70
0.072	10	200	22	56	0.35	2.50
0.072	12	200	22	56	0.53	2.26
0.073	06,08	800	22	56	0.30	2.70
0.073	10	800	22	56	0.35	2.50
0.073	12	800	22	56	0.53	2.26
0.074	06,08	800	22	64	0.30	2.60
0.074	10	800	22	64	0.35	2.50
0.074	12	800	22	64	0.53	2.25
0.075	06,08	800	22	64	0.30	2.60
0.075	10	800	22	64	0.35	2.50
0.075	12	800	22	64	0.53	2.25
0.076	06,08	800	22	64	0.30	2.60
0.076	10	800	22	64	0.35	2.50
0.076	12	800	22	64	0.53	2.25
0.078	06,08	800	22	64	0.30	2.60
0.078	10	800	22	64	0.35	2.50
0.078	12	800	22	64	0.51	2.23

Table A.2: Simulation parameters for the 3D RACAT model. The same notation as in Table A.1 is used.

Appendix B

Kramers-Wannier duality for CSS code

Appendix B follows closely the elaboration on the Kramers-Wannier duality relation between the 3D RPI and the 3D RACAT model reported in the supplementary material S.I [P1]. To avoid any confusion we use the notation reported there, where the Hamiltonian of the RPI model, which can be found in Equation 3.25, is denoted by $H_\eta^A \equiv H_{\tau p}^A$, and the Hamiltonian of the RACAT model by $H_\eta^B \equiv H_{\tau \mu}^B$. Furthermore the configurations denoted by $n(l)$ in the mappings established in Equation 3.26 and Equation 3.28 are referred to by η .

In the ($p = 0$) limit, where the duality between H_η^A and H_η^B is exact, there are no physical errors in the qubits, thus there is only one error equivalence class, which is the trivial one ($\eta \equiv 0$). The partition function, which models the bit-flip X -errors in the mapping of error chains to coupling constants according to Equation 3.26, is here denoted by $Z_n^A \equiv \mathcal{Z}_\eta^A$ and the respective one for phase-flip errors by $Z_n^B \equiv \mathcal{Z}_\eta^B$. In the disorder free limit \mathcal{Z}_η^A can be reduced to

$$\mathcal{Z}_0^A(\beta) = \sum_{f \in \mathbb{Z}_2^A} e^{\beta \sum_{\ell \in \mathcal{Q}} (-1)^{\partial_A f(\ell)}} = \sum_{f \in \mathbb{Z}_2^A} W_\beta(\partial_A f), \quad (\text{B.1})$$

where $f \equiv \{f(c)\}_{c \in \mathcal{A}} \in \mathbb{Z}_2^A$ labels the configuration of type- A stabilizer generators as it was done with the chains in the main text. $\partial_A f \in \mathbb{Z}_2^{\mathcal{Q}}$ specifies the corresponding qubit configuration with respect to errors, and the respective Boltzmann weight is given by $W_\beta(\xi) := \prod_\ell e^{\beta(-1)^{\xi(\ell)}}$ for a general qubit configuration $\xi \in \mathbb{Z}_2^{\mathcal{Q}}$.

The Kramers-Wannier duality can be considered as a Fourier transform [95]. The

Appendix B Kramers-Wannier duality for CSS code

dual of W_β can be represented as

$$\begin{aligned}\widetilde{W}_\beta(\zeta) &:= 2^{-\frac{|\mathcal{Q}|}{2}} \sum_{\xi \in \mathbb{Z}_2^{\mathcal{Q}}} W_\beta(\xi) e^{-i\pi \langle \zeta, \xi \rangle} \\ &= \prod_{\ell \in \mathcal{Q}} \sqrt{\sinh 2\beta} e^{\tilde{\beta}(-1)^{\zeta(\ell)}} = (\sinh 2\beta)^{\frac{|\mathcal{Q}|}{2}} W_{\tilde{\beta}}(\zeta),\end{aligned}\quad (\text{B.2})$$

in terms of the dual inverse temperature $\tilde{\beta}$ specified by the relation

$$\sinh(2\beta) \sinh(2\tilde{\beta}) = 1, \quad (\text{B.3})$$

where $\zeta \in \mathbb{Z}_2^{\mathcal{Q}}$ is the conjugate variable of ξ , and $\langle \zeta, \xi \rangle := \sum_{\ell \in \mathcal{Q}} \zeta(\ell) \xi(\ell)$ denotes an inner product.

Taking the Fourier transform representation into account the partition function \mathcal{Z}_0^A can be rewritten as

$$\mathcal{Z}_0^A(\beta) = 2^{-\frac{|\mathcal{Q}|}{2}} \sum_{f \in \mathbb{Z}_2^{\mathcal{A}}} \sum_{\zeta \in \mathbb{Z}_2^{\mathcal{Q}}} \widetilde{W}_\beta(\zeta) e^{i\pi \langle \zeta, \partial_A f \rangle}. \quad (\text{B.4})$$

Using the identities $\langle \zeta, \partial_A f \rangle = \langle \partial_A^\dagger \zeta, f \rangle$ and $\sum_{f \in \mathbb{Z}_2^{\mathcal{A}}} e^{i\pi \langle \partial_A^\dagger \zeta, f \rangle} = 2^{|\mathcal{A}|} \delta(\partial_A^\dagger \zeta)$ one finds that only those ζ , which fulfill $\zeta \in \ker \partial_A^\dagger$, contribute here. As the choice of boundary conditions has no influence on the free energy density in the thermodynamical limit, we can choose open boundary condition without loss of generality. With an appropriate choice we can write $\ker \partial_A^\dagger = \text{im } \partial_B \simeq \mathbb{Z}_2^{\mathcal{B}} / \ker \partial_B$. With these considerations Equation B.4 can be expressed as

$$\mathcal{Z}_0^A(\beta) = \frac{2^{|\mathcal{A}| - \frac{|\mathcal{Q}|}{2}}}{|\ker \partial_B|} \sum_{g \in \mathbb{Z}_2^{\mathcal{B}}} \widetilde{W}_\beta(\partial_B g), \quad (\text{B.5})$$

where g labels the configurations belonging to the physical type- B stabilizer generators, and the application of the respective boundary map on g results in the corresponding error configuration $\partial_B g = \zeta \in \text{im } \partial_B$.

Thus, the Kramers-Wannier duality for CSS codes in the absence of disorder can be written as

$$\mathcal{Z}_0^A(\beta) = \frac{2^{|\mathcal{A}| - \frac{|\mathcal{Q}|}{2}}}{|\ker \partial_B|} (\sinh 2\beta)^{\frac{|\mathcal{Q}|}{2}} \sum_{g \in \mathbb{Z}_2^{\mathcal{B}}} W_{\tilde{\beta}}(\partial_B g) = \frac{2^{|\mathcal{A}| - \frac{|\mathcal{Q}|}{2}}}{|\ker \partial_B|} (\sinh 2\beta)^{\frac{|\mathcal{Q}|}{2}} \mathcal{Z}_0^{\mathcal{B}}(\tilde{\beta}). \quad (\text{B.6})$$

As the X-cube model belongs to the class of CSS codes, the duality between PIM and the ATM follows immediately. As this can be considered as the $p = 0$ case of the RPI model and the RACAT model, we can write $H_{\eta=0}^A$ and $H_{\eta=0}^B$.

However, if disorder is present in the system ($p > 0$), the above exact duality for the $p = 0$ case of the RPI and the ATM can no longer be established. However, the results summarized in our associated recently published work [P1] together with previous studies for models with the more conventional global or local symmetries [64, 190, 191] suggest an approximate duality relation between the respective optimal error thresholds p_c^X and p_c^Z , which can be written as

$$H(p_c^X) + H(p_c^Z) \approx 1, \quad (\text{B.7})$$

where H denotes the Shannon entropy, which is defined by

$$H(p) := -p \log_2(p) - (1 - p) \log_2(1 - p). \quad (\text{B.8})$$

Appendix C

Benchmarking the worm algorithm

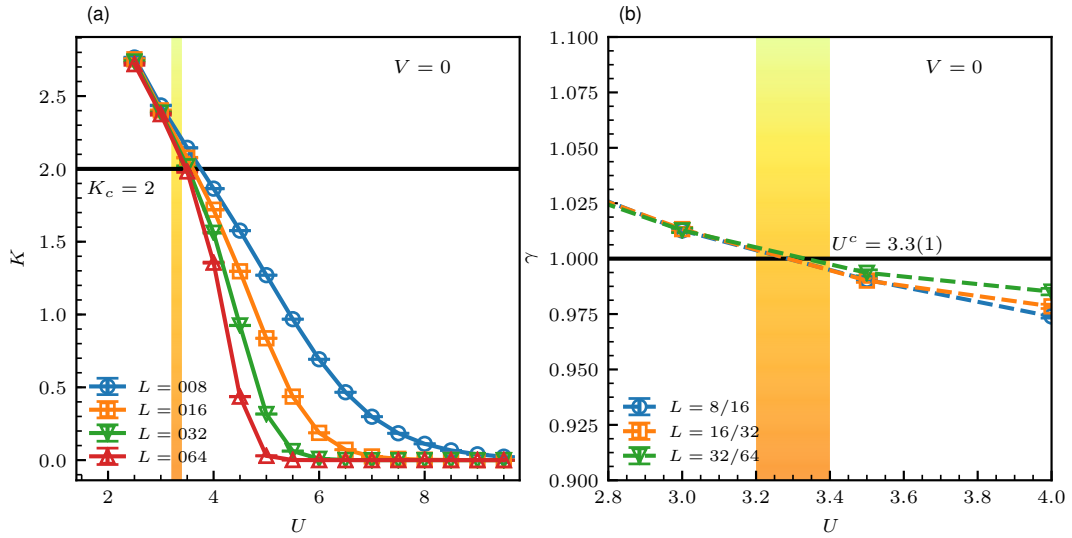


Figure C.1: (a) Luttinger parameter K over a wide range of U values. The interparticle interaction is fixed to $V = 0$. Different lattice sizes L use respective inverse temperatures $\beta = L/2$. The critical value of K_c is again marked by the horizontal black line and the same equations were used as for Figure 8.2. (b) The integration parameter γ close to the BKT transition for fixed $V = 2$. γ is independent of the system size for large enough L . Plotted versus U it thus allows for a precise determination of U^C for fixed $V = 0$. We find $U^C = 3.3(1)$ in perfect agreement with the literature value of $U^c = 3.29(2)$ [125].

In Appendix C we verify the results from the worm algorithm against previously known cases to validate the method and our implementation. Similar to what was done for the parallel tempering MC algorithm, where our numerics established the agreement of our result for the disorder free case of the RPI model to the previously known case of the PIM in Subsection 5.1.4, here we benchmark our algorithm for

Appendix C Benchmarking the worm algorithm

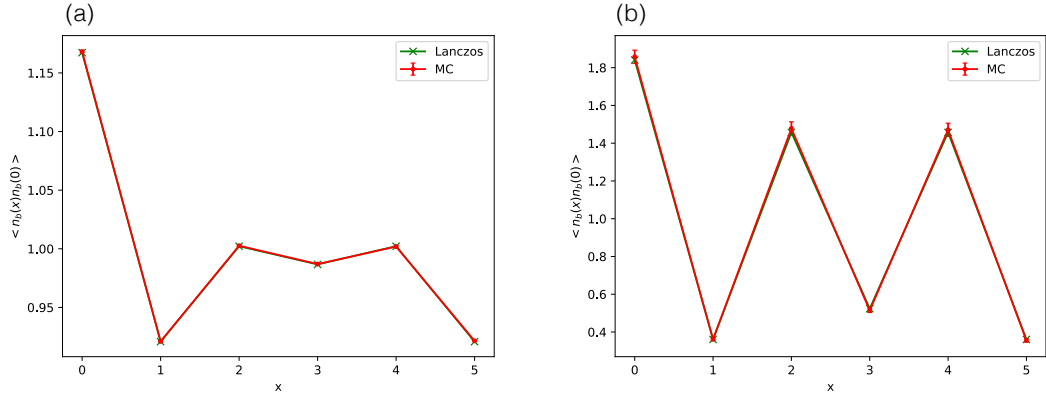


Figure C.2: (a) **Bosonic density-density correlation function results for $L = 6$.** The parameters are $U = 20$, $V = 10$, $N_b = 6$, $N_\uparrow = N_\downarrow = 3$. The red QMC results from the worm algorithm perfectly agree with the green Lanczos results within errorbars. (b) **Same plot but for $V = 20$, $U = 12.5$.** Again perfect agreement is established. Also the qualitatively expected density modulations are visible in this CDW regime expected for strong couplings between $0.5U < V < 0.717$ as discussed in Subsection 8.1.2.

the sBFHM against the case of a softcore bosonic system superimposed with free noninteracting fermions in the absence of an interspecies coupling $V = 0$, $U_{FF} = 0$ in Figure C.1.

To also verify the correct implementation of interactions, we also compared our results from the QMC method to the Lanczos method, mentioned in Section 7.1, for small system sizes up to $L = 6$, limited by the large local Hilbert space of the model. Only for the PS regime the QMC was not able to deliver reasonable results as expected. Exemplary we show here the perfect agreement for the strong coupling regime, once at the MI-CDW transition line at $U = 2V$ in Figure C.2(a) and once between the two black dashed lines in Figure C.2(b), where we analytically expect CDW order in the system.

For other parameter regimes we compared the energies in the system across different parameter regimes. Figure C.3 displays exemplary the potential E_{pot} and the total energy E_{tot} in the system for fixed interparticle interaction $V = 1$.

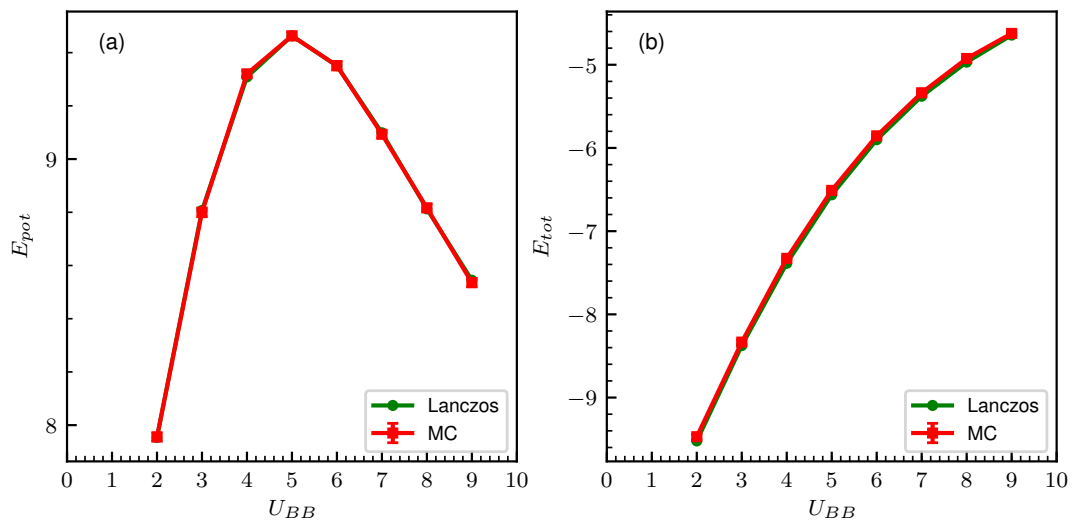


Figure C.3: (a) E_{pot} for $L = 6$. The parameter U is varied for fixed interparticle interaction $V = 1$ with particle numbers $N_b = 6$, $N_{\uparrow} = N_{\downarrow} = 3$ and $n_{max} = 2$. The red QMC results from the worm algorithm agree with the green Lanczos results within errorbars. (b) **Same parameters but the E_{pot} is displayed.** Agreement is established in both SF regimes at small U values and MI regimes at large U values.

Bibliography

1. Lee, P. A. From high temperature superconductivity to quantum spin liquid: progress in strong correlation physics. *Reports on Progress in Physics* **71** (2008).
2. Arute, F., Arya, K., Babbush, R., *et al.* Quantum supremacy using a programmable superconducting processor. *Nature* **574** (2019).
3. Zhong, H. S., Wang, H., Deng, Y. H., *et al.* Quantum computational advantage using photons. *Science* **370** (2020).
4. Lucas, A. Ising formulations of many NP problems. *Frontiers in Physics* **2** (2014).
5. Shor, P. W. Polynomial-time algorithms for prime factorization and discrete logarithms on a quantum computer. *SIAM Journal on Computing* **26** (1997).
6. Bernstein, D. J. in *Post-Quantum Cryptography* (2009).
7. Biamonte, J., Wittek, P., Pancotti, N., *et al.* *Quantum machine learning* 2017.
8. Feynman, R. P. Simulating physics with computers. *International Journal of Theoretical Physics* **21** (1982).
9. Johnson, M. W., Amin, M. H., Gildert, S., *et al.* Quantum annealing with manufactured spins. *Nature* **473** (2011).
10. Lanting, T., Przybysz, A. J., Smirnov, A. Y., *et al.* Entanglement in a quantum annealing processor. *Physical Review X* **4** (2014).
11. Lechner, W., Hauke, P. & Zoller, P. A quantum annealing architecture with all-to-all connectivity from local interactions. *Science Advances* **1** (2015).
12. Albash, T. & Lidar, D. A. Adiabatic quantum computation. *Reviews of Modern Physics* **90** (2018).
13. Deutsch, D. QUANTUM THEORY, THE CHURCH-TURING PRINCIPLE AND THE UNIVERSAL QUANTUM COMPUTER. *Proceedings of The Royal Society of London, Series A: Mathematical and Physical Sciences* **400** (1985).

Bibliography

14. Nielsen, M. A. & Chuang, I. L. Programmable quantum gate arrays. *Physical Review Letters* **79** (1997).
15. Nielsen, M. A., Chuang, I. & Grover, L. K. Quantum Computation and Quantum Information. *American Journal of Physics* **70** (2002).
16. Bremner, M. J., Dawson, C. M., Dodd, J. L., *et al.* Practical Scheme for Quantum Computation with Any Two-Qubit Entangling Gate. *Physical Review Letters* **89** (2002).
17. Blatt, R. & Roos, C. F. *Quantum simulations with trapped ions* 2012.
18. Bloch, I., Dalibard, J. & Nascimbène, S. *Quantum simulations with ultracold quantum gases* 2012.
19. Gross, C. & Bloch, I. *Quantum simulations with ultracold atoms in optical lattices* 2017.
20. Bharath, H. M., Scherg, S., Kohlert, T., *et al.* Benchmarking a novel efficient numerical method for localized 1D Fermi-Hubbard systems on a quantum simulator. arXiv: arXiv:2105.06372v1 (2021).
21. Chow, J. M., Dicarlo, L., Gambetta, J. M., *et al.* Optimized driving of superconducting artificial atoms for improved single-qubit gates. *Physical Review A - Atomic, Molecular, and Optical Physics* **82** (2010).
22. Brown, K. R., Wilson, A. C., Colombe, Y., *et al.* Single-qubit-gate error below 10^{-4} in a trapped ion. *Physical Review A - Atomic, Molecular, and Optical Physics* **84** (2011).
23. Arroyo-Camejo, S., Lazariev, A., Hell, S. W., *et al.* Room temperature high-fidelity holonomic single-qubit gate on a solid-state spin. *Nature Communications* **5** (2014).
24. Preskill, J. Quantum computing in the NISQ era and beyond. *Quantum* **2** (2018).
25. Dennis, E., Kitaev, A., Landahl, A., *et al.* Topological quantum memory. *Journal of Mathematical Physics* **43** (2002).
26. Bombin, H. & Martin-Delgado, M. A. Topological quantum distillation. *Physical Review Letters* **97** (2006).
27. Vuillot, C., Asasi, H., Wang, Y., *et al.* Quantum error correction with the toric Gottesman-Kitaev-Preskill code. *Physical Review A* **99** (2019).

28. Bloch, I., Dalibard, J. & Zwerger, W. Many-body physics with ultracold gases. *Reviews of Modern Physics* **80** (2008).
29. Lewenstein, M., Sanpera, A., Ahufinger, V., *et al.* Ultracold atomic gases in optical lattices: Mimicking condensed matter physics and beyond. *Advances in Physics* **56** (2007).
30. Dutta, O., Gajda, M., Hauke, P., *et al.* Non-standard Hubbard models in optical lattices: a review. *Reports on Progress in Physics* **78** (2015).
31. Moore, G. E. Cramming more components onto integrated circuits. *Electronics* **38**, 114–117 (1998).
32. Steane, A. M. Efficient fault-tolerant quantum computing. *Nature* **399** (1999).
33. Tompkins, C. B. & Hohn, F. E. Applied Boolean Algebra, An Elementary Introduction. *Mathematics of Computation* **15** (1961).
34. Williams, C. P. in (2011).
35. DiVincenzo, D. P. Two-bit gates are universal for quantum computation. *Physical Review A* **51** (1995).
36. Preskill, J. Quantum Information and Computation. *Lecture Notes for Physics* **229** (1998).
37. Deutsch, D. & Jozsa, R. Rapid solution of problems by quantum computation. *Proceedings of the Royal Society of London. Series A: Mathematical and Physical Sciences* **439** (1992).
38. Brown, K. R., Chiaverini, J., Sage, J. M., *et al.* *Materials challenges for trapped-ion quantum computers* 2021.
39. Wootters, W. K. & Zurek, W. H. A single quantum cannot be cloned. *Nature* **299** (1982).
40. Hamming, R. W. Error Detecting and Error Correcting Codes. *Bell System Technical Journal* **29** (1950).
41. Mielke, N., Marquart, T., Wu, N., *et al.* Bit error rate in NAND flash memories in *IEEE International Reliability Physics Symposium Proceedings* (2008).
42. Shor, P. W. Scheme for reducing decoherence in quantum computer memory. *Physical Review A* **52** (1995).
43. Peres, A. Reversible logic and quantum computers. *Physical Review A* **32** (1985).

Bibliography

44. Shor, P. W. *Fault-tolerant quantum computation* in *Annual Symposium on Foundations of Computer Science - Proceedings* (1996).
45. Rains, E. M. Nonbinary quantum codes. *IEEE Transactions on Information Theory* **45** (1999).
46. Kitaev, A. Y. in *Quantum Communication, Computing, and Measurement* (1997).
47. Kitaev, A. Y. Fault-tolerant quantum computation by anyons. *Annals of Physics* **303** (2003).
48. Calderbank, A. R., Rains, E. M., Shor, P. W., *et al.* Quantum error correction and orthogonal geometry. *Physical Review Letters* **78** (1997).
49. Gottesman, D. Class of quantum error-correcting codes saturating the quantum Hamming bound. *Physical Review A - Atomic, Molecular, and Optical Physics* **54** (1996).
50. Djordjevic, I. *Quantum Information Processing and Quantum Error Correction* (2012).
51. Steane, A. Multiple-particle interference and quantum error correction. *Proceedings of the Royal Society A: Mathematical, Physical and Engineering Sciences* **452** (1996).
52. Onsager, L. Crystal statistics. I. A two-dimensional model with an order-disorder transition. *Physical Review* **65**, 117–149 (1944).
53. Honecker, A., Picco, M. & Pujol, P. Universality class of the nishimori point in the 2D $+J$ random-bond ising model. *Physical Review Letters* **87** (2001).
54. Nishimori, H. No Title. *Progress of Theoretical Physics* **66** (1981).
55. Gruzberg, I. A., Read, N. & Ludwig, A. W. Random-bond Ising model in two dimensions: The Nishimori line and supersymmetry. *Physical Review B - Condensed Matter and Materials Physics* **63** (2001).
56. Shankar, R. Exact critical behavior of a random bond two-dimensional Ising model. *Physical Review Letters* **58** (1987).
57. Harris, A. B. Effect of random defects on the critical behaviour of ising models. *Journal of Physics C: Solid State Physics* **7** (1974).
58. Morgenstern, I. & Binder, K. Evidence against spin-glass order in the two-dimensional random-bond ising model. *Physical Review Letters* **43** (1979).

59. Aharonov, D. & Ben-Or, M. Fault-tolerant quantum computation with constant error rate. *SIAM Journal on Computing* **38** (2008).
60. Andrist, R. S., Katzgraber, H. G., Bombin, H., *et al.* Tricolored lattice gauge theory with randomness: Fault tolerance in topological color codes. *New Journal of Physics* **13** (2011).
61. Bombin, H., Andrist, R. S., Ohzeki, M., *et al.* Strong resilience of topological codes to depolarization. *Physical Review X* **2** (2012).
62. Ohno, T., Arakawa, G., Ichinose, I., *et al.* Phase structure of the random-plaquette Z_2 gauge model: Accuracy threshold for a toric quantum memory. *Nuclear Physics B* **697** (2004).
63. Bombin, H. & Martin-Delgado, M. A. Exact topological quantum order in $D=3$ and beyond: Branyons and brane-net condensates. *Physical Review B - Condensed Matter and Materials Physics* **75** (2007).
64. Katzgraber, H. G., Bombin, H. & Martin-Delgado, M. A. Error threshold for color codes and random three-body Ising models. *Physical Review Letters* **103**, 1–4. arXiv: 0902.4845 (2009).
65. Vijay, S., Haah, J. & Fu, L. Fracton topological order, generalized lattice gauge theory, and duality. *Physical Review B* **94** (2016).
66. Song, H., Prem, A., Huang, S. J., *et al.* Twisted fracton models in three dimensions. *Physical Review B* **99** (2019).
67. Koutsoumbas, G., Savvidy, G. K. & Savvidy, K. G. Phase structure of four-dimensional gonihedric spin system. *Physics Letters, Section B: Nuclear, Elementary Particle and High-Energy Physics* **410** (1997).
68. Ashkin, J. & Teller, E. Statistics of two-dimensional lattices with four components. *Physical Review* **64** (1943).
69. Johnston, D. A. & Ranasinghe, R. P. The dual gonihedric 3D Ising model. *Journal of Physics A: Mathematical and Theoretical* **44** (2011).
70. Mueller, M., Janke, W. & Johnston, D. A. Nonstandard finite-size scaling at first-order phase transitions. *Physical Review Letters* **112** (2014).
71. Mueller, M., Johnston, D. A. & Janke, W. Multicanonical analysis of the plaquette-only gonihedric Ising model and its dual. *Nuclear Physics B* **888** (2014).

Bibliography

72. Johnston, D. A., Mueller, M. & Janke, W. Macroscopic degeneracy and order in the 3D plaquette Ising model. *Modern Physics Letters B* **29** (2015).
73. Johnston, D. A., Mueller, M. & Janke, W. *Plaquette Ising models, degeneracy and scaling* 2017.
74. Metropolis, N. & Ulam, S. The Monte Carlo Method. *Journal of the American Statistical Association* **44**, 335–341 (1949).
75. Fehske, H., Schneider, R. & Weiße, A. *Computational Many-Particle Physics* (Springer, 2008).
76. Liu, A. J. & Fisher, M. E. The three-dimensional Ising model revisited numerically. *Physica A: Statistical Mechanics and its Applications* **156** (1989).
77. Talapov, A. L. & Blöte, H. W. The magnetization of the 3D Ising model. *Journal of Physics A: Mathematical and General* **29** (1996).
78. Lavis, D. & Bell, G. M. *Statistical Mechanics of Lattice Systems: Volume 1: Closed-Form and Exact Solutions* (Springer Science & Business Media, 2013).
79. Papon, P., Leblond, J. & Meijer, P. H. *The physics of phase transitions: Concepts and applications* (2006).
80. Lee, J. & Kosterlitz, J. M. Finite-size scaling and Monte Carlo simulations of first-order phase transitions. *Physical Review B* **43** (1991).
81. Ehrenfest, P. Phasenumwandlungen im ueblichen und erweiterten Sinn, classifiziert nach den entsprechenden Singularitaeten des thermo-dynamischen Potentials. *Proceedings Koninklijke Akademie van Wetenschappen* **36** (1933).
82. Landau, L. D. On the theory of phase transitions. *Phys. Z. Sowjet.* **11** (1937).
83. Liu, J. S. *Monte Carlo Strategies in Scientific Computing* (2004).
84. BILLINGSLEY, P. *Probability and Measure* (JOHN WILEY & SONS, 1995).
85. Metropolis, N., Rosenbluth, A. W., Rosenbluth, M. N., *et al.* Equation of state calculations by fast computing machines. *The Journal of Chemical Physics* **21** (1953).
86. Swendsen, R. H. & Wang, J. S. Nonuniversal critical dynamics in Monte Carlo simulations. *Physical Review Letters* **58** (1987).
87. Wolff, U. Collective Monte Carlo Updating for Spin Systems. *Physical Review Letters* **62** (1989).

88. Hastings, W. K. Monte carlo sampling methods using Markov chains and their applications. *Biometrika* **57** (1970).
89. Berg, B. A. in (2005).
90. Katzgraber, H. G., Trebst, S., Huse, D. A., *et al.* Feedback-optimized parallel tempering Monte Carlo. *Journal of Statistical Mechanics: Theory and Experiment* (2006).
91. Challa, M. S., Landau, D. P. & Binder, K. Finite-size effects at temperature-driven first-order transitions. *Physical Review B* **34** (1986).
92. Mueller, M., Janke, W. & Johnston, D. A. Planar ordering in the plaquette-only gonihedric Ising model. *Nuclear Physics B* **894**, 1–14 (2015).
93. Lee, J. & Kosterlitz, J. M. New numerical method to study phase transitions. *Physical Review Letters* **65** (1990).
94. Ferrenberg, A. M. & Swendsen, R. H. New Monte Carlo technique for studying phase transitions. *Physical Review Letters* **61** (1988).
95. Wu, F. Y. & Wang, Y. K. Duality transformation in a many-component spin model. *Journal of Mathematical Physics* **17** (1975).
96. Aizenman, M. & Wehr, J. Rounding of first-order phase transitions in systems with quenched disorder. *Physical Review Letters* **62** (1989).
97. Jin, S., Sen, A. & Sandvik, A. W. Ashkin-teller criticality and pseudo-first-order behavior in a frustrated Ising model on the square lattice. *Physical Review Letters* **108** (2012).
98. Baxter, R. J. *Potts model at the critical temperature* 1973.
99. Katzgraber, H. G., Körner, M. & Young, A. P. Universality in three-dimensional Ising spin glasses: A Monte Carlo study. *Physical Review B - Condensed Matter and Materials Physics* **73** (2006).
100. Gilbert, E. N. A Comparison of Signalling Alphabets. *Bell System Technical Journal* **31** (1952).
101. Varshamov, R. R. Estimate of the number of signals in error correcting codes. *Dokl. Akad. Nauk SSSR Soviet Math. - Doklady* **117** (1957).
102. Calderbank, A. R. & Shor, P. W. Good quantum error-correcting codes exist. *Physical Review A - Atomic, Molecular, and Optical Physics* **54** (1996).
103. Jaksch, D., Bruder, C., Cirac, J. I., *et al.* Cold bosonic atoms in optical lattices. *Physical Review Letters* **81** (1998).

Bibliography

104. Van Oosten, D., van der Straten, P. & Stoof, H. T. Quantum phases in an optical lattice. *Physical Review A. Atomic, Molecular, and Optical Physics* **63** (2001).
105. Greiner, M., Mandel, O., Esslinger, T., *et al.* Quantum phase transition from a superfluid to a mott insulator in a gas of ultracold atoms. *Nature* **415** (2002).
106. Günter, K., Stöferle, T., Moritz, H., *et al.* Bose-Fermi mixtures in a three-dimensional optical lattice. *Physical Review Letters* **96** (2006).
107. Ferrier-Barbut, I., Delehaye, M., Laurent, S., *et al.* A mixture of Bose and Fermi superfluids. *Science* **345** (2014).
108. Gadway, B., Pertot, D., Reimann, R., *et al.* Superfluidity of interacting bosonic mixtures in optical lattices. *Physical Review Letters* **105** (2010).
109. Jürgensen, O., Sengstock, K. & Lühmann, D. S. Density-induced processes in quantum gas mixtures in optical lattices. *Physical Review A - Atomic, Molecular, and Optical Physics* **86** (2012).
110. Delehaye, M., Laurent, S., Ferrier-Barbut, I., *et al.* Critical Velocity and Dissipation of an Ultracold Bose-Fermi Counterflow. *Physical Review Letters* **115** (2015).
111. Albus, A., Illuminati, F. & Eisert, J. Mixtures of bosonic and fermionic atoms in optical lattices. *Physical Review A - Atomic, Molecular, and Optical Physics* **68** (2003).
112. Mathey, L., Wang, D. W., Hofstetter, W., *et al.* Luttinger liquid of polarons in one-dimensional boson-fermion mixtures. *Physical Review Letters* **93** (2004).
113. Suzuki, K., Miyakawa, T. & Suzuki, T. P -wave superfluid and phase separation in atomic Bose-Fermi mixtures. *Physical Review A - Atomic, Molecular, and Optical Physics* **77** (2008).
114. Mering, A. & Fleischhauer, M. One-dimensional Bose-Fermi-Hubbard model in the heavy-fermion limit. *Physical Review A - Atomic, Molecular, and Optical Physics* **77** (2008).
115. Fetter, A. L., Walecka, J. D. & Kadanoff, L. P. Quantum Theory of Many Particle Systems. *Physics Today* **25** (1972).
116. Stoof, H. T., Gubbels, K. B. & Dickerscheid, D. B. Ultracold Quantum Fields (Springer, Dordrecht, 2009).

117. Krutitsky, K. V. *Ultracold bosons with short-range interaction in regular optical lattices* 2016.
118. Batrouni, G. G., Rousseau, V., Scalettar, R. T., *et al.* Mott Domains of Bosons Confined on Optical Lattices. *Physical Review Letters* **89** (2002).
119. Pollet, L., Rombouts, S., Heyde, K., *et al.* Bosons confined in optical lattices: The numerical renormalization group revisited. *Physical Review A - Atomic, Molecular, and Optical Physics* **69** (2004).
120. Fölling, S., Widera, A., Müller, T., *et al.* Formation of spatial shell structure in the superfluid to mott insulator transition. *Physical Review Letters* **97** (2006).
121. Bogoliubov, N. On the theory of superfluidity. *J. Phys* (1947).
122. Kühner, T. D., White, S. R. & Monien, H. One-dimensional Bose-Hubbard model with nearest-neighbor interaction. *Physical Review B - Condensed Matter and Materials Physics* **61** (2000).
123. Elstner, N. & Monien, H. Dynamics and thermodynamics of the bose-hubbard model. *Physical Review B - Condensed Matter and Materials Physics* **59** (1999).
124. Batrouni, G. G. & Scalettar, R. T. World-line quantum Monte Carlo algorithm for a one-dimensional Bose model. *Physical Review B* **46** (1992).
125. Kashurnikov, V. A., Krasavin, A. V. & Svistunov, B. V. Mott-insulator-superfluid-liquid transition in a one-dimensional bosonic Hubbard model: Quantum Monte Carlo method. *JETP Letters* **64** (1996).
126. Kühner, T. & Monien, H. Phases of the one-dimensional Bose-Hubbard model. *Physical Review B - Condensed Matter and Materials Physics* **58** (1998).
127. Ibarra-García-Padilla, E., Mukherjee, R., Hulet, R. G., *et al.* Thermodynamics and magnetism in the two-dimensional to three-dimensional crossover of the Hubbard model. *Physical Review A* **102** (2020).
128. Giamarchi, T. *Quantum Physics in One Dimension* (2007).
129. Cazalilla, M. A., Ho, A. F. & Giamarchi, T. Interacting Bose gases in quasi-one-dimensional optical lattices. *New Journal of Physics* **8** (2006).
130. Van Otterlo, A., Wagenblast, K. H., Baltin, R., *et al.* Quantum phase transitions of interacting bosons and the supersolid phase. *Physical Review B* **52** (1995).

Bibliography

131. Ejima, S. & Fehske, H. Entanglement properties of the nontrivial Haldane insulator in the 1D extended Bose-Hubbard model. *J. Phys.: Conf. Ser.* **592** (2015).
132. Mermin, N. D. & Wagner, H. Absence of ferromagnetism or antiferromagnetism in one- or two-dimensional isotropic Heisenberg models. *Physical Review Letters* **17** (1966).
133. Batrouni, G. G., Rousseau, V. G., Scalettar, R. T., *et al.* Competing phases, phase separation, and coexistence in the extended one-dimensional bosonic Hubbard model. *Physical Review B - Condensed Matter and Materials Physics* **90** (2014).
134. Sicks, J. & Rieger, H. Haldane insulator in the 1D nearest-neighbor extended Bose-Hubbard model with cavity-mediated long-range interactions. *European Physical Journal B* **93** (2020).
135. Batrouni, G. G., Hébert, F. & Scalettar, R. T. Supersolid phases in the one-dimensional extended soft-core bosonic hubbard model. *Physical Review Letters* **97** (2006).
136. Rossini, D. & Fazio, R. Phase diagram of the extended Bose-Hubbard model. *New Journal of Physics* **14** (2012).
137. Mandel, O., Greiner, M., Widera, A., *et al.* Controlled collisions for multi-particle entanglement of optically trapped atoms. *Nature* **425** (2003).
138. Dogra, N., Brennecke, F., Huber, S. D., *et al.* Phase transitions in a Bose-Hubbard model with cavity-mediated global-range interactions. *Physical Review A* **94** (2016).
139. Hubbard, J. Electron correlations in narrow energy bands. *Proceedings of the Royal Society of London. Series A. Mathematical and Physical Sciences* **276** (1963).
140. Giorgini, S., Pitaevskii, L. P. & Stringari, S. Theory of ultracold atomic Fermi gases. *Reviews of Modern Physics* **80** (2008).
141. Köhl, M., Moritz, H., Stöferle, T., *et al.* Fermionic atoms in a three dimensional optical lattice: Observing Fermi surfaces, dynamics, and interactions. *Physical Review Letters* **94** (2005).
142. Hofstetter, W., Cirac, J. I., Zoller, P., *et al.* High-Temperature Superfluidity of Fermionic Atoms in Optical Lattices. *Physical Review Letters* **89** (2002).

143. Lieb, E. H. & Wu, F. Y. Absence of mott transition in an exact solution of the short-range, one-band model in one dimension. *Physical Review Letters* **20** (1968).
144. Essler, F. H. L., Frahm, H., Göhmann, F., *et al.* The One-Dimensional Hubbard Model (Cambridge University Press, 2005).
145. White, S. R., Scalapino, D. J., Sugar, R. L., *et al.* Numerical study of the two-dimensional Hubbard model. *Physical Review B* **40** (1989).
146. Staudt, R., Dzierzawa, M. & Muramatsu, A. Phase diagram of the three-dimensional Hubbard model at half filling. *European Physical Journal B* **17** (2000).
147. Troyer, M. & Wiese, U. J. Computational complexity and fundamental limitations to fermionic quantum Monte Carlo simulations. *Physical Review Letters* **94** (2005).
148. Corboz, P., Evenbly, G., Verstraete, F., *et al.* Simulation of interacting fermions with entanglement renormalization. *Physical Review A - Atomic, Molecular, and Optical Physics* **81** (2010).
149. Iemini, F., Maciel, T. O. & Vianna, R. O. Entanglement of indistinguishable particles as a probe for quantum phase transitions in the extended Hubbard model. *Physical Review B - Condensed Matter and Materials Physics* **92** (2015).
150. Hirsch, J. E. Charge-density-wave to spin-density-wave transition in the extended Hubbard model. *Physical Review Letters* **53** (1984).
151. Nakamura, M. Mechanism of CDW-SDW Transition in One Dimension. *Journal of the Physical Society of Japan* **68** (1999).
152. Nakamura, M. Tricritical behavior in the extended Hubbard chains. *Physical Review B - Condensed Matter and Materials Physics* **61** (2000).
153. Sengupta, P., Sandvik, A. W. & Campbell, D. K. Bond-order-wave phase and quantum phase transitions in the one-dimensional extended hubbard model. *Physical Review B - Condensed Matter and Materials Physics* **65** (2002).
154. Jeckelmann, E. Ground-State Phase Diagram of a Half-Filled One-Dimensional Extended Hubbard Model. *Physical Review Letters* **89** (2002).

Bibliography

155. Sandvik, A. W., Balents, L. & Campbell, D. K. Ground state phases of the half-filled one-dimensional extended Hubbard model. *Physical Review Letters* **92** (2004).
156. Tsuchiizu, M. & Furusaki, A. Ground-state phase diagram of the one-dimensional half-filled extended Hubbard model. *Physical Review B - Condensed Matter and Materials Physics* **69** (2004).
157. Glocke, S., Klümper, A. & Sirker, J. Half-filled one-dimensional extended Hubbard model: Phase diagram and thermodynamics. *Physical Review B - Condensed Matter and Materials Physics* **76** (2007).
158. Pollet, L., Troyer, M., Van Houcke, K., *et al.* Phase diagram of bose-fermi mixtures in one-dimensional optical lattices. *Physical Review Letters* **96** (2006).
159. Lewenstein, M., Santos, L., Baranov, M. A., *et al.* Atomic Bose-Fermi Mixtures in an Optical Lattice. *Physical Review Letters* **92** (2004).
160. Titvinidze, I., Snoek, M. & Hofstetter, W. Supersolid Bose-Fermi mixtures in optical lattices. *Physical Review Letters* **100** (2008).
161. Büchler, H. P. & Blatter, G. Supersolid versus phase separation in atomic bose-fermi mixtures. *Physical Review Letters* **91** (2003).
162. Polak, T. P. & Kopeć, T. K. Zero-temperature phase diagram of Bose-Fermi gaseous mixtures in optical lattices. *Physical Review A - Atomic, Molecular, and Optical Physics* **81** (2010).
163. Hatsuda, R. & Arahata, E. Ground-state and Excitation Spectra of Bose-Fermi Mixtures in a Three-Dimensional Optical Lattice. *Journal of the Physical Society of Japan* **89** (2020).
164. Cazalilla, M. A., Ho, A. F. & Giamarchi, T. Two-component fermi gas on internal-state-dependent optical lattices. *Physical Review Letters* **95** (2005).
165. Ospelkaus, S., Ospelkaus, C., Wille, O., *et al.* Localization of bosonic atoms by fermionic impurities in a three-dimensional optical lattice. *Physical Review Letters* **96** (2006).
166. Pollet, L., Kollath, C., Schollwöck, U., *et al.* Mixture of bosonic and spin-polarized fermionic atoms in an optical lattice. *Physical Review A - Atomic, Molecular, and Optical Physics* **77** (2008).

167. Mathey, L. & Wang, D. W. Phase diagrams of one-dimensional Bose-Fermi mixtures of ultracold atoms. *Physical Review A - Atomic, Molecular, and Optical Physics* **75** (2007).
168. Bukov, M. & Pollet, L. Mean-field phase diagram of the Bose-Fermi Hubbard model. *Physical Review B - Condensed Matter and Materials Physics* **89** (2014).
169. Anders, P., Werner, P., Troyer, M., *et al.* From the cooper problem to canted supersolids in bose-fermi mixtures. *Physical Review Letters* **109** (2012).
170. Avella, R., Mendoza-Arenas, J. J., Franco, R., *et al.* Insulator phases of a mixture of spinor fermions and hard-core bosons. *Physical Review A* **100** (2019).
171. Pollet, L., Houcke, K. V. & Rombouts, S. M. Engineering local optimality in quantum Monte Carlo algorithms. *Journal of Computational Physics* **225** (2007).
172. Hanke-Bourgeois, M. Grundlagen der Numerischen Mathematik und des Wissenschaftlichen Rechnens (2006).
173. Komzsik, L. The Lanczos Method: Evolution and Application. *Scientific Programming* **12** (2004).
174. Schönmeier-Kromer, J. *Quantum Monte Carlo Simulation of the Spiny Bose-Fermi-Hubbard Model in One Dimension* Masterthesis (Ludwig-Maximilians-Universität, 2015).
175. Lehoucq, R. B., Sorensen, D. C. & Yang, C. ARPACK Users' Guide (1998).
176. Virtanen, P., Gommers, R., Oliphant, T. E., *et al.* SciPy 1.0: fundamental algorithms for scientific computing in Python. *Nature Methods* **17** (2020).
177. Prokof'ev, N. V., Svistunov, B. V. & Tupitsyn, I. S. "WORM" ALGORITHM IN QUANTUM MONTE CARLO SIMULATIONS. *Physics Letters, Section A: General, Atomic and Solid State Physics* **238** (1998).
178. Büchler, H. P. & Blatter, G. Phase separation of atomic Bose-Fermi mixtures in an optical lattice. *Physical Review A - Atomic, Molecular, and Optical Physics* **69** (2004).
179. Viverit, L., Pethick, C. J. & Smith, H. Zero-temperature phase diagram of binary boson-fermion mixtures. *Physical Review A - Atomic, Molecular, and Optical Physics* **61** (2000).

Bibliography

180. Ejima, S., Fehske, H., Gebhard, F., *et al.* Characterization of Mott-insulating and superfluid phases in the one-dimensional Bose-Hubbard model. *Physical Review A - Atomic, Molecular, and Optical Physics* **85** (2012).
181. Bogoljubov, N. N., Tolmachov, V. V. & Širkov, D. V. A New Method in the Theory of Superconductivity. *Fortschritte der Physik* **6** (1958).
182. Bilitewski, T. & Pollet, L. Exotic superconductivity through bosons in a dynamical cluster approximation. *Physical Review B - Condensed Matter and Materials Physics* **92** (2015).
183. Mathey, L., Tsai, S. W. & Neto, A. H. Competing types of order in two-dimensional bose-fermi mixtures. *Physical Review Letters* **97** (2006).
184. Krinner, S., Lacroix, N., Remm, A., *et al.* Realizing Repeated Quantum Error Correction in a Distance-Three Surface Code. arXiv: 2112.03708 (2021).
185. Avella, R., Mendoza-Arenas, J. J., Franco, R., *et al.* Mixture of scalar bosons and two-color fermions in one dimension: Superfluid-insulator transitions. *Physical Review A* **102** (2020).
186. Guerrero-Suarez, R., Mendoza-Arenas, J. J., Franco, R., *et al.* Spin-selective insulators in Bose-Fermi mixtures. *Physical Review A* **103** (2021).
187. Efron, B. & Tibshirani, R. J. An Introduction to the Bootstrap (1993).
188. Johnson, R. W. An Introduction to the Bootstrap. *Teaching Statistics* **23** (2001).
189. Gaenko, A., Antipov, A. E., Carcassi, G., *et al.* Updated core libraries of the ALPS project. *Computer Physics Communications* **213** (2017).
190. Nishimori, H. *Duality in finite-dimensional spin glasses* in *Journal of Statistical Physics* **126** (2007).
191. Kubica, A., Beverland, M. E., Brandão, F., *et al.* Three-Dimensional Color Code Thresholds via Statistical-Mechanical Mapping. *Physical Review Letters* **120** (2018).

List of Publications

- P1. Song, H., Schönmeier-Kromer, J., Liu, K., Viyuela, O., Pollet, L. & Martin-Delgado, M. A. Optimal Thresholds for Fracton Codes and Random Spin Models With Subsystem Symmetry. *Preprint submitted to Physical Review Letters*. arXiv: 2112.05122 (2021).
- P2. Schönmeier-Kromer, J. & Pollet, L. Ground-state phase diagram of the two-dimensional Bose-Hubbard model with anisotropic hopping. *Physical Review A - Atomic, Molecular, and Optical Physics* **89**. arXiv: 1308.2229 (2014).

List of Abbreviations

1D	one dimension
2D	two dimensions
3D	three dimensions
ATM	Ashkin-Teller model
BFHM	Bose-Fermi-Hubbard model
BHM	Bose-Hubbard model
BOW	bond order wave
CDW	charge density wave
CSS	Calderbank-Shor-Steane
DMFT	dynamical mean-field theory
DMRG	density matrix renormalization group
eBHM	extended Bose-Hubbard model
ED	exact diagonalization
eFHM	extended Fermi-Hubbard model
FHM	Fermi-Hubbard model
HI	Haldane insulator
IM	Ising model
KT	Kosterlitz-Thouless
LL	Luttinger liquid
MC	Monte Carlo
MI	Mott insulator
NISQ	Noisy Intermediate-Scale Quantum
PIM	Plaquette Ising model
PS	phase separation
PT	phase transition
QMC	quantum Monte Carlo
RACAT	random anisotropically coupled Ashkin-Teller

List of Abbreviations

RPI	random plaquette Ising
sBFHM	spinful Bose-Fermi-Hubbard model
SDW	spin density wave
SF	superfluid
SS	supersolid

Acknowledgments

Finally, I would like to thank everyone who supported and accompanied me during my doctorate.

First and foremost, I would like to thank Professor Dr. Lode Pollet, who gave me the opportunity to pursue the research projects, which led to this thesis, in his group. Thank you, that your door was always open and that you always took time for emerging questions, discussions and problems.

I am much obliged to all members of the joint fracton project. In this regard, I would like to mention Dr. Ke Liu in particular. He offered invaluable guidance throughout the project and his help in proofreading the draft of this thesis was highly appreciated.

Special thanks are also due to Professor Dr. Miguel Martin-Delgado, who declared his willingness to act as a second examiner next to Professor Dr. Lode Pollet, as well as to the entire examination board, namely Professor Dr. Monika Aidelsburger, Professor Dr. Jan Lipfert, Professor Dr. Gerhard Buchalla and Professor Dr. Thomas Birner for taking the time to be part of my PhD commission.

I would like to thank all those involved in the Chair of Professor Dr. Schollwöck, especially Cordula Weber, who was always available with a helping hand and an open ear in all administrative matters.

Last but not least, I am thankful to my family and friends, who always supported me.